Oxide Thermoelectrics: The Role of Crystal Structure on Thermopower in Strongly Correlated Spinels

Professor:
David R. Clarke

Author:
Taylor Sparks

Oxide Thermoelectrics: The Role of Crystal Structure on Thermopower in Strongly Correlated Spinels

Abstract

This dissertation reports on the synthesis, structural and thermal characterization and electrical and thermal transport properties of a variety of strongly correlated spinels. General structure property relationships for electrical and thermal transport are discussed. However, the relationship between thermopower and features of the crystal structure such as spin, crystal field, anti-site disorder, and structural distortions are explored in depth. The experimental findings are reported in the context of improving existing oxide thermoelectric materials, screening for new materials or using thermopower as a unique characterization tool to determine the cation distribution in spinels.

The need for improved n-type oxide thermoelectric materials has led researchers to consider mixed valence (+3/+4) manganese oxides. Contrary to previous findings we report herein that the $LiMn_2O_4$ compound reaches the relatively large n-type thermopower of -73 μV/K which is three times larger than the value observed in other

manganese oxides, -25 μV/K. The cause of this increase in thermopower is shown to be the absence of a Jahn-Teller distortion on the Mn^{3+} ions in $LiMn_2O_4$. By avoiding this structural distortion the orbital degeneracy is doubled and the Koshibae et al.'s modified Heikes formula predicts a thermopower of -79 μV/K in good agreement with the experiment. Altering the $Mn^{3+/4+}$ ratio via aliovalent doping did not affect the thermopower and is a second evidence of universal charge transport first reported by Kobayashi et al. The role of anti-site disorder was further examined in $Fe_xMn_{1-x}NiCrO_4$ x=0, ½, ¾, 1 spinels but the effect on thermopower was inconclusive due to the presence of impurity phases.

Next, the thermopower as a function of temperature in Co_3O_4 was investigated as a means whereby the Wu and Mason's 30 year old model for using thermopower to calculate cation distribution in spinels could be revisited. We report evidence that Wu and Mason's original model using the standard Heikes formula and considering octahedral sites alone leads to a stoichiometrically inconsistent result at high temperatures. Alternate models are evaluated considering Koshibae et al.'s modified Heikes formula and accounting for tetrahedral site contributions. Furthermore, the effect of a possible spin state transition is considered.

Table of Contents

List of Figures

Acknowledgements

I feel so incredibly grateful to the many people and institutions who made this PhD possible. It’s cliché, but I truly couldn’t have done this alone. To start, I owe my wife, Jodi, an enormous debt of gratitude. When I told her I had a dream to do a PhD and that meant moving out of state she supported me completely and without complaint. Jodi earned this every bit as much as I did. She went to bed alone while I worked on homework, did the lion's share of the work around the house, lived in Shanghai for a summer (!), cared for our son, Atticus, and even moved clear across the country. In doing so she sacrificed her own education goals and aspirations to make mine a reality, and I’ll always be in her debt for that.

I’m indebted to my parents for raising me with love, discipline, hard work and humor. It was the example of my dad who, though a high school dropout originally, went on to change his life, outlive a “terminal” brain tumor for 25 years and graduate college as a 40 year old in engineering that made me truly believe it when he told me I could do anything I wanted in life. It was the daily efforts of my mom who raised us in happy, though humble circumstances that taught me to work hard to accomplish goals.

Though Santa Barbara is as perfect a place as you could imagine to live and to do materials research, the reason I selected UCSB for graduate school was to work with my

fantastic advisor, David Clarke. I knew right from the beginning that he was somebody who I wanted to be like and who would help me achieve great things. I honestly didn't even know what state Harvard University was located in, but when he told me he was moving there, I knew I'd come along. I can't overstate the significance of his mentorship to me. He's invested in my future by helping me obtain unique international research experiences and perspective as well as expanding my academic network. He has put confidence in me time and again to come up with my own research ideas and carry them out. I hope he knows how grateful I am for all this and for his patience in helping me write (and rewrite) papers and for putting up with the occasional explosion in the laboratory.

Some of the most gratifying experiences of my PhD were realized while working with diverse individuals from all over the world. I express thanks to my coworkers Aleksander Gurlo, Qu Zhixue, Wan Chunlei, Jérôme Chevalier, Laurent Gremillard, Maged Bekheet and many, many others with whom I carried out experiments. The Clarke group, too, over the years has been a great source of friendship, learning and I acknowledge my good friends Bill, Xin, Sam, Andi, Yang, Jiangshui, Mor, Ashwin, Michael, Mary, Jesse, Roger, John, Jenny, Liguo, Sebastien, and Matt and I will certainly miss the Annual Clarke Group Holiday Table Tennis Invitational.

I'm indebted to a number of institutions and professors that hosted me for extended international research stays. Among these are Prof. Pan Wei at Tsinghua University, China, Prof. Gu Hui at the Shanghai Institute of Ceramics, Chinese Academy

of Science, China, Dr. Laetitia Laversenne and Dr. Aleksander Gurlo at the Institut Laue-Langevin, France and Technische Universität Darmstadt, Germany respectively. There are many things one simply can't learn but by having experienced them.

I've been privileged to receive training from world class experts. Professors like Ram Seshadri, Frans Spaepan, Shriram Ramanathan, Evelyn Hu, Nicola Spaldin, Omar Saleh and others at UCSB and Harvard provided exceptional coursework that had an actual impact on my research. I also recognize the enormous efforts of the International Centre for Diffraction Data (ICDD) as well as other beamline scientists and neutron and X-ray diffraction experts who taught me Rietveld refinement. This skill has been incredibly useful and I owe Joel Reid, Jim Kaduk, Brent Melot, Laetitia Laversenne, Emma Suarde, John Faber, Cyrus Crowder, Matt Suchomel, Scott Speakman, Eric Toberer, and Yan Gao my gratitude for all the help, facilities and free advice they offered me.

Finally, I gratefully acknowledge the funding from the National Science Foundation that made my PhD possible. In particular the World Materials Network (NSF-WMN), International Research and Education in Engineering China program (NSF-IREE) and the International Center for Materials Research (NSF-ICMR).

Glossary

Boltzmann constant	k_B
Work function	Φ_M
Electron affinity (n and p-type; subscripts n, p)	X
Band gap (n and p-type; subscripts n, p)	E_G
Built in potential (n and p-type; subscripts n, p)	V_{BI}
Built in barrier (n and p-type; subscripts n, p)	Φ_B
Fermi level of non-degenerate ionized dopants	E_F
Fermi level of intrinsic semiconductor	E_i
Carrier concentration of intrinsic semiconductor	n_i
Temperature (hot and cold; subscripts H, C)	T
Concentration of donor and acceptor ions	N_D, N_A
Fermi-Dirac distribution as a function of energy and temperature	$f(E,T)$
Chemical potential	μ
Energy (Fermi; subscript F)	E
Charge (positive or negative)	δ^+, δ^-
Current density (n and p-type; subscripts n, p)	j

Fundamental charge	q
Carrier concentration (n and p-type). In Chapter 3 n is an integer.	n, p
Carrier mobility (n and p-type; subscripts n, p)	v
Diffusion coefficients (n and p-type; subscripts n, p)	D
Distance	x
Electric potential	V
Seebeck coefficient or thermopower (n and p-type; subscripts n, p)	S
Thermopower (octahedral and tetrahedral sites; subscripts O, T)	S
Electric field	ε
Heat (in n and p-type materials; subscripts n, p)	Q
Electric current or intensity of peak (Section 3.2 only)	I
Peltier coefficient	Π
Time	t
Thermal conductivity (in n and p-type materials; subscripts n, p)	κ
Area (cross-sectional)	A
Electrical resistivity (n and p-type; subscripts n, p)	ρ
Length (diffusion length; subscript D)	L
Coefficient of performance (cooling efficiency)	φ
Power generation efficiency	η
Thermoelectric figure of merit	ZT
Lorenz constant	L_0

Transport coefficients (l=1,2; m=1,2)	L_{lm}, M_{lm}
Flux densities (electric, thermal, particle energy; subscripts e, heat, 1, 2)	j
Electrical conductivity (n and p-type; subscripts n, p)	σ
Electrical conductivity (octahedral and tetrahedral sites; subscripts O, T)	σ
Effective mass (electrons and holes; subscripts n, p)	m
Carrier collision time (electrons and holes; subscripts n, p)	τ
Concentration of carrier in Heikes formula	y
Electronic state degeneracy (sites i, j; subscripts i, j)	g
Orbital and spin degeneracy	$g_{orbital}, g_{spin}$
Number of particles	N
Entropy (subscripts cold, hot)	s
Transfer integral	$\bar{t}$
Creation and annihilation operators for electrons of spin ($\varsigma = \uparrow, \downarrow$)	$c^{*}_{I\varsigma}, c_{I\varsigma}$
Superexchange interactions	J
Volume of phase α	V_{α}
Total spin	ζ
Activation energy	E_A
Gas constant	R
Interplanar spacing (hkl plane; subscript hkl)	d
Incident angle of X-ray	θ

Wavelength	λ
Lattice parameters and unit cell angles	$a, b, c, \alpha, \beta, \gamma$
Atomic coordinates	u, v, w
Dispersion factors	f', f''
Weight fraction of phase α	W_α
Weighing factor of *i*-th component	W_i
Rietveld refinement residual (weighted profile)	R_{wp}
Density of phase α	$\rho_{D,\alpha}$
Mass absorption coefficient	μ_m^*
Rietveld scaling factor of phase α (Section 3.2 only)	S_α
Constant of reflection of *i*-th reflection in phase α (Section 3.2 only)	$C_{i\alpha}$
Number of formula units in the unit cell	Z
Molecular weight of phase α	M_α
Scaling factors (Section 3.2 only)	K, c
Planck's constant (Section 3.2.4 only)	h
Electric potential	V
Thermal diffusivity	α
Heat capacity at constant pressure	C_p
Porosity	P

Ionic radius (subscript indicates site; A, B, O. Superscripts indicate ion)	r
Tolerance factor	t^*
Reduced Planck's constant	$\hbar$
Three dimensional Fermi wave vector	k_F

Dedication

I dedicate this dissertation to my father whose hard work and eternal optimism gave me the self-confidence to reach for lofty goals; to my mother who sacrificed and worked, often thanklessly, in helping me achieve my goals; and to my family who motivate me, daily, to try and make the world a better place.

Chapter 1. Fundamentals of Thermoelectricity

Fossil fuels such as coal, petroleum and natural gas have been the principal source of energy fueling mankind's development since the Industrial Revolution. Because fossil fuels are the result of anaerobic decomposition of dead organisms accumulating over millions of years there is only a finite amount of fossil fuels available. With a finite amount of fuel the rate of discovery of new deposits decreases with time while the rate of consumption simultaneously increases due to population growth and changes in lifestyle. Because demand outpaces supply, the result is a peak in fossil fuel production, termed the "Hubbert Peak." [1] The decline in production leads inevitably to increased cost and market instability. Furthermore, fossil fuels are most commonly combusted and have the detriment of giving off pollutants such as carbon dioxide, sulfur dioxide and nitrogen oxides that can have serious environmental implications.

Due to the disadvantages of fossil fuels there is strong appeal for renewable sources of energy such as wind, solar, hydroelectric, geothermal, tidal, wave and biofuels. In 1949 roughly 1/3 of all the domestically produced electricity came from renewable sources.[2] Since that time there has been a general decrease in the US reliance on renewable sources of energy and most recently, in 2010, only 10.4% of electricity in the United States was from a renewable source.[3] The two largest contributors are hydroelectric power (6%) and wind power (2.3%).[4] Because energy demands continue to

increase it is critical to invest in developing technology for clean, sustainable and renewable sources of energy. The purpose of this chapter is to explain the role that thermoelectric devices could play in renewable energy as well as to describe their operation and efficiency fundamentals.

1.1 Converting Heat to and from Electricity

Considering the enormous effort and cost required for providing energy in the first place it is, perhaps, shocking to realize that ~58% [5] of all initial energy is given off as waste heat. For example, in automobiles less than 20% of fuel energy is used for propulsion because 30% is wasted as exhaust heat, 40% in radiator heat and 10% to friction and alternator.[6] Increasing efficiency in lighting, vehicles, industrial processes etc. is essential, but greater benefit would be attained if even a small fraction of waste heat could be recycled and converted back to useable electricity.

Thermoelectric electrical generators are devices than can harness waste heat, say, from industrial processing, vehicle exhaust/radiator systems[7] or solar concentrators,[8] converting it directly to an electrical potential. These same devices can be operated in reverse by applying an external voltage to direct a current through the material where the Peltier effect creates a temperature gradient for solid-state refrigeration with no moving parts or dangerous chemicals. These so-called thermoelectric or Peltier coolers are technologically important and widely used as heat pumps and temperature controllers for integrated circuits, laser diodes or in-seat cooling modules in vehicles.[9] In contrast, thermoelectric electrical generators are not yet as widely used but radioisotope

thermoelectric generators[10,11] have found application in deep space probes and cardiac pacemakers.

1.2 Thermoelectric Operation

Thermoelectric devices consist fundamentally of metal semiconductor junctions. The schematic of a simplified device is shown in Figure 1.1 in both power generation mode (left) and refrigeration mode (right). In both modes there is a hot (red) and cold (blue) side with a temperature gradient across the two thermoelectric elements. The two elements differ in carrier type; one relies on holes (purple, p-type) and the other, free electrons (green, n-type) for electrical conduction. A metal interconnect layer (orange) connects the two legs and makes a circuit such that the legs are connected in series electrically but in parallel with respect to the thermal current. The voltage across a single thermoelectric couple, also called a thermopile, is normally low whereas the required output voltage is large so actual devices consist of many pairs of thermoelectric couples connected in series.

1.2.1 Power Generation Mode

Thermoelectric devices operating in power generation mode take advantage of the thermal gradient that can be produced by waste heat to drive a current through the thermoelectric couple and produce a potential available to drive an external load. To best understand how this electrical current is created by a temperature gradient we can examine the device shown in Figure 1.1 and observe that there are essentially five regions.

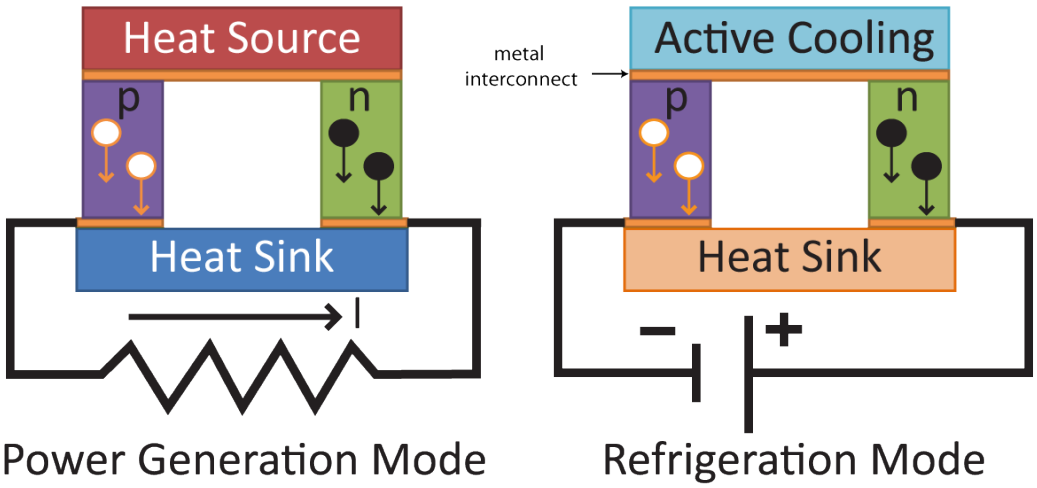

Figure 1.1. Diagrams for thermoelectric devices in power generation mode (left) and refrigeration mode (right). In both cases heat is carried from the top side to the bottom side. An electrical current is obtained automatically in power generation mode but must be powered by an external voltage in refrigeration mode.

Starting from the bottom left the electron must travel through a metal to a p-type semiconductor to a metal to an n-type semiconductor and finally back to a metal. The band diagrams, representations of electron energy as a function of spatial displacement across a device, for these five regions are shown in Figure 1.2 before (a) and after (b) the regions are placed in contact.

Let us consider first the case of thermal equilibrium throughout the device. In a metal the work function, Φ_M, is the work required to move an electron from the Fermi level to vacuum. In a semiconductor the Fermi level lies in a region of energy between the top of the valence band and the bottom of the conduction band where no electronic states exist called a band gap, E_g. For simplicity in creating figures we select p and n-type

semiconductors with equal band gap and electron affinity and metals with the same work function though this condition is not necessary in thermoelectric devices.

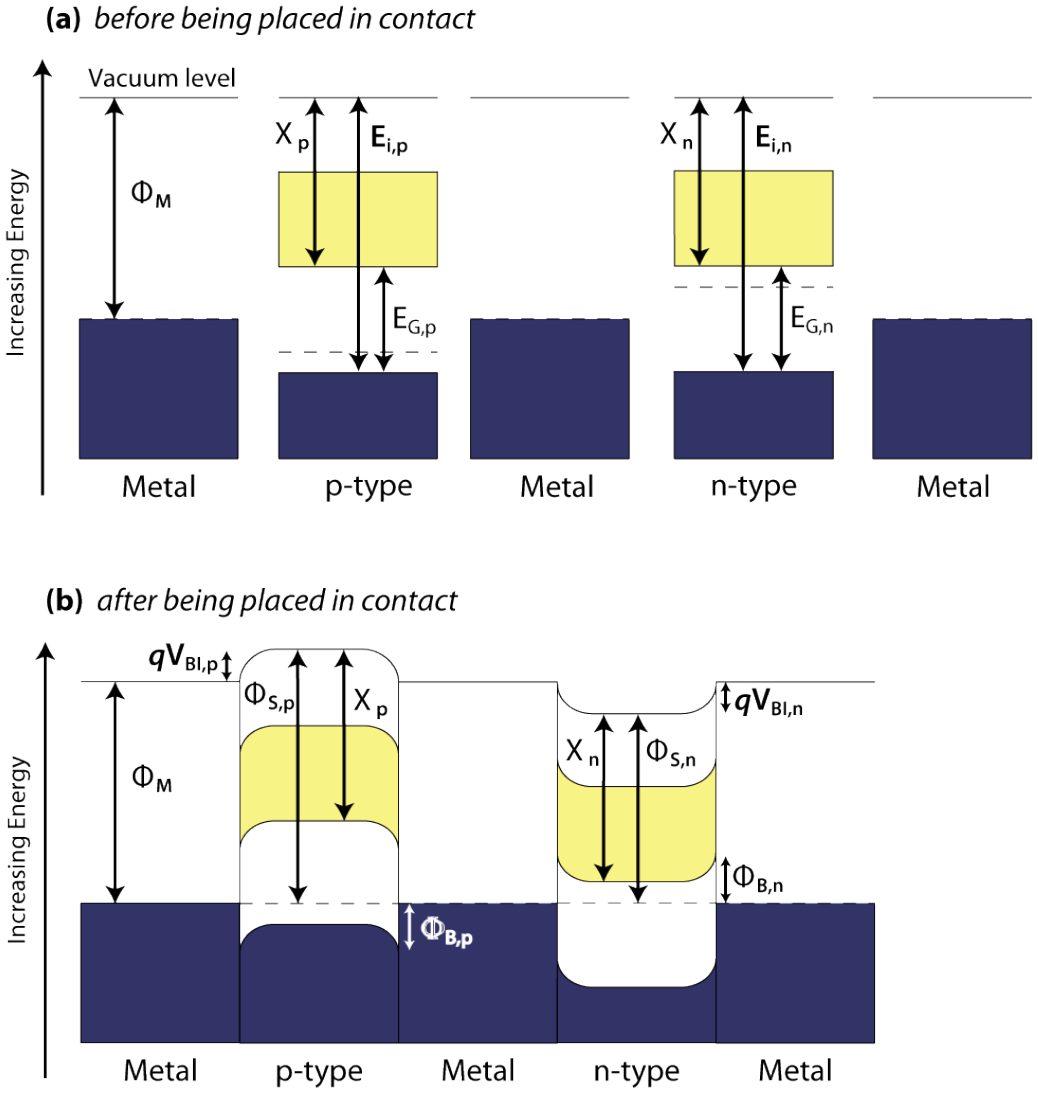

Figure 1.2. Band diagrams for a thermoelectric device before (a) and after (b) the regions are joined (no temperature gradient). The work functions, vacuum level, electron affinities, band gaps and built in (barrier) potentials are shown.

The Fermi level (shown as a dashed line in Figure 1.2) for an intrinsic or undoped semiconductor would lie in the middle of the band gap. In doped semiconductors, however, the Fermi level is closer to the valence band for p-type and closer to the conduction band for n-type semiconductors. The Fermi levels, E_F, for non-degenerate ionized dopants are given by the following set of Equations

$$E_F - E_i = k_B T \ln \frac{N_D}{n_i} \text{ where } N_D > N_A, n_i \tag{1.1}$$

$$E_i - E_F = k_B T \ln \frac{N_A}{n_i} \text{ where } N_A > N_D, n_i \tag{1.2}$$

where E_i and n_i are the Fermi level and carrier concentration of the intrinsic semiconductor, k is the Boltzmann constant, T is the absolute temperature and N_D and N_A are the concentrations of donor and acceptor dopants respectively.

When the five regions in Figure 1.2 are brought into contact and equilibrium is reached band bending at the junctions occurs such that the Fermi level is constant throughout. Before we assess the effect of a temperature gradient in this complete device it is helpful first to observe the effect of a temperature gradient in a metal as shown in Figure 1.3.

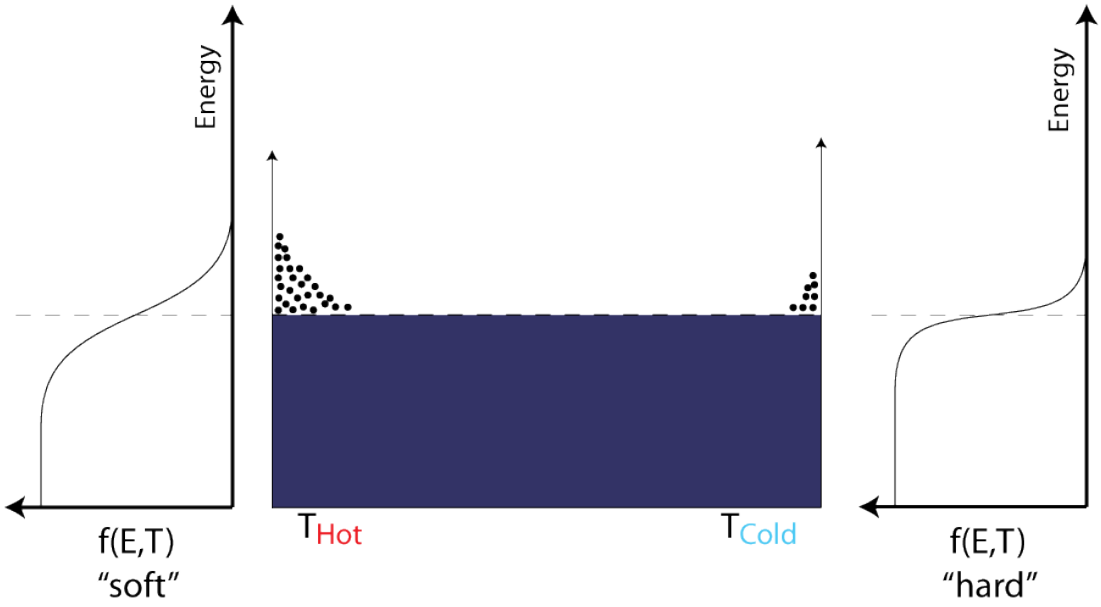

Figure 1.3. "Soft" and "hard" Fermi distributions corresponding to hot and cold sides of a metal. Figure adapted from Föll.[12]

The Fermi-Dirac distribution describes the average number of electrons at different energy levels and temperatures, $f(E,T)$, and is of the form

$$f(E,T)=\frac{1}{e^{(E-\mu)/k_BT}+1} \tag{1.3}$$

where E is the energy of the particle and μ is the chemical potential. At low temperatures a "hard" distribution is obtained whereas at high temperatures a "soft" distribution is observed. A higher temperature distribution has a higher concentration of electrons above the Fermi level. Therefore, a temperature gradient leads to a concentration gradient and diffusion of electrons from the hot side to the cold side occurs for two reasons. First, electrons move to lower energy states on the cold side and in doing so remove the

concentration gradient. Second, the electrons on the hot side have a larger momentum than those on the cold side and therefore diffuse faster towards the cold side than cold electrons diffuse away.[12]

In a thermoelectric device a temperature gradient across the semiconductor regions also results in a concentration gradient. With increasing temperature the Fermi level moves closer to the band edges (in agreement with Equations 1.1 and 1.2) because carriers are thermally activated. This results in further distortions of the bands (see Figure 1.4) and diffusion of electrons and holes across the semiconductor from the hot side to the cold side.

As higher energy electrons and holes diffuse towards the cold side they leave behind their charged donors and acceptors respectively. This displacement of charged carriers leads to the development of an electric field across the semiconductor causing backflow of current. Eventually a steady-state equilibrium is reached between backflow of current driven by the electric field and diffusion current driven by the concentration gradient. The governing equations are derived from the Drift-Diffusion model.[13] The current density for electrons and holes respectively are as follows:

$$j_n = qnv_n \frac{-dV}{dx} + qD_n \frac{dn}{dx} \tag{1.4}$$

$$j_p = qpv_p \frac{-dV}{dx} - qD_p \frac{dp}{dx} \tag{1.5}$$

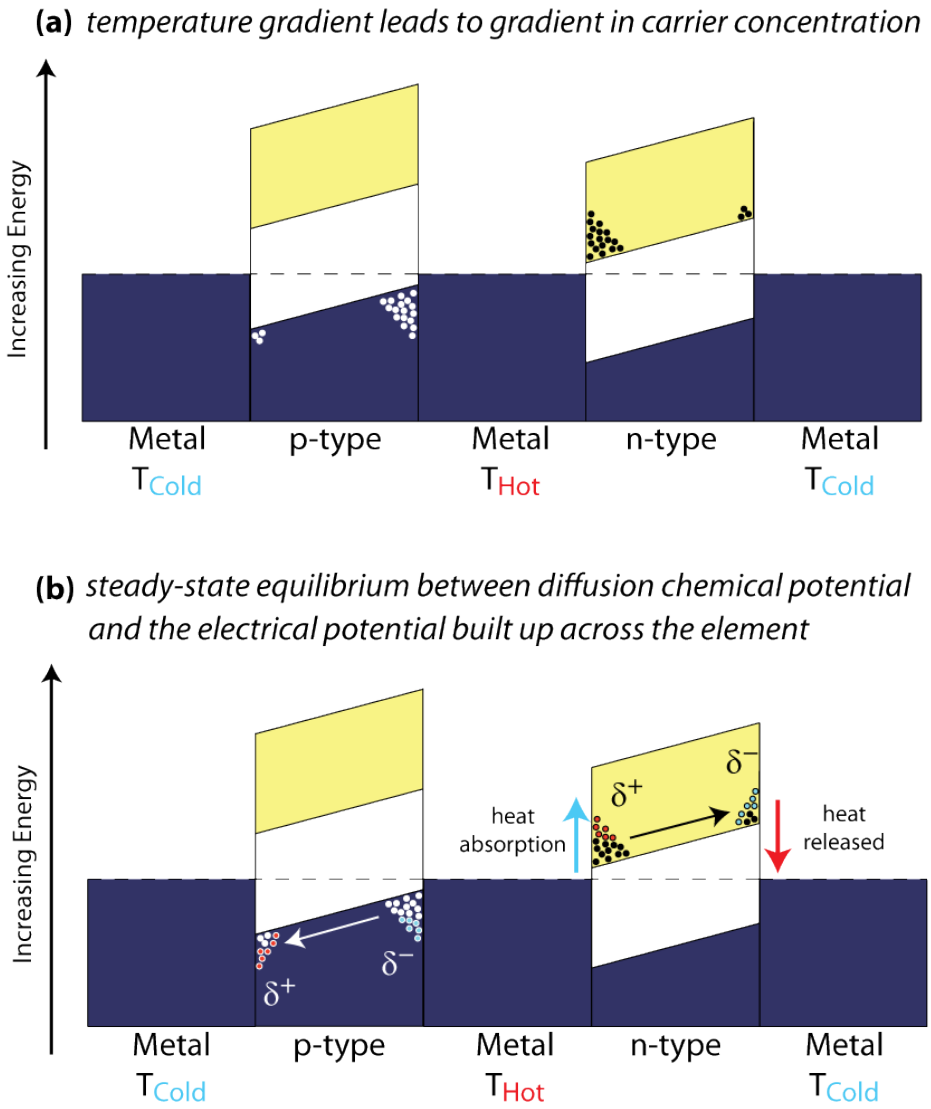

Figure 1.4. Band diagrams for a thermoelectric power generation device in a thermal gradient before (a) and after (b) steady-state equilibrium is reached. Holes and electrons in the valence and conduction bands are shown in white and black respectively. Negative charges (ionized acceptors, displaced electrons) and positive charges (ionized donors, displaced holes) are shown in blue and red respectively.

where q is the fundamental charge, n and p are the electron and hole carrier concentrations, v_n and v_p are mobilities of electrons and holes, D_n and D_p are diffusion

coefficients for electrons and holes respectively. The first term of Equations 1.4 and 1.5 represent the drift term, or how a charged particle moves due to an applied electric field, and the second term represents diffusion or how a particle moves due to a concentration gradient.

The Drift-Diffusion model assumes a constant temperature throughout the device which is obviously not the case in a thermoelectric device. However, if material properties do not change with position then we can rewrite Equations 1.4 and 1.5 using the temperature gradient instead of the concentration gradient and replacing the diffusion coefficient with the Seebeck coefficient, S, (also called thermopower)

$$j_n = qn\mu \frac{-dV}{dx} + qS_n \frac{dT}{dx} \tag{1.6}$$

$$j_p = qp\mu \frac{-dV}{dx} - qS_p \frac{dT}{dx}. \tag{1.7}$$

The Seebeck coefficient is the electric field, ε, or voltage differential across a temperature gradient

$$S = \frac{\varepsilon}{\nabla T} = \frac{\Delta V}{\Delta T}. \tag{1.8}$$

The sign of the Seebeck coefficient is defined as positive if the electric field is in the same direction as the temperature gradient such that the higher temperature end of a material would have the lower potential.

Figure 1.4 clearly shows that as an electron travels from left to right through the device heat must be absorbed from the middle metal region (hot side) and released at the outer metal regions (cold side). This is consistent with the energy band diagram. For example, an electron travels from the hot metal into the conduction band of the n-type semiconductor at a higher energy level by absorbing energy. As electrons are transported from the hot side to the cold side of the semiconductor they carry heat with them and when they leave the conduction band to re-enter the metal they go from high energy to low and must release heat to do so.

1.2.2 Refrigeration Mode

Having just explained in detail the operation of a thermoelectric device in power generation mode it is a simple thing to describe the operation of a thermoelectric device in refrigeration mode. These so called Peltier coolers rely on the Peltier effect defined as the heat loss per unit time, dQ/dt, as current, I, travels through a junction between two materials A and B, or

$$\frac{dQ}{dt} = (\Pi_A - \Pi_B)I \tag{1.9}$$

where Π_A and Π_B are the Peltier coefficients of the two materials. The Peltier coefficient itself is related to the Seebeck coefficient by the relation

$$\Pi = S\,T \,. \tag{1.10}$$

The band diagram for a thermoelectric cooler, shown in Figure 1.5, is instructive to see how the same device used for power generation can also be used for active cooling when an external potential is applied across the device. From left to right, an electron must release heat at the metal/p-type junction, absorb heat at the p-type/metal and metal/n-type junctions, and finally release heat at the n-type/metal junction. The result is that the outer metal regions act as heat sinks and active cooling is achieved in the central metal region. This heat transfer makes sense physically because the p-type material valance band is at a lower energy level than the metal and the n-type material conduction band is at a higher energy level than the metal.

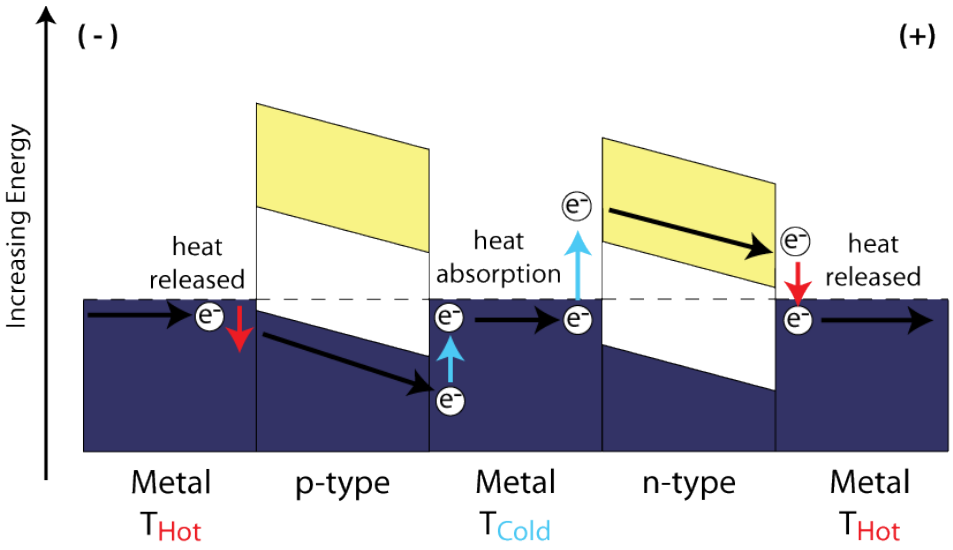

Figure 1.5. Band diagram for a thermoelectric cooler. An external potential across the device directs a current through the material where carriers absorb heat from the central metal region and release it on the outer regions to achieve active, solid-state cooling. Figure redrawn from Tamer et al.[14]

1.3 Thermal and Electrical Transport

Consider a thermoelectric couple (refrigeration mode) such as the one shown in Figure 1.1 with two thermoelectric elements (n and p-type) of length L and cross-sectional area A. Following the treatment by others, [14–17] the heat flow rate across the respective elements is

$$Q_n = -S_n IT - \kappa_n A\frac{dT}{dx} \tag{1.11}$$

$$Q_p = S_p IT - \kappa_p A\frac{dT}{dx} \tag{1.12}$$

where κ_n and κ_p are the thermal conductivities of the n and p-type materials. The first term represents the heat transported by the electrical carriers themselves and the second term represents the heat transported due to the temperature gradient. In the refrigeration mode, contrary to power generation mode, the heat flow from electrical carriers is opposite that of thermal conduction, hence the opposite sign. Additionally, due to Joule heating there is actually heat being generated within the elements themselves at a rate per unit length shown by the following

$$-\kappa_n A\frac{-d^2T}{dx^2} = \frac{I^2\rho_n}{A} \tag{1.13}$$

$$-\kappa_p A\frac{-d^2T}{dx^2}=\frac{I^2\rho_p}{A} \tag{1.14}$$

where $\rho_n$and ρ_p are the electrical resistivities of the two elements. Applying the boundary conditions that $T=T_C$ at $x=0$ and $T=T_H$ at $x=L$ for the cold and hot sides respectively, solving the differential equations and substituting back into the original heat flow rate Equations 1.11 and 1.12 we obtain the following

$$Q_n=-S_nIT_C-\frac{\kappa_nA(T_H-T_C)}{L}-\frac{I^2\rho_nL}{2A} \tag{1.15}$$

$$Q_p=S_pIT_C-\frac{\kappa_pA(T_H-T_C)}{L}-\frac{I^2\rho_pL}{2A}. \tag{1.16}$$

The total rate of heat transferred across the couple (the cooling power at the heat sink) is the combination of the heat transferred across n and p-type elements. Summing Equations 1.15 and 1.16 we obtain

$$Q=SIT_C-(T_H-T_C)\frac{(\kappa_n+\kappa_p)A}{L}-\frac{(\rho_n+\rho_p)I^2L}{2A} \tag{1.17}$$

where $S=S_p-S_n$. Recall that the legs are connected in parallel thermally but in series electrically. Therefore the thermal resistance, κ, and the electrical resistance, ρ, can be written as

$$\kappa = \frac{\kappa_n A}{L} + \frac{\kappa_p A}{L} \tag{1.18}$$

$$\rho = \frac{\rho_n L}{A} + \frac{\rho_p L}{A} . \tag{1.19}$$

Therefore, Equation 1.17 simplifies to

$$Q = SIT_C - \kappa(T_H - T_C) - \frac{\rho I^2}{2} . \tag{1.20}$$

We can derive the power, P, consumed in each leg in much the same way

$$P_n = -S_n I(T_H - T_C) - \frac{I^2 \rho_n L}{A} \tag{1.21}$$

$$P_p = S_p I(T_H - T_C) - \frac{I^2 \rho_p L}{A} \tag{1.22}$$

and the total power for the thermoelectric couple is the sum

$$P = SI(T_H - T_C) - I^2 \rho . \tag{1.23}$$

1.3.1 Efficiency and Coefficient of Performance

A crucial attribute of all thermoelectric materials is their efficiency in converting

between heat and electricity. A high cost, low efficiency thermoelectric device may not be justified especially considering alternative, competing technologies[18,19] such as the Stirling engines which tend to be more efficient though bulkier and featuring moving parts.[20] The total device efficiency for a cooler, often called the coefficient of performance, is simply the heat transported divided by the power supplied (Equations 1.20 and 1.23)

$$\varphi = \frac{Q}{P} = \frac{SIT_C - \kappa(T_H - T_C) - \frac{I^2\rho}{2}}{SI(T_H - T_C) + I^2\rho} \quad . \tag{1.24}$$

Heikes[16] showed that by taking the derivative of Equation 1.24 with respect to current and setting this to zero a current corresponding to maximum efficiency, I_{max}, can be determined;

$$\frac{\partial\varphi}{\partial I} = 0 = \frac{-\left(I^2\rho S(T_C + T_H) + 4I\rho\kappa(T_C - T_H) - 2\kappa S(T_C - T_H)^2\right)}{2I^2(I\rho - S(T_C - T_H))^2} \tag{1.25}$$

$$I_{\max} = \frac{2\sqrt{\kappa}\sqrt{\kappa\rho + 1/2S^2(T_C + T_H)}(T_C - T_H)}{S\sqrt{\rho}(T_C + T_H)} - \frac{2\kappa(T_C - T_H)}{S(T_C + T_H)} \quad . \tag{1.26}$$

Finally, substituting I_{max} back into Equation 1.24 we obtain

$$\varphi = \frac{Q}{P} = \frac{T_C}{T_H - T_C} \frac{\sqrt{1+ZT_m} - \frac{T_H}{T_C}}{\sqrt{1+ZT_m}+1} \tag{1.27}$$

where $T_m = (T_C + T_H)/2$ and we introduce the dimensionless figure of merit, ZT, to be discussed in detail in the next section

$$ZT_m = \frac{S^2}{\rho\kappa} T_m \tag{1.28}$$

or, more commonly

$$ZT_m = \frac{S^2\sigma}{\kappa_e + \kappa_L} T_m \tag{1.29}$$

where σ is the electrical conductivity and κ_e and κ_L are the electronic and lattice contributions to thermal conductivity. Similarly, we can express the efficiency, η, of power generation by dividing the power extracted by the total heat energy absorbed to obtain

$$\eta = \frac{P}{Q} = \frac{T_H - T_C}{T_H} \frac{\sqrt{1+ZT_m} - 1}{\sqrt{1+ZT_m} + \frac{T_C}{T_H}}. \tag{1.30}$$

1.4 Thermoelectric Figure of Merit

An interesting feature of the thermoelectric figure of merit is that it has no upper

limit such that as ZT approaches ∞ Equation 1.27 and 1.30 reduce to the Carnot efficiency for a heat pump and power generator respectively. An illustration of this can be seen in Figure 1.6 where the efficiency is plotted against T_H, the heat source temperature, for different ZT values as well as other energy sources such as geothermal, solar, coal and nuclear using different thermodynamic engine cycles (Rankine, Stirling, Brayton etc.).[21,22] However, despite this potential for high efficiency the best ZT values, even for state-of-the-art thermoelectric materials remain between 1 and 2.

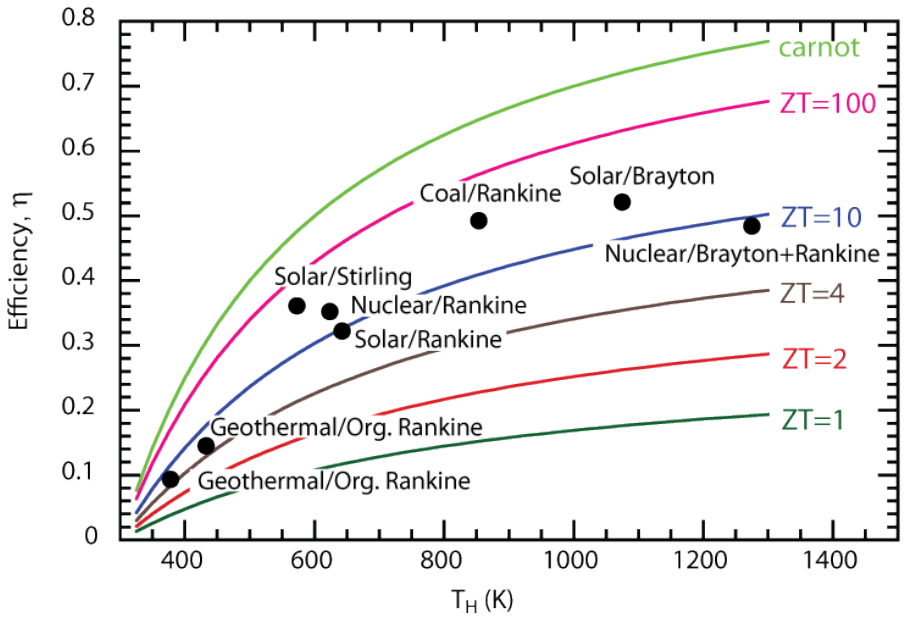

Figure 1.6. Efficiency plotted against T_H, heat source temperature, for different figure of merit values. For comparison the efficiency of other energy sources and engine cycles are included. Figure redrawn from Vining.[20]

Achieving increases in ZT are notoriously difficult as evidenced by the remarkably slow improvement over the last 60 years since Goldsmid et al. initially demonstrated thermoelectric refrigeration using Bi_2Te_3;[23] an event that began the modern era of thermoelectric materials research. The majority of thermoelectric devices still use this material and ZT values have increased only slightly.

The reason for such low ZT values is because the three materials properties involved, electrical conductivity, thermal conductivity and Seebeck coefficient are not entirely independent from one another. This interdependence can be visualized in Figure 1.7 where representative curves for the properties are depicted against carrier concentration from insulating to metallic. If, for instance, the carrier concentration is increased to enhance electrical conductivity this will reduce the Seebeck coefficient and increase the electrical contribution to thermal conductivity such that there may be no overall improvement in ZT. Typically, the highest figure of merit values are not obtained in insulators (large thermopower) or metals (large electrical conductivity), but rather in semiconductors with carrier concentrations between 10^{18} and 10^{19} cm^{-3}.[24,25]

For metals, the electrical and thermal conductivity are related through the Wiedemann-Franz law

$$L_0 = \frac{\kappa_e}{\sigma T} = \frac{\pi^2}{3}\left(\frac{k_B}{q}\right)^2 \qquad 1.31$$

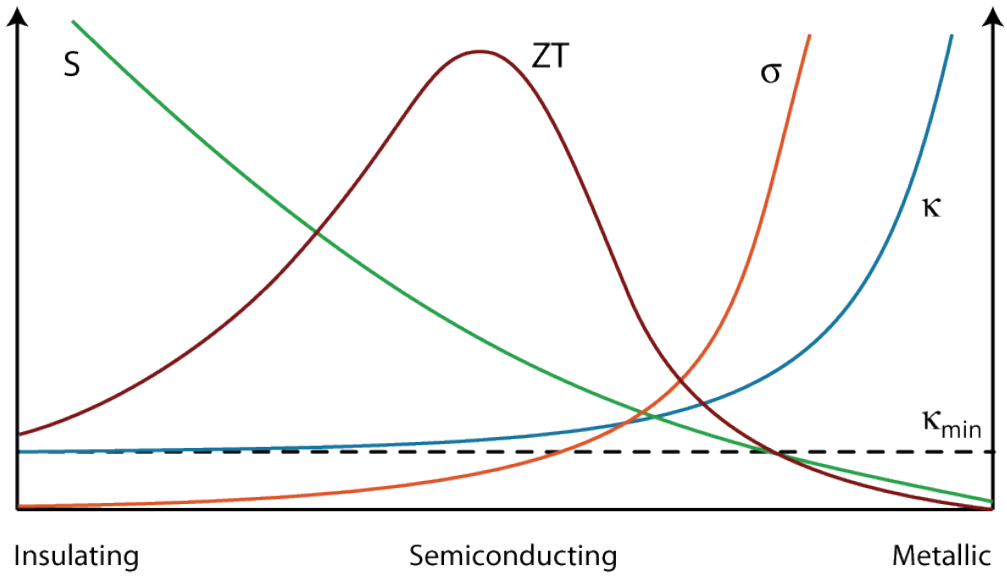

Figure 1.7. Typical trends in thermoelectric properties and figure of merit for different classes of materials. The abscissa roughly corresponds to a carrier concentration range from 10^{18}-10^{21} cm^{-3}. Figure redrawn from Snyder et al.[25]

where L_0 is the Lorenz constant equal to 2.44×10^{-8} W Ω K^{-2}. Using this relation we can rewrite Equation 1.29 as

$$ZT = \frac{S^2}{L_0}\left(\frac{1}{1+\kappa_L/\kappa_e}\right). \qquad 1.32$$

With the electrical conductivity essentially dictating the electronic contribution to thermal conductivity this leaves only the possibility of reducing the lattice contribution or increasing the Seebeck coefficient.

In an effort to maintain high electrical conductivity but reduce the lattice thermal conductivity, or heat transferred via phonons, Slack proposed the "Phonon Glass and Electron Crystal" (PGEC) concecpt.[26] Since the mid 90's virtually all the major progress in ZT for thermoelectric materials has been due to reduction in lattice thermal conductivity, rather than enhancing the electrical conductivity or thermopower. The techniques for reducing thermal conductivity are extensive and the detailed methods are beyond the scope of this dissertation. A few examples include using "rattling" structures such as clathrates[27,28] or skutterudites, [29–32] structures with point defects, [33–38] anisotropic and substructured crystals,[39–45] mass or alloy scattering,[34,38,46–50] nanoengineered materials and superlattices[26,51–65] and complex or disordered crystal structures such as zintl and half-heusler compounds.[27,28,66–69]

Having laid the groundwork for understanding thermoelectric device operation, applications, efficiency and potential we can now focus on a more detailed look at thermopower in an unconventional class of thermoelectric materials; oxides.

Chapter 2. Thermopower in Oxides

Oxide materials play an indispensable role in a wide range of technological applications including electronics, magnetic devices, sensors, fuel cells, refractories, thermal barrier coatings, optical devices, biomaterials and many more. Nevertheless, oxides were initially overlooked in the search for high ZT materials because, typically insulators, they exhibit very low electrical conductivity and most also have a low average atomic mass relative to many traditional thermoelectric materials and therefore a higher atomic vibration frequency and thermal conductivity. In this chapter the potential advantages for oxide thermoelectric materials will be highlighted and a case will be made for their use in place of traditional semiconductor materials based on the large Seebeck coefficient values that can be obtained. A survey of the relevant literature will be presented and the fundamentals governing thermopower in band conducting and small-polaron conducting oxides will be described.

2.1 Why Oxides?

By far the most commonly used thermoelectric material is Bi_2Te_3 alloyed with either Sb or Se with an estimated production of 30 tonnes annually. The next largest in production is PbTe at 2-4 tonnes annually. The reliance on these materials is troublesome

partly because of their toxicity (Sb, Se, Pb), which will limit some applications, but more so because of the scarcity and cost of tellurium which at 1 ppb in the earth's crust is even rarer than platinum (37 ppb). The USGS classifies tellurium as one of the nine rarest metals[70] and the DOE lists it as a critically scarce energy material.[71] Tellurium is not mined independently, but is an anodic byproduct of copper refining. Because of its scarcity and increasing use in technology, such as CdTe solar panels, the cost of tellurium has risen dramatically from 3.86$/lb in 2000 to over 150$/lb now.[72] Many traditional thermoelectric materials are also limited to operation at lower temperatures to avoid sublimation, oxidation or decomposition. In comparison, oxide thermoelectrics generally benefit from being non-toxic, relying on more abundant transition metals, having very good high temperature stability and corrosion resistance and facile synthesis.

Moreover, many of the best thermoelectric materials, such as Zintl compounds and clathrates, exhibit thermal conductivity nearing the theoretical minimum thermal conductivity, κ_{min}. A phonon wavelength cannot be arbitrarily small because the wave consists of displaced atoms and a wavelength shorter than the interatomic distance is not physically meaningful. As a result, further reduction in κ_L and subsequent increase in ZT are approaching their limit. Furthermore, the nanostructured features necessary for many phonon scattering approaches are unstable at high temperature and prone to coarsening which leads, in turn, to a reduction in ZT. Having minimized the denominator in Equation 1.29, future approaches to increase ZT must include an increase in the numerator, the power factor, σS^2.

2.2 Band Conductors

Degenerately doped semiconductors have metallic-like electrical resistivity and the Seebeck coefficient is characteristically linear with respect to temperature. For oxides fitting these criteria it is possible to apply the thermopower expression for a single band metal. To do so we rely on the Mott formula[73] relating thermopower to the energy partial differential of the electrical conductivity evaluated at the Fermi energy. This expression can be derived from the basic electrical and thermal current transport equations involving an electric field and thermal gradient

$$j_e = L_{11}\nabla\varepsilon + L_{12}\nabla T \tag{2.1}$$

$$j_{heat} = L_{21}\nabla\varepsilon + L_{22}\nabla T \tag{2.2}$$

We notice at once that these equations are simply generalized forms of Equations 1.6 and 1.7 that were derived in the last chapter. Thermopower is the ratio of the matrix elements

$$S = \frac{-L_{21}}{L_{11}} \tag{2.3}$$

where

$$L_{11} = \sigma \tag{2.4}$$

$$L_{21} = T L_{12} = \frac{\pi^2 (k_B T)^2}{3q} \frac{\partial \sigma(E)}{\partial E}\bigg|_{E=E_F} \tag{2.5}$$

such that

$$S = \frac{\pi^2}{3} \frac{{k_B}^2 T}{q} \frac{\partial \ln[\sigma(E)]}{\partial E}\bigg|_{E=E_F}. \tag{2.6}$$

The electrical conductivity of a single band metal with parabolic band approximation is given by [74]

$$\sigma(E) = \frac{2q^2}{3m} \int N(E) \tau E \frac{df(E)}{dE} dE \tag{2.7}$$

where m is the effective mass of the carrier, τ is the carrier scattering time, $f(E)$ is the Fermi-Dirac distribution (Equation 1.3) and $N(E)$ is the density of states. Expressing Equation 2.7 in terms of the density of states and carrier concentration, n, we have [75]

$$S = \frac{\pi^2}{3} \frac{{k_B}^2 T}{q} \frac{N(E)}{n}\bigg|_{E=E_F}. \tag{2.8}$$

The inverse dependence on carrier concentration alluded to in Figure 1.7 is now clear. Similarly, expressing electrical conductivity in terms of carrier mobility, ν, concentration, n or p, and charge, q, we see the proportional dependence on carrier concentration

$$\sigma = nq\upsilon_n, \ \sigma = pq\upsilon_p . \qquad 2.9$$

The carrier mobility itself depends on the effective mass of the carrier and the carrier collision time (or time between scattering events) as

$$\upsilon_n = \frac{q\tau_n}{m_n}, \ \upsilon_p = \frac{q\tau_p}{m_p} . \qquad 2.10$$

Examining Equations 2.8 and 2.9 and acknowledging the inherent performance trade-off with respect to carrier concentration, it becomes evident that an increase in power factor ($S^2\sigma$) for band conducting oxides must rely on one of three approaches: increasing the density of states in the vicinity of the Fermi level, increasing the time between collisions or minimizing the effective mass of the carrier.

In 1993 Hicks and Dresselhaus identified quantum confinement as a route by which the density of states could be sharpened leading to an increase in Seebeck coefficient.[76] However, experiments have yet to show definitively that enhancement in ZT in nanostructured materials is actually due to increased Seebeck coefficient, more likely is that the nanostructuring (multiple quantum wells devices of Eu doped PbTe for example) imposed interfaces that effectively scattered phonons, reducing κ_L.[77–80]

The strong ionic character of oxides resulting from the large difference in electronegativity between cations and oxygen has meant low carrier mobility (short scattering times, narrow bands, high effective mass) relative to traditional semiconductors

for degenerately doped semiconducting oxides.[81] Taken together with the lower average atomic mass (higher vibrational frequency and therefore thermal conductivity) of oxides relative to traditional materials it is not surprising that the ZT values of even the best band conducting oxide materials (Al,In,Ga)-doped ZnO,[82–88] (La,Mo,Nb,Bi,Yb)-doped $CaMnO_3$,[89–98] (Nb,La)-doped $SrTiO_3$ perovskites,[99–103] (Ge,Ni,Cu,Mg,Ca,Sn,Zn)-doped In_2O_3, [82,104–108] or La-doped $Sr_2Nb_2O_7$ [40,109] are still inferior to traditional thermoelectric materials.

2.3 Strongly Correlated Systems

In 1997 Terasaki et al.[42] found that $NaCo_2O_4$ crystals exhibited metallic electrical conductivity (0.2 mΩ cm) and, shockingly, had the large value for thermopower of 100 μV/K. Of equal surprise was that the Seebeck coefficient didn't have the characteristic linear temperature dependence, but rather, at high temperatures the thermopower transitioned to roughly 200 μV/K (see Figure 2.1).[110]

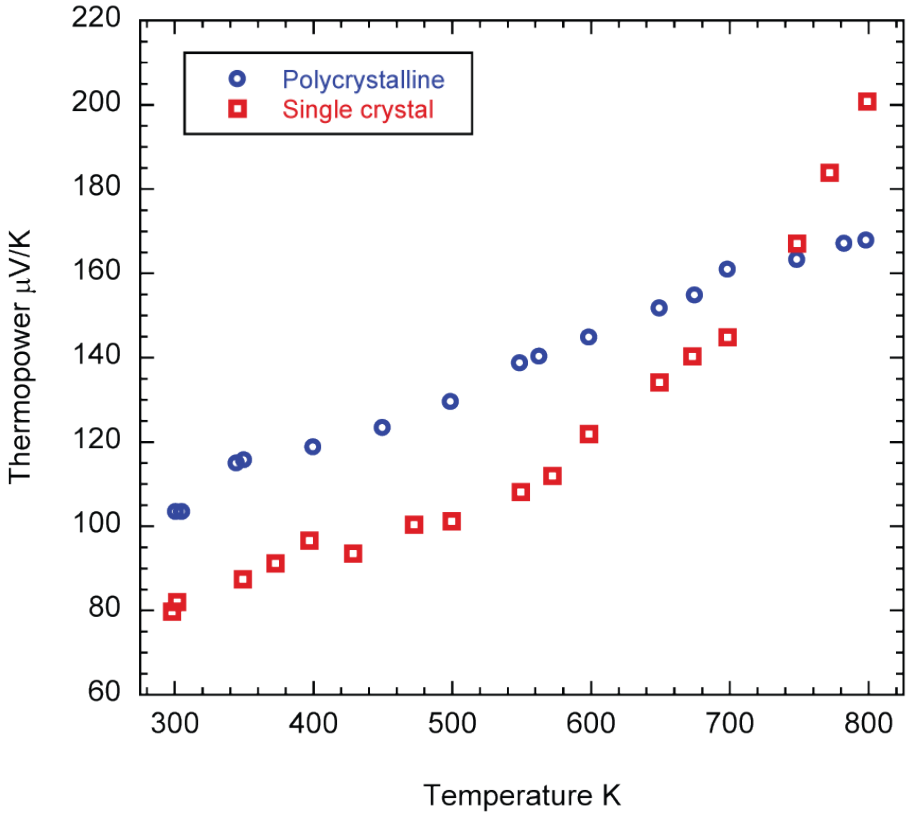

Figure 2.1. Thermopower plotted as a function of a temperature for polycrystalline and single crystal $NaCo_2O_4$ samples. Figure redrawn from Fujita et al.[110]

This large thermopower at high temperatures (~800K), taken with the metallic electrical conductivity gave $NaCo_2O_4$ a ZT of ~1, a dramatic improvement over previous oxide thermoelectrics and one that made oxides competitive with traditional thermoelectric materials. The origin of this thermopower in a material with such a large carrier density (~10^{22} cm^{-3}) was at the time completely unknown. For example, the original high temperature formula for thermopower proposed by Heikes in 1961 [16] and bearing his name is given by

$$S = \frac{k_B}{q} \ln\left(\beta \frac{y}{1-y}\right) \qquad 2.11$$

where y is the carrier concentration and β is an electronic degeneracy parameter. This expression was unable to adequately explain both the magnitude and temperature dependence in $NaCo_2O_4$. As the next section will describe, in strongly correlated materials, or ones where the charge carrier interactions must be included, the physics of thermopower are significantly modified.

Eventually, in 2000 Koshibae et al.[111–114] proposed a modified version of the Heikes formula which accounted for the often overlooked spin and orbital contributions to entropy and therefore thermopower. The modification also considered the large exchange of entropy between the two ions involved in conduction on sites (I) and (II) and therefore includes the ratio of electronic degeneracy, $g_{(I)}/g_{(II)}$, and is of the form

$$S = \frac{k_B}{q} \ln\left(\frac{g_{(I)}}{g_{(II)}} \frac{y}{1-y}\right). \qquad 2.12$$

This modified formula not only explained the large magnitude of thermopower in $NaCo_2O_4$, but also accounted for a low-spin (LS) to high-spin (HS) transition in spin state (mitigated by increasing thermal energy) which provided the alteration in spin and orbital degeneracy to explain the thermopower temperature dependence. The detailed derivation

of Koshibae et al.'s modified Heikes formula will be detailed in Section 2.3.1 and its application to $NaCo_2O_4$ will be laid out in Section 2.3.2.

Naturally, in the wake of measuring such remarkable thermoelectric properties in $NaCo_2O_4$ many other strongly correlated oxide systems were examined. To date, Koshibae et al.'s modified Heikes formula has described the thermopower of many compounds such as $NaCo_2O_4$[115–120] and other structures[116,121–130] containing edge-shared CoO_2 layers such as $Ca_2Co_2O_5$, $Ca_3Co_4O_9$ or members of the (Bi,Pb)-(Ca,Sr,Ba)-Co-O system, cobalt perovskites $La_{1-x}Sr_xCoO_3$,[131] layered rhodium oxides,[132,133] orthochromites,[134,135] manganese perovskites $Pr_{0.5}Ca_{0.5}MnO_3$ and double-perovskites $Ca(Mn_{3-y}Cu_y)Mn_4O_{12}$ [136] and spinels $LiMn_2O_4$,[137] Co_3O_4,[138] iron based structures $SrFeO_x$,[139] and $RBaCo_2O_{5+x}$ (R=Gd, Nd).[140]

2.3.1 Thermopower Due to Spin and Orbital Degeneracy

Thermopower is frequently used as a means to determine the sign and concentration of carriers in metals and semiconductors because thermopower is a measurement of the entropy per carrier in a system. An oversimplification often occurs where only the entropy from charge is considered ignoring the fact that the carriers also have spin and orbital degrees of freedom. Including these components is key to Koshibae et al.'s modified Heikes formula for thermopower in strongly correlated systems.

Before we begin discussing the role of spin and orbital degeneracy we must derive modified dynamical thermoelectric linear response expressions. The linear response expressions shown in Equations 2.1 and 2.2 do not satisfy Onsager's reciprocity

relation, $L_{12} \neq L_{21}$. Following Koshibae et al. [114] we consider an irreversible system with a net generation of entropy and in addition to electric potential and temperature gradient we include the chemical potential as particles move from the hot to the cold side. When N particles and ΔE energy is transferred from the hot to cold side of a thermoelectric system the change in entropy on the cold and hot sides are given by

$$s_{cold} = -\frac{\Delta E}{T} + \frac{\mu(T)}{T} N \tag{2.13}$$

$$s_{hot} = -\frac{\Delta E}{T + \Delta T} - \frac{\mu(T + \Delta T) - q\Delta\varepsilon}{T + \Delta T} N \,. \tag{2.14}$$

The rate of change of entropy is then

$$\frac{ds}{dt} = \frac{d(s_{cold} + s_{hot})}{dt} = \frac{d(\Delta E)}{dt}\left(-\frac{\Delta T}{T^2}\right) + \frac{dn}{dt}\left[\frac{q}{T}\Delta\varepsilon - \Delta T \frac{\partial}{\partial T}\left(\frac{\mu}{T}\right)\right]. \tag{2.15}$$

On the right hand side of Equation 2.15 we see the particle and energy current, dn/dt and d(ΔE)/dt, multiplied by coefficients allowing us to express the driving forces for particle and energy currents

$$\frac{q}{T}\Delta\varepsilon - \Delta T \frac{\partial}{\partial T}\left(\frac{\mu}{T}\right) = \Delta x\left[\frac{q}{T}\frac{\partial\varepsilon}{\partial x} - \frac{\partial}{\partial x}\left(\frac{\mu}{T}\right)\right] \tag{2.16}$$

$$-\frac{\Delta T}{T^2} = \Delta x \frac{\partial}{\partial x}\left(\frac{1}{T}\right). \tag{2.17}$$

With these generalized driving forces we are now able express the dynamical thermoelectric response expressions

$$j_1 = M_{11}\left[\frac{q}{T}\frac{\partial \varepsilon}{\partial x} - \frac{\partial}{\partial x}\left(\frac{\mu}{T}\right)\right] + M_{12}\frac{\partial}{\partial x}\left(\frac{1}{T}\right) \tag{2.18}$$

$$j_2 = M_{12}\left[\frac{q}{T}\frac{\partial \varepsilon}{\partial x} - \frac{\partial}{\partial x}\left(\frac{\mu}{T}\right)\right] + M_{22}\frac{\partial}{\partial x}\left(\frac{1}{T}\right) \tag{2.19}$$

where j_1 and j_2 represent particle and energy flux densities. These expressions now satisfy Onsager's reciprocity relation, $M_{12} = M_{21}$. At steady state there are electric and diffusive forces but there is also an interference between the heat and electric currents.[114] The expression for thermopower in steady state ($j_1 = 0$) can be determined as the ratio of the gradients of electro-chemical potential and the temperature

$$-\left(\frac{\partial \varepsilon}{\partial x} - \frac{1}{q}\frac{\partial \mu}{\partial x}\right) = \left(-\frac{1}{qT}\frac{M_{12}}{M_{11}} + \frac{\mu}{eT}\right)\frac{\partial T}{\partial x} = S\frac{\partial T}{\partial x} \tag{2.20}$$

therefore

$$S = -\frac{1}{qT}\frac{M_{12}}{M_{11}} + \frac{\mu}{qT}. \tag{2.21}$$

The first term on the left hand side of Equation 2.21 has kinetic coefficients which are experimentally determined. Fortunately, we will now show that these kinetic coefficients are approximately constant at high temperatures meaning the first term

approaches zero. Using the Kubo formalism, an application of an external perturbation on linear response, the Hamiltonian in the Hubbard model can be written as

$$H = \bar{t} \sum_{\langle I,II \rangle \varsigma} \left(c^{*}_{I\varsigma} c_{II\varsigma} + c^{*}_{II\varsigma} c_{I\varsigma} \right) + J \sum_{I} \left(\vec{s}_{I} \ \vec{s}_{I+1} \right) \qquad 2.22$$

where $\bar{t}$ is the transfer integral of an electron between neighboring sites, $c^{*}_{I\varsigma}$ and $c_{II\varsigma}$ are creation and annihilation operators for electrons of spin ($\varsigma = \uparrow, \downarrow$) at sites I and $I + 1 = II$. J is the antiferromagnetic superexchange interaction between neighboring spins. The transport coefficients M_{1b} $(b = 1,2)$ are defined as

$$M_{1b} = \int_{0}^{\infty} dt \int_{0}^{1/k_B T} d\tau \ Tr\left[e^{-(H-\mu N)/k_B T} \, j_1(-t - i\tau) j_b \right] \qquad 2.23$$

where N is the number of electrons, Tr is the trace, or summation over a complete set of states, j_b $(b = 1,2)$ is the particle and thermal flux operators. At high temperatures $t, J \ll k_B T$ or $t \ll k_B T \ll J$ then M_{11} and M_{12} can be considered constant Equation 2.21 reduces to

$$S = \frac{\mu}{qT} . \qquad 2.24$$

If we apply the thermodynamic identity for chemical potential

$$\frac{\mu}{T} = -\left(\frac{\partial s}{\partial N}\right)_{E,V}. \qquad 2.25$$

where s is entropy and N is the number of particles we can rewrite Equation 2.24 as

$$S = -\frac{1}{q}\left(\frac{\partial s}{\partial N}\right)_{E,V}. \qquad 2.26$$

As $T \to \infty$ entropy can be written as $k_B ln(g)$ where g is the electronic degeneracy, not Gibbs free energy. Substituting this in Equation 2.26 we obtain

$$S = -\frac{k_B}{q}\left(\frac{\partial \ln(g)}{\partial N}\right)_{E,V}. \qquad 2.27$$

The degeneracy is calculated as follows. Each site has two orbitals that can either be occupied or doubly occupied; these conditions will be labeled (I) and (II) respectively. The total number of ways to arrange these two kinds of sites is given by [112]

$$g = \left[g_{(I)}\right]^{2L-N}\left[g_{(II)}\right]^{N-L}\frac{L!}{(N-L)!(2L-N)!} \qquad 2.28$$

where $g_{(I)}$ and $g_{(II)}$ are the degeneracies of sites (I) and (II) and N is the number of electrons in L unit cells. Applying Stirlings approximation to Equation 2.28 we finally can rewrite Equation 2.27 as

$$S = \frac{k_B}{q}\left(\ln\left[g_{(I)}\right] - \ln\left[g_{(II)}\right]\right) - \frac{k_B}{q}\ln\left(\frac{y}{1-y}\right) \qquad 2.29$$

where $y = 2 - N/L$ or, more simply

$$S = \frac{k_B}{q}\ln\left(\frac{g_{(I)}}{g_{(II)}}\frac{y}{1-y}\right) \qquad 2.30$$

which is the same as Equation 2.12; Koshibae et al.'s modified Heikes formula. Equation 2.30 demonstrates fraction of conducting sites, y/(1-y) plays an important role in both the

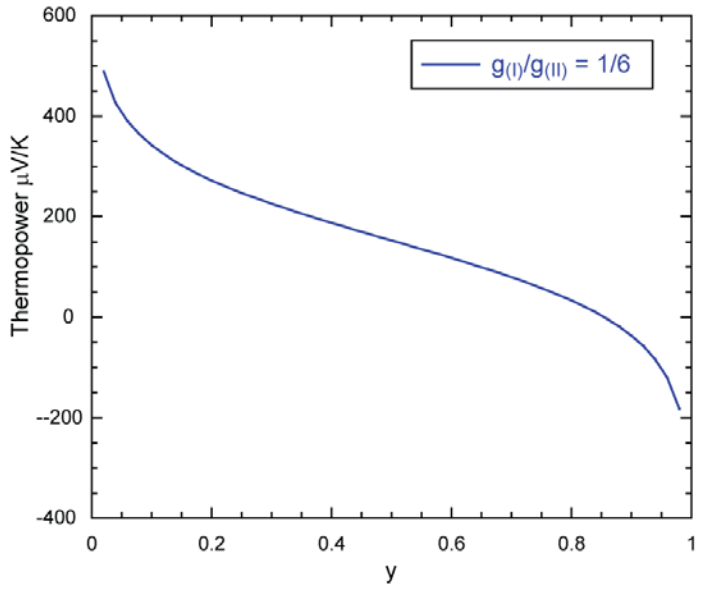

Figure 2.2. Thermopower calculated from Koshibae et al.'s modified Heikes formula plotted against carrier concentration.

magnitude and the sign of a material's thermopower (see Figure 2.2). Equally important, however, is the ratio of the electronic degeneracies for the ions involved in conduction. A large ratio in degeneracy yields a large contribution to thermopower from spin and orbital entropy.

2.3.2 Thermopower in $NaCo_2O_4$ and derivative structures

The crystal structure of $NaCo_2O_4$ was identified in 1974 by Jansen and Hoppe.[141] The compound crystallizes in the $P6_3/mmc$ space group and consists of a naturally divided unit cell with layers of edge shared CoO_2 octahedra (CdI_2 type, triangular lattice) separated by filled or partially filled layers Na atoms (see Figure 2.3). The sodium atoms donate their valence electron to the CoO_2 layer explaining the large carrier density (~10^{22} cm^{-3}).

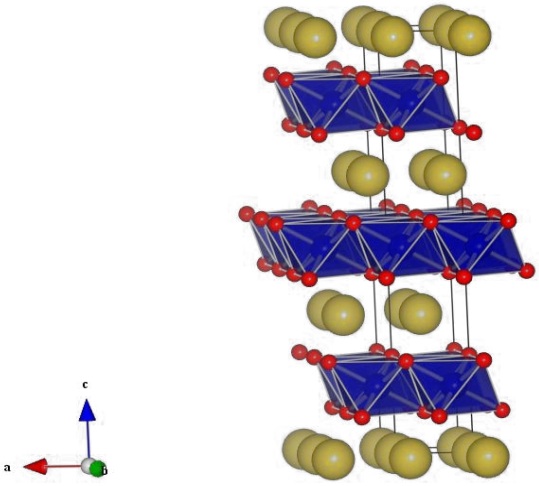

Figure 2.3. Crystal structure of $NaCo_2O_4$. Yellow atoms are sodium, blue-red octahedral are CoO_6.

For the stoichiometric compound the average oxidation state of the Co ion is +3.5. Since ions can't have half of an electron this really implies that there is equal numbers of Co^{3+} and Co^{4+} or Co ions with 6 and 5 d shell electrons, respectively. Because of electron shell overlap from the 2p orbitals of surrounding oxygen atoms (octahedral crystal field) the 5 d shell orbitals for the cobalt ion split into two bands: a lower energy, triply degenerate t_{2g} band (d_{xy}, d_{yz}, and d_{xz}) and a higher energy, doubly degenerate e_g band ($d_{x^2-y^2}$ and d_{z^2}). The different ways in which Co^{3+} and Co^{4+} can arrange their electrons in these bands are shown in Figure 2.4 along with the electronic degeneracy calculated as the product of spin and orbital degeneracy

$$g = g_{spin} g_{orbital} . \tag{2.31}$$

and

$$g_{spin} = 2\zeta + 1 \tag{2.32}$$

where ζ is the total spin and $g_{orbital}$ is simply the number of configurations possible for distributing spins between energy states.

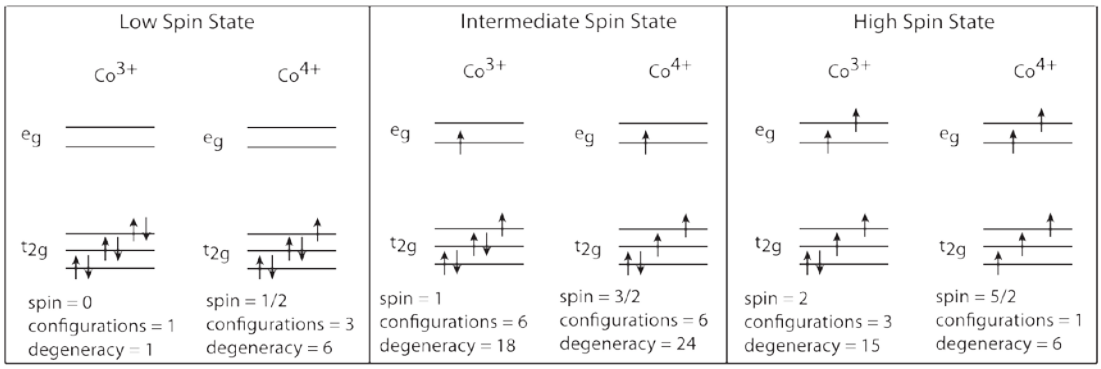

Figure 2.4. Electronic degeneracy of Co^{3+} and Co^{4+} ions in an octahedral crystal field with low, intermediate and high spin states. The total spin, number of configurations and electronic degeneracy are calculated.

Consider electron hopping between cobalt ions in the low spin (LS) state. The t_{2g} band of the Co^{3+} ion is completely filled but the Co^{4+} ion has an unfilled band and acts as a hole donor. For a stoichiometric compound, $y = [Co^{3+}] = [Co^{4+}] = 0.5$, applying the electronic degeneracies, $g_{3+} = 1$ and $g_{4+} = 6$ and substituting into Equation 2.30 the calculated thermopower is

$$S = -\frac{k_B}{e}\ln\left(\frac{1}{6}\frac{0.5}{1-0.5}\right) = 154\mu V/K \qquad 2.33$$

which agrees fairly well with the low temperature experimental thermopower of 100 μV/K.[42] Notably, as an electron hops from a Co^{3+} to a Co^{4+} the sites exchange a large entropy and the electron current flows opposite the current of entropy. At high temperatures magnetic measurements suggest a spin state transition in Co^{4+} ions from low spin to high spin (HS).[142,143] If both LS and HS states are available to Co^{4+} ions then

the total electronic degeneracy is $g_{4+} = 6 + 6 = 12$ and the calculated thermopower would be

$$S = -\frac{k_B}{e}\ln\left(\frac{1}{12}\frac{0.5}{1-0.5}\right) = 214\mu V / K \qquad 2.34$$

in good agreement with the experimental thermopower at high temperatures (200 μV/K).

2.4 Modified Heikes Formula as a Screening Tool for New Materials

In the previous section we discussed the unusually large thermopower discovered in $NaCo_2O_4$ and derived the governing equations for thermopower accounting for both spin and orbital degeneracy in strongly correlated systems. A number of new oxides related to $NaCo_2O_4$ have been identified with large ZT values, particularly single crystals, but efficiencies are still too low in bulk, polycrystalline ceramics. Additionally, some authors have suggested that a 'spin blockade' phenomenon (shown in Figure 2.5) can lead to systematically lower efficiencies in n-type materials relative to their p-type counterparts.[24] Spin blockade occurs when the transport of an electron would lower the spin state to an energetically unfavorable transient state thus restricting electrical current.[144,145] Finally, a relatively small number of ion pairs, such as Co^{3+} and Co^{4+}, have been examined and almost all compounds have featured ions in octahedral crystal fields. There exists an opportunity to establish a methodology using Koshibae et al.'s modified Heikes formula to screen for new high efficiency oxide materials looking, in particular, towards new ion pairs and different crystal fields.

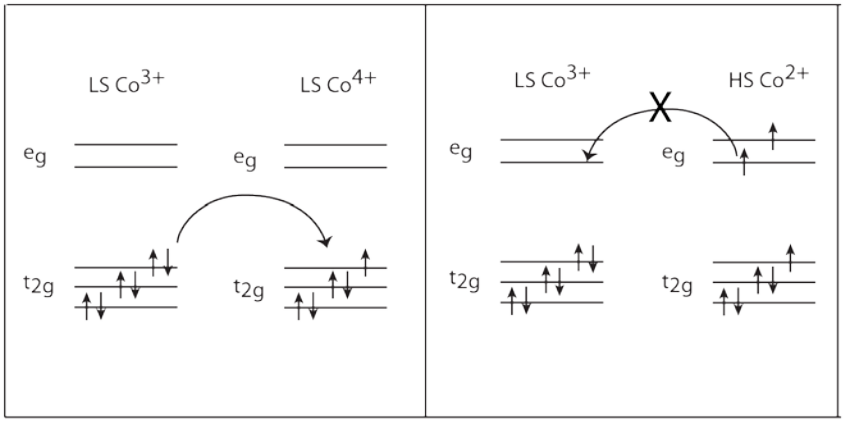

Figure 2.5. The spin blockade phenomenon. Redrawn from Hébert and Maignan.[24]

2.4.1 Alternate Crystal Fields

The majority of transition metals crystallize in structures where they are octahedrally coordinated by anions. In fact, the (MO_6) (M=cation) octahedral unit is a fundamental building block for an enormous variety of compounds and structures. Structures exist where these polyhedra are corner shared (perovskites), edge shared (cordierite) and even face shared (sapphire).[146] Nevertheless, many other coordinations are possible depending on the size and bonding of the cation. Some examples include, tetrahedral, rhombohedral, dodecahedral, cubic, trigonal bipyramidal, planar, pyramidal etc. The crystal fields for a few of these alternative coordinations are determined by ligand field theory and are shown in Figure 2.6.

In Section 2.3.1 we explained why it isn't sufficient for a material to have large values for $g_{(I)}$ and $g_{(II)}$, but rather, the ratio of $g_{(I)}/g_{(II)}$ must also be large in order to achieve an enhancement in thermopower. However, not all crystal fields are equally

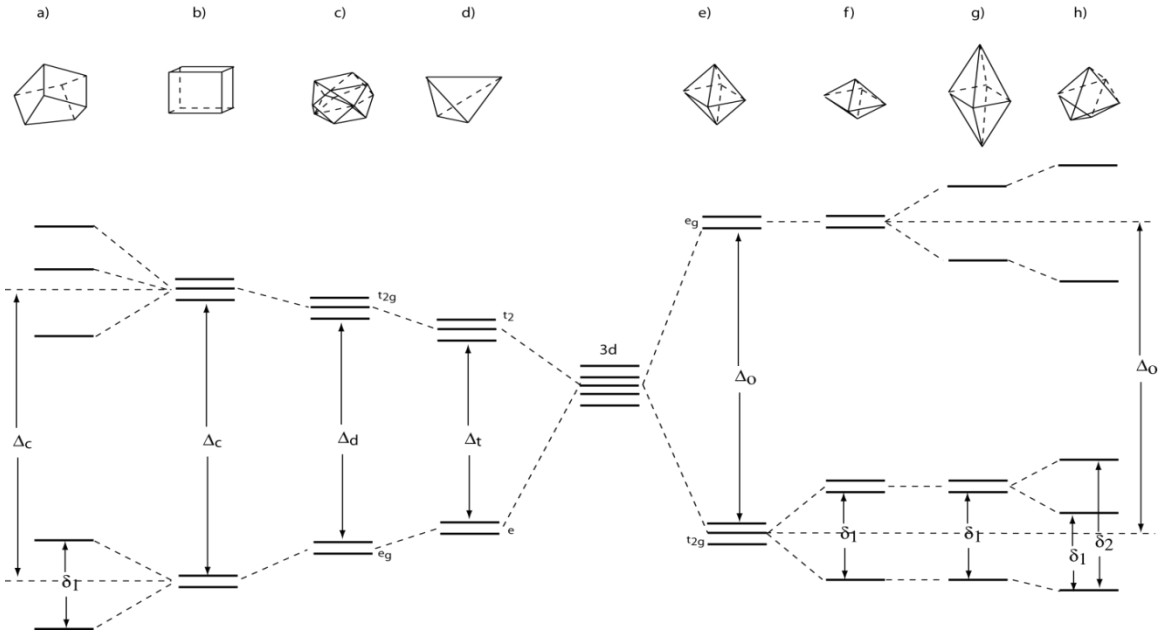

Figure 2.6. The crystal fields for a variety of different coordinations. From left to right (a) distorted cubic, (b) cubic, (c) dodecahedral, (d) tetrahedral, (e) octahedral, (f) trigonally distorted octahedral, (g) tetragonally distorted octahedral and (h) highly distorted six-coordinate. Figure adapted from Burns.[147]

suited to yield large ratios in thermopower. The octahedral crystal field, for example, benefits largely from the triply degenerate t_{2g} band. For a LS d^6 ion the t_{2g} band is filled and spin is zero yielding the lowest possible degeneracy value, 1, but if an electron is either added or removed the total spin becomes ½ and the orbital degeneracy increases to 2 or 3 for the e_g and t_{2g} bands respectively. This advantage is also present in tetrahedral, cubic and dodecahedral crystal fields which can be thought of as the opposite of octahedral field; the e band is now the lower energy band and the t_2 band is higher. Note that tetrahedral coordinations lack a center of symmetry so the g subscript in the e_g and t_{2g} bands is removed in Point Group nomenclature.

Another distinction is that the crystal field stabilization energy (CFSE), sometimes called 10dq, Δ, and defined as the energy distance between the bands is different for tetrahedral, dodecahedral, cubic and octahedral crystal fields. In general the CFSE increases in the same order $\Delta_t < \Delta_d < \Delta_c < \Delta_o$. Electron occupancy is ultimately the result of a competition between Hund's Rule coupling and CFSE. The implication is that relative to the octahedral crystal field, less thermal energy is necessary to allow ions to stabilize in intermediate or high spin states. This, too, could be advantageous for tetrahedral, cubic or dodecahedrally coordinated ions. If multiple spin states are stabilized then the degeneracies of each state would sum together and could potentially result in very large total electronic degeneracies. This was the case for $NaCo_2O_4$ at very high temperatures where both LS, $g_{(Co^{4+})} = 6$, and HS, $g_{(Co^{4+})} = 6$, Co^{4+} ions are stabilized and the total degeneracy was effectively doubled, 12. One prospective combination of d shell electrons in the tetrahedral/cubic/dodecahedral coordination is d^3 (LS+HS) and d^4 (LS) with a degeneracy ratio of 16/1 and a calculated thermopower of -240 μV/K (see Figure 2.7). A complete list of candidate ion combinations and their degeneracy values, calculated thermopower and possible crystal structures will be presented in the next section.

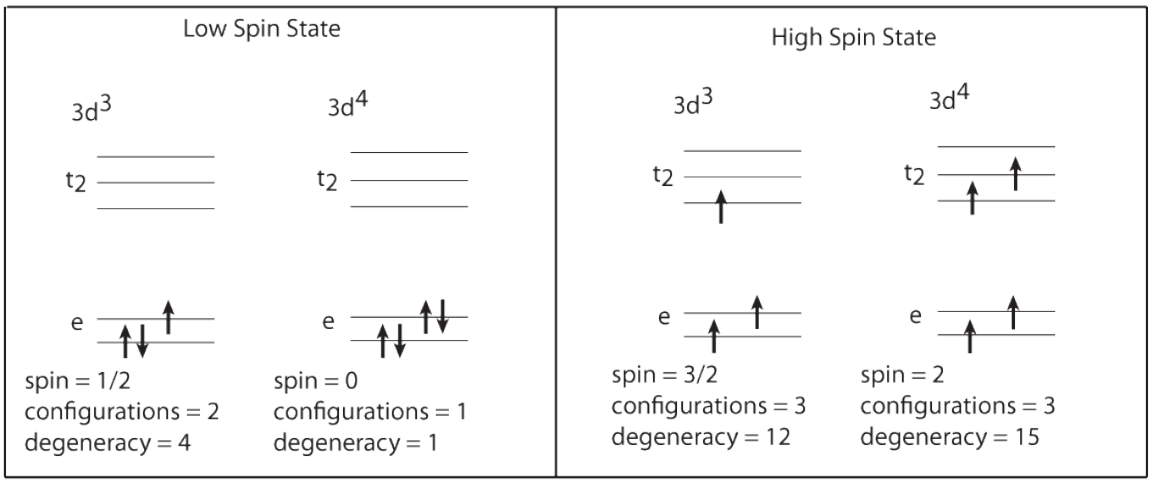

Figure 2.7. Low and high spin states for d^3 and d^4 ion combinations in a tetrahedral/cubic/dodecahedral crystal field. Spin, configurations and degeneracy are calculated. (for cubic and dodecahedral the nomenclature e_g and t_{2g} are used.)

Another interesting possibility is exploring thermopower in the rare-earth elements because the bonding electrons in the actinides and lanthanides are f shell rather than d shell. The presence of two additional orbitals could potentially lead to enhancement in electronic degeneracy ratios. The crystal field for f^2 and f^3 electrons in an octahedral crystal field is shown in Figure 2.8. At first glance there appears to be a good opportunity for large degeneracy ratio; LS $4f^2$ & LS, HS, or LS+HS $4f^3$ is 1/6, 1/12 or 1/18 respectively. However, due to shielding from 5s and 5p shells the 4f shell electrons do not strongly overlap with the orbitals of surrounding ions and therefore the crystal field effects are rather weak.

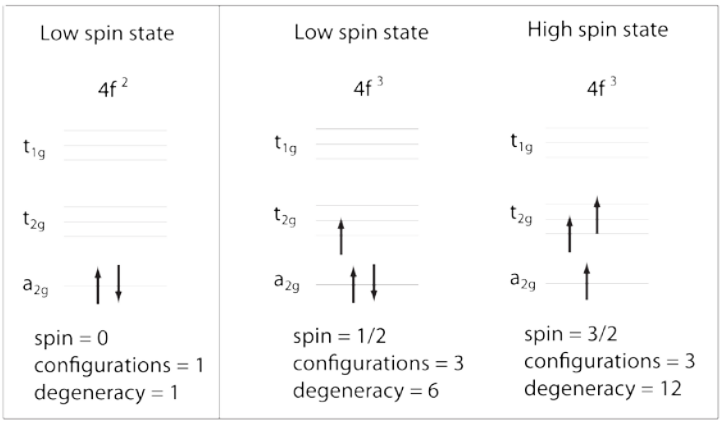

Figure 2.8. Crystal field for f shell orbitals in an octahedral crystal field. The $4f^2$ (LS) and $4f^3$ (LS and HS) configurations are shown to demonstrate the large ratio in spin and orbital degeneracy possible. The t_{2g} band is $f_{x(y^2-z^2)}$, $f_{y(x^2-z^2)}$, and $f_{z(x^2-y^2)}$ orbitals, the t_{1g} band is f_{x^3}, f_{y^3}, and f_{z^3}orbtials, and the a_{2g} band is the f_{xyz} orbital.

2.4.2 Selecting Transition Metal Ion Pairs

Identifying the electronic configurations such as $3d^3$ and $3d^4$ with potential for large degeneracy ratios is only the first step in screening for new oxide thermoelectric materials. Transition metal ions typically have multiple oxidation states and, therefore, a number of different elements might be suitable for a given electronic configuration. To achieve $3d^3$ and $3d^4$ configurations, for example, combinations of either $Cr^{2+/3+}$ or $Mn^{3+/4+}$ would be satisfactory.

To determine which ion pair combination is best suited to achieve an electronic configuration in a specific stereochemistry, or coordination, it is helpful to examine the ionic radii. Many experiments have been performed to accurately determine ionic radii in different coordinations and oxidation states and extensive tables of values now exist.[148–

[152] If a radii value has not been reported for a given coordination and oxidation state it may be an indicator that the arrangement is not thermodynamically favorable. Table 2.1 reports the ionic radii values for candidate ion pairs and we observe that ionic radii for the ions in dodecahedral sites are not available (NA) indicating they are too small for this site. In fact, only the largest fit in a cubic site. Rather than searching fruitlessly for a structure where Mn^{3+}/Mn^{4+} are in a cubic or dodecahedral coordination we can instead search for a structure with tetrahedral sites.

Table 2.1. Ionic radii values (Angstroms) for ion pairs of a few select electronic configurations. NA indicates that no values are available.

	Electron configuration	Ion Pair	CN=4	CN=6	CN=8	CN=12
Cubic Tetrahedral or Dodecahedral	LS + HS d^3 & LS d^4 $g_{(I)}/g_{(II)}$ = 16/1	Cr^{2+} / Cr^{3+}	NA/0.41	0.73/0.61	NA	NA
		Mn^{3+} / Mn^{4+}	NA/0.39	0.58/0.53	NA	NA
	LS d^4 & LS + HS d^5 $g_{(I)}/g_{(II)}$ = 1/12	Mn^{2+} / Mn^{3+}	0.66/NA	0.67/0.58	0.96/NA	NA
		Cr^{2+} / Mn^{2+}	NA/0.66	0.73/0.67	NA	NA
		Mn^{3+} / Fe^{3+}	NA/0.49	0.58/0.55	NA/0.78	NA
		Fe^{3+} / Fe^{4+}	0.49/NA	0.55/0.58	0.78/NA	NA
Octahedral or Rhombohedral	LS d^6 & LS+HS d^7 $g_{(I)}/g_{(II)}$ = 16/1	Co^{2+} / Co^{3+}	0.58/NA	0.65/0.53	0.9/NA	NA
		Fe^{2+} / Co^{2+}	0.63/0.58	0.61/0.65	0.92/0.9	NA
		Co^{3+} / Ni^{3+}	NA	0.53/0.56	NA	NA
	d^0 & d^1 $g_{(I)}/g_{(II)}$ = 6/1	Ti^{3+} / Ti^{4+}	NA/0.42	.67/0.61	NA/0.74	NA

Table 2.2. Various ion pairs in different crystal fields with their electron degeneracy ratio, predicted thermopower and possible crystal structures for candidate materials.

Crystal Field	*d* electron combination	Ion pairs	$\frac{g_{(I)}}{g_{(II)}}$	Calculated thermopower (μV/K)	Possible crystal structure and composition
Octahedral	LS d^6 & LS+HS d^7	Co^{2+} / Co^{3+} Fe^{2+} / Co^{2+}	16/1	-240	$(Si_{1-x}Al_x)[Co]_2O_4$ $(Si)[CoFe]O_4$ $(Co)[Co]_2O_4$
	LS d^0 & LS d^1	Ti^{3+} / Ti^{4+}	6/1	-154	$(A)[Ti]_2O_4$ (A=Li,Na)
	LS d^5 & LS+HS d^6	Fe^{3+} / Co^{3+}	1/12	214	$(Fe,Co)_2Si_3O_9$
Tetrahedral Cubic or Dodecahedral	d^3 & d^4	Cr^{2+} / Cr^{3+} Mn^{3+} / Mn^{4+}	16/1	-240	$(Mn)[Ni_{1-x}Cr_x]_2O_4$
	d^4 & d^5	Fe^{3+} / Fe^{4+} Mn^{2+} / Mn^{3+} Mn^{3+} / Fe^{3+}	1/12	214	$(Mn_{1-x}Fe_x)[NiCr]O_4$

Once the appropriate ions have been selected a crystal structure hosting these ions in the desired site can be identified. Table 2.2 lists candidate crystal structures likely to benefit from enhanced thermopower using Koshibae et al's modified Heikes formula.

After describing synthesis and characterization in the next chapter we will describe our experiments to further explore thermopower with respect to its structure, crystal field and spin in strongly correlated spinels.

Chapter 3. Synthesis and Characterization: Tools and Techniques

Previous chapters gave an overview of thermoelectrics describing their operation, efficiency and materials guidelines and then went on to explain in detail the origin and governing equations for thermopower in band conducting oxides as well as strongly correlated systems. Finally, the effect of spin and orbital entropy on thermopower was illustrated and a screening methodology was developed to identify oxide compounds that could exhibit large thermopower. This chapter describes the synthesis routes and characterization tools and techniques employed to investigate new oxide thermoelectric materials. The methods used for materials synthesis, densification and characterization are quite standard and many detailed texts describing them are available. Nevertheless, an overview of the basic principles involved as well as the details regarding application of a tool or technique to a specific oxide material system is useful.

3.1 Synthesis of Compounds

Let us begin with the synthesis of new materials. The materials science community is continually developing new and innovative routes to synthesize materials with improved or unique properties, specific end-shapes, or complex crystal structure and nanostructured features. Oxide thermoelectrics fall in the inorganic materials and

ceramics category with diverse synthesis techniques ranging from wet chemistry approaches to polymer derived ceramics to chemical or physical vapor deposition and many more. We will begin with one of the simplest and most common routes to prepare materials; the solid-state method.

3.1.1 Solid-state synthesis

Once a composition of interest has been identified one of the first methods used to make a sample is the solid-state method because of its relative simplicity. If the incorrect phase or impurities are obtained then more difficult approaches can be considered. The basic principle is to mix stoichiometric amounts of the constituent oxides in powder form for a given composition and then to heat the mixture and allow diffusion to achieve intimate mixing. This so-called “shake and bake” process relies on diffusion of elements at the molecular level to form a homogenous compound.

For a given temperature the mass diffusion length, L_D, can be approximated by

$$L_D = \sqrt{4Dt} \tag{3.1}$$

where t is time and D is the material’s diffusivity given by

$$D = D_0 e^{\left(-E_A/RT\right)} \tag{3.2}$$

where the prefactor, D_0, is the coefficient of diffusion, E_A is an activation energy for diffusion and R is the gas constant. The coefficient of diffusion is an experimentally

determined value that can range from 10^{-8} m^2/s for small molecules moving interstitially through a metal to 10^{-20} m^2/s for large molecules in organic materials. Oxides have a rather low melting point coefficient of diffusivity between 10^{-12}-10^{-14} m^2/s and a moderately high normalized activation energy between 22-25 $E_A / (RT_M)$.[153] Substituting these values into Equation 3.1 and 3.2 and assuming the mixture is held near the melting point for a week we observe that typical mass diffusion lengths could be as low as 5-25 nm!

The short diffusion length underscores the importance of aggressively mixing the precursor powders to minimize the diffusion length and reduce the particle size. Powders can be ground by hand in a mortar and pestle or they can be dispersed in ethanol and milled in a ball, attrition or planetary mill with milling media such as zirconia or alumina. If the powders are calcined and still aren't the correct phase or pure the powder can be milled and the process repeated. For our experiments we used the solid-state method to make the complex spinel materials $Fe_xMn_{1-x}Ni_{2-y}Cr_yO_4$ x=0, ¼, ½, ¾, 1 and y=0,1,2. However, samples of sufficient purity were only obtained for y=1 composition.

3.1.2 Coprecipitation method

A way to bypass the problem of short diffusion length in material synthesis is to rely on a wet chemistry technique such as precipitation, coprecipitation or reverse coprecipitation. In this approach the ions are dissolved entirely into a solution and intimate mixing is achieved. An important feature of all the different precipitation techniques is that the ions are dissolved at a specific pH value, normally acidic. The

solution is then mixed dropwise to a buffer solution of the opposite pH such that the dissolved ions are no longer thermodynamically stable and precipitate immediately into the solid form leaving behind an aqueous solution of the acid or base. In order to assess whether the desired ions should be dissolved in a basic or acidic solution a Pourbaix diagram can be referenced such as the one shown in Figure 3.1 for iron. A Pourbaix diagram shows the thermodynamically favorable state for an element or compound as a function of pH and potential (oxidizing or reducing conditions). The precipitate is normally an amorphous gel, oftentimes a hydroxide or nitrate that must be filtered, washed several times in alcohol and deionized water before it is dried and calcined to remove hydroxyl or nitrate groups. A benefit of the precipitate being amorphous is an increased thermodynamic driving force for crystallization upon heat treating the sample.

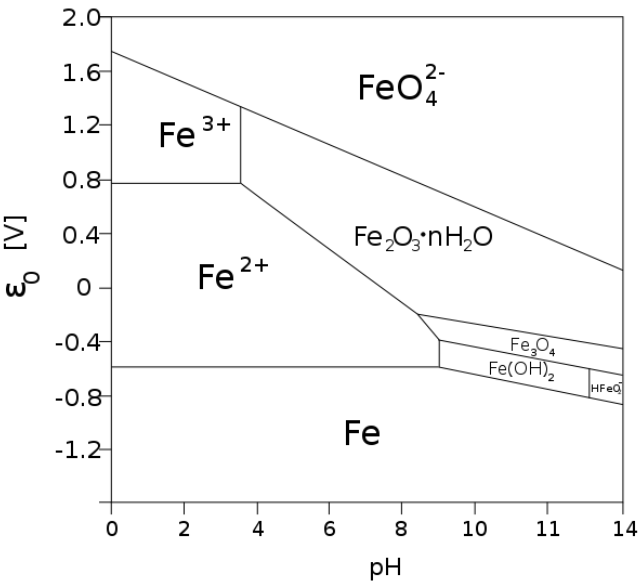

Figure 3.1. Pourbaix diagram for iron. Figure used with permission from Früh.[154]

The majority of compounds are made by dissolving salts such as nitrate precursors in water or water buffered with HNO_3. The dissociation reaction is of the form

$$M\left(NO_3\right)_y \cdot xH_2O_{(s)} = M^{y+}{}_{(aq)} + y\, NO_3^{-}{}_{(aq)}. \quad 3.3$$

Where y is the oxidation state of metal and (aq) denotes an aqueous, or dissolved species. Oxide precursors with the nominal formula $M_zO_{z*y/2}$ can also be used if nitric acid is used to help dissolve the ions via the elimination reaction (dehydration)

$$M_zO_{z*y/2\,(s)} + 2z\,H^{+}{}_{(aq)} = M^{y+}{}_{(aq)} + z\,H_2O_{(l)}. \quad 3.4$$

Commonly used bases include NaOH or NH_3OH and the final precipitation reaction could be of the form

$$M^{+}{}_{(aq)} + X^{-}{}_{(aq)} + 2H^{+}{}_{(aq)} + Na^{+}{}_{(aq)} + OH^{-}{}_{(aq)} \leftrightarrow MX_{(s)} + Na^{+}{}_{(aq)} + H_2O_{(l)} \quad 3.5$$

though amorphous hydroxides are more commonly formed. The nomenclature coprecitation or reverse coprecipitation refers to whether the ions in solution are added to the buffer solution dropwise or whether the buffer solution is added to the ion solution dropwise. One downside to the technique is dealing with insoluble ions, using immiscible liquid precursors or using multiple ions that precipitate at incompatible pH ranges as was the case for our experiments. We attempted to synthesize the $Fe_xMn_{1-x}Ni_{2-y}Cr_yO_4$ x=0, ¼, ½, ¾, 1 and y=0,1,2 series via coprecipitation but we were unsuccessful because the elements Fe, Mn, Ni and Cr only had a very narrow window of pH values ($7.5 < \delta < 8.8$)

Table 3.3. Insolubility ranges at 0 volts in pH for Fe, Mn, Ni and Cr elements and coprecipitation.[155,156]

Fe	Mn	Ni	Cr	Coprecipitation range
< 6	> 7.5	< 8.8	> 5 and < 11.5	$7.5 < \delta < 8.8$

where solids of each element would precipitate (see Table 3.3). Despite repeated attempts, after each coprecipitation was complete there still remained ions in solution evidenced by the color in the solution.

3.1.3 Combustion synthesis

The final synthesis route that I'll describe in this work is combustion synthesis. Combustion synthesis combines the relative simplicity of the solid-state method with the intimate mixing achieved through coprecipitation routes. The idea is to start with precursors that must decompose during a heat treatment and the remaining elements can form the desired composition. Consider the combustion of lanthanum carbonate and manganese oxalate to form $LaMnO_3$

$$La_2(CO_3)_3 + 2\,MnC_2O_4 = 2\,LaMnO_3 + 5\,CO_2\,. \qquad 3.6$$

The combustion can involve solid condensed-state precursor materials (self-propagating high-temperature synthesis, SHS), liquid precursos (solution combustion synthesis, SCS) or even gas-phase synthesis. Typical starting materials for SHS are organometallic compounds (carbonates, oxalates or acetates) and decomposition occurs over a medium temperatures range. For solution combustion synthesis, however, metal salt (nitrate)

precursors mixed with urea or glycerine as a fuel source are more commonly used and decomposition occurs at a lower temperature. The precursor materials are mixed in a crucible and the entire crucible is then put in an oven and the temperature is slowly raised first to evaporate any liquid and then to combust the materials. A regrettable consequence of decomposition is the inherent gas byproducts which, for the case of nitrates in particular, can be dangerous if not performed inside a fume hood. Whether NO_2 or N_2 is formed depends on the ratio of NO_3^- to fuel; if sufficient fuel is present then N_2 will form.

Combustion synthesis was invaluable as a synthesis route for all of the experiments described in this work. In particular, for the $Fe_xMn_{1-x}Ni_{2-y}Cr_yO_4$ x=0, ¼, ½, ¾, 1 and y=0,1,2 series the solid-state and coprecipitation methods were unable to produce dense, crystalline pure phase materials but solution combustion synthesis was successful. Iron, nickel chromium and manganese nitrate solutions were mixed in a beaker in appropriate quantitites with a small amount of glycerine and combusted in a fume hood. We also employed combustion synthesis using solid precursors (lithium, manganese and magnesium oxalates) to synthesize $LiMn_2O_4$ and $Li_xMg_{1-x}Mn_2O_4$ materials.

3.1.4 Current Assisted Pressure Activated Densification

Synthesis of pure phase, crystalline compounds in powder form facilitates many structural characterization techniques such as powder diffraction or Raman microscopy. However, it is often necessary to sinter, or densify the compound into a solid body in order to measure thermoelectric properties. For example, thermal conductivity requires a

pellet shaped material (10mm diameter, 1-2mm thickness) and rectangular bars are necessary for thermopower and electrical conductivity measurements (3-10mm length, 2mm width and thickness). There are a variety of methods whereby powders can be consolidated and sintered into a dense body. The most simple and widely used approach is to use a die to compact the powders uniaxially into a green, or unfired pellet and then to sinter the pellet in air to remove the remaining porosity.

In pressureless sintering a reduction in free energy due to reducing surface area and solid-gas interfaces acts as the driving force for sintering. The driving force can be increased, however, when a pressure is applied to the compact during heating. One specific variant of this process is the so-called spark plasma sintering (SPS) technique. In fact, SPS is a misnomer as there is no spark and no plasma involved causing some to refer to the technique as current assisted densification (CADPro). The ceramic powders are compacted under a load into a die normally made of carbon though some higher strength materials such as SiC are used occasionally. The powder is heated under vacuum by applying a DC current across the plungers of the die. As the current passes through the die, or, in the case of electrically conductivity powders, through the powder compact itself there is Joule heating. Due to the large currents involved very fast heating rates up to 1000 K/min can be achieved and the applied pressure can significantly lower the temperatures required for densification. Faster heating rates paired with lower temperatures makes CADPro an ideal process to retain microstructures because grain growth is suppressed. Originally it was expected that a pulsed DC current would create a

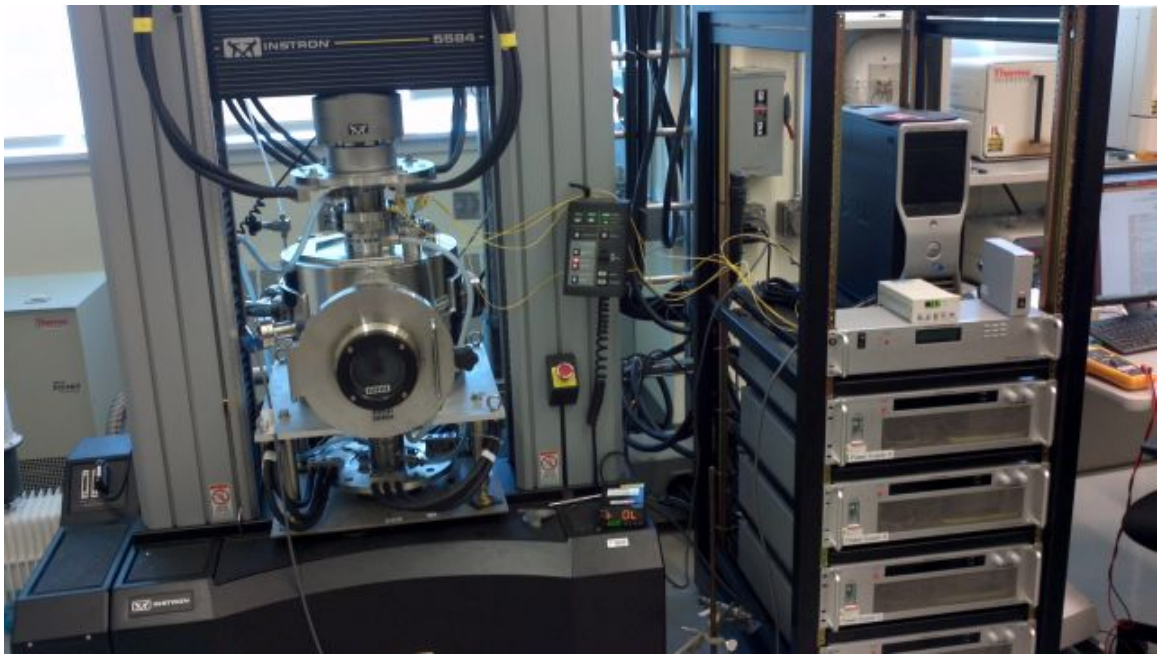

Figure 3.2. Custom built SPS or CADPro sintering chamber. The chamber is located within an Instron frame allowing a mechanical load and displacement to be applied and monitored.

strong electrical field diffusion effect but the actual role of such an effect is still debated.[157–159] For the $LiMn_2O_4$ and $Li_xMg_{1-x}Mn_2O_4$ materials we investigated pressureless sintering was unable to produce sufficiently dense samples so CADPro was employed on an instrument, developed by Andi Limarga, shown in Figure 3.2. Densities >90% were routinely achieved.

3.2 Structural Characterization

In order to explore the structure-processing-property relationships fundamental to materials science information must be obtained about the characteristic features of a material. There are many structural characterization tools ranging from macrostructural to

meso and microstructural and even probes to examine materials on the atomic scale! Brandon and Kaplan [160] point out that no single characterization technique is suitable for examining a structure at all length scales, but rather a compilation of tools applied in parallel is necessary. They argue that the techniques with the most widespread use are optical microscopy, X-ray diffraction and electron microscopy which rely on visible light, X-ray radiation and high energy electron beams respectively to probe a material. In this work we concern ourselves with the details of the crystal structure. Accordingly, we rely most heavily on diffraction using X-ray radiation and neutrons, a probe of long range order as it relates to the crystal structure. However, in a secondary role we examine short range order using Raman microscopy. Lastly, we go beyond looking at structural features to examine the response of a material to a thermal gradient and an electrical field; namely electrical and thermal conductivity and thermopower. A discussion of the structure and properties determined from these techniques will be described in the following sections.

3.2.1 X-Ray Powder Diffraction

Since the initial discovery of X-rays in 1895 and its first application to crystallography in 1912 X-ray diffraction (XRD) has grown remarkably to become an entire discipline with many techniques and capabilities. A more complete treatment of the subject is found elsewhere [161–163] Nevertheless, it is instructive to at least describe the principle underlying the technique. XRD is an elastic scattering process whereby an incident X-ray strikes a material, scatters and the diffracted beam intensity is measured as a function of incident and diffraction angle. Modern X-ray powder diffractometers use X-

rays produced by colliding a beam of electrons with a metal such as copper, molybdenum or cobalt and a portion of the energy released is given off as X-rays. The wavelength of the X-ray depends on electron transitions of inner electron shells and for this reason X-ray wavelength depends strongly on the anode metal used. The X-ray wavelength can be further monochromated until a very pure wavelength of light is obtained.

When an incident X-ray beam strikes a material with long range order, such as a crystal, there is scattering from the lattice planes (see Figure 3.3). If the incident and diffracted beams are in phase then destructive interference is avoided and a strong signal can be observed. Geometrically speaking, specular reflection from a crystal with an interplanar spacing, d, can lead to a path difference between the incident beam and the beams reflected from two parallel planes. In order for these beams to be in phase the path difference must be equal to an integer multiple of the X-ray wavelength; this is the basis of the well known Bragg's Law

$$n\lambda = 2d\sin(\theta). \qquad 3.7$$

where λ is the X-ray wavelength, θ is the incident angle and n is an integer (1,2,3…).

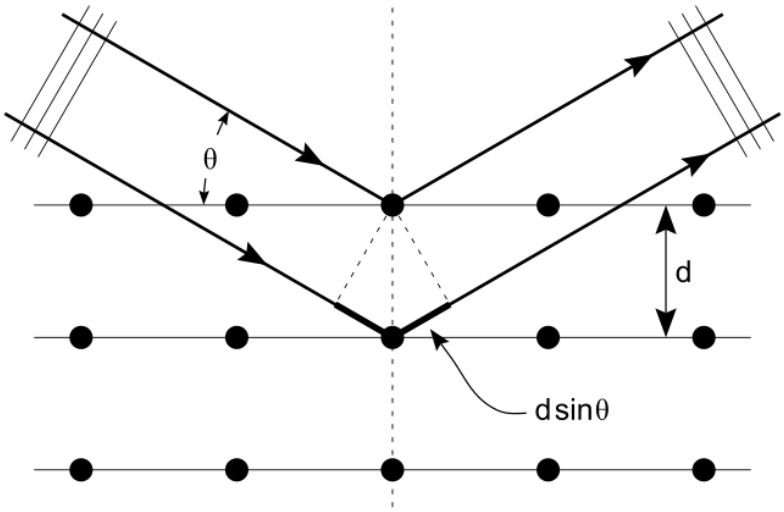

Figure 3.3. Illustration of X-ray diffraction from lattice planes in an ordered material. The diagram illustrates the relation between incident angle θ and lattice plane separation d known as Bragg's law. Figure used with permission.[164]

The crystal structure can be assessed by observing diffraction intensity as a function of angle. In a crystal there are multiple planes of atoms that can cause diffraction- these are known as Miller indices. The interplanar spacings are a function of these Miller indices, or what planes are diffracting, and the lattice parameter of the structure. Following Kaplan and Brandon, for a particular interplanar spacing corresponding to the (hkl) plane we can rewrite Equation 3.7 as

$$\lambda = 2d_{hkl}\sin(\theta). \tag{3.8}$$

where d_{hkl} is generally written for any Bragg lattice as

$$\frac{1}{d^2} = \frac{1}{V^2}\left(C_{11}h^2 + C_{22}k^2 + C_{33}l^2 + 2C_{12}hk + 2C_{23}kl + C_{31}lh\right). \tag{3.9}$$

The volume, V, of the unit cell is defined as

$$V = abc\sqrt{1-\cos^2\alpha-\cos^2\beta-\cos^2\gamma+2\cos\alpha\cos\beta\cos\gamma}\,. \qquad 3.10$$

with lattice parameters a, b and c and unit cell angles α, β and γ. The constants C_{ij} are given by

$$\begin{pmatrix} C_{11} = b^2c^2\sin^2\alpha \\ C_{22} = c^2a^2\sin^2\beta \\ C_{33} = a^2b^2\sin^2\gamma \\ C_{12} = abc^2(\cos\alpha\cos\beta-\cos\gamma) \\ C_{23} = a^2bc(\cos\beta\cos\lambda-\cos\alpha) \\ C_{31} = ab^2c(\cos\gamma\cos\alpha-\cos\beta) \end{pmatrix} \qquad 3.11$$

Substituting Equations 3.10 and 3.11 into Equation 3.9 gives the planar spacings. For example, a cubic lattice where $a = b = c$ and $\alpha = \beta = \gamma = 0$ the expression simplifies to

$$\frac{1}{d^2} = \frac{\left(h^2+k^2+l^2\right)}{a^2}. \qquad 3.12$$

The intensity of a diffracted peak, I, contains additional information about the crystal and depends on a number of factors. Intensity has the general form

$$I = k\left|F^2\right|\frac{1+\cos^2 2\alpha\cos^2 2\theta}{\sin^2\theta\cos\theta\left(1+\cos^2 2\alpha\right)}PA(\theta)\exp\left(\frac{-2B\sin^2\theta}{\lambda}\right). \qquad 3.13$$

where k is a scaling factor, $|F^2|$ is the structure factor, $\frac{1+\cos^2 2\alpha \cos^2 2\theta}{\sin^2\theta\cos\theta\left(1+\cos^2 2\alpha\right)}$ is the Lorentz polarization factor determined by sampling geometry, P is the multiplicity of the reflecting plane, $A(\theta)$ is the absorption correction and $\exp\left(\frac{-2B\sin^2\theta}{\lambda}\right)$ is a temperature factor. The complete details of these expressions are beyond the scope of this work, but it is worth noting that the structure factor, $|F^2|$, takes into account both the spatial distribution of atoms in a structure as well as the atomic scattering factor, f, which dictates the individual scattering amplitudes for an atom. For a given hkl reflection the structure factor for N atoms located at (u,v,w) in a material is given by

$$F_{hkl} = \sum_{n=1}^{N} f_n \exp\left[2\pi i\left(hu_n + kv_n + lw_n\right)\right]. \tag{3.14}$$

The atomic scattering factor has the form

$$|f|^2 = \left(f_0 \exp\left(\frac{-B\sin^2\theta}{\lambda^2}\right) + f'\right)^2 + \left(f''\right)^2 \tag{3.15}$$

where f' and f'' are anomalous dispersion factors. The atomic scattering factor is proportional to the atomic number of an element because X-rays interact primarily with the electron cloud which increases in size with atomic number. If multiple atoms with sufficiently different atomic scattering factors at a given angle θ occupy the same crystallographic site then the atomic occupancy can be determined.

X-ray diffractometers feature a number of optics to improve the resolution, purity and intensity of the signal. For example, Soller slits and curved (Göbles) mirror ensure the beam is parallel and collimated, divergence slits determine the area of sample to illuminated by the X-ray beam and filters and monochromators remove undesired impurity wavelengths such as $K_{\alpha 2}$ and K_{β}.

There are many different geometries and conditions for measuring XRD. For the most part our samples were loose powders placed on a stationary holder made of a polymer or a zero background holder (ZBH, silicon cut along a non-diffracting plane). The instrument geometry most commonly employed was Bragg-Brentano theta-theta scan where both the incident and diffracted beam angles were equal; i.e. the source and detector both moved during the scan.

A copper anode in a Phillips PANalytical X'Pert Pro diffractometers (Almelo, the Netherlands) in continuous scanning mode at 45 kV and 40 mA with vertical theta-theta geometry was used to produce Cu K_{α} radiation for $LiMn_2O_4$ and $Li_xMg_{1-x}Mn_2O_4$ materials. However, compounds containing iron or cobalt such $Fe_xMn_{1-x}Ni_{2-y}Cr_yO_4$ x=0, ¼, ½, ¾, 1 and y=0,1,2. and Co_3O_4 required the use of a cobalt anode at 40 kV and 45 mA in order to minimize absorption and fluorescence and thereby reduce a large background (see Figure 3.4). High quality scans were obtained by scanning from 20^o to 100^o with a step size of 0.017^o and a rate of 1.4 s/step. Fixed divergence and scattering slits of 0.5^o, 0.02 radian Soller slits and K_{β} filters and a germanium detector were used. The height of the sample in the furnace was zeroed by splitting the beam and the tilt was

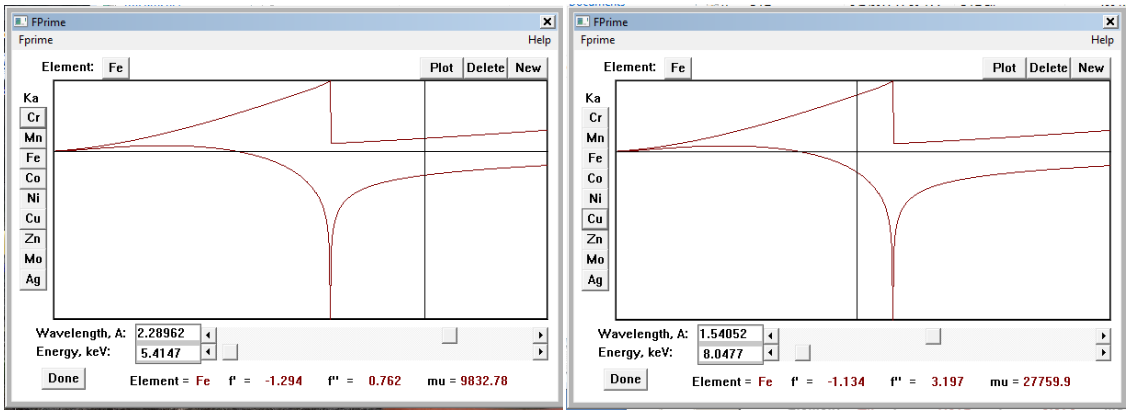

Figure 3.4. Dispersion factors, f' and f'', for the element iron using Cr K_α (left) and Cu K_α (right) radiation sources. When copper radiation is used it is strongly absorbed and fluoresced by iron. Images made using FPRIME software.[165]

corrected by rocking the sample. For high temperature data collection an Anton-Paar HTK1200N furnace was employed to heat the samples. The temperature fluctuation within the furnace was less than 1 K and the sample was heated slowly at 5 K/min and allowed 30 minutes to equilibrate before each scan was performed. Measurements were carried out in an air atmosphere with the exception of the reduced $LiMn_2O_4$ samples which were measured in argon.

The X-ray diffraction experiments reported in this work relied on both basic laboratory X-ray diffractometers as well as diffractometers using synchrotron radiation. The technique is the same except that for the intensity and wavelength of the incident radiation. Instead of relying on X-ray emissions from a metal as electrons transition between different shells a synchrotron is a particle accelerator that uses bending magnets

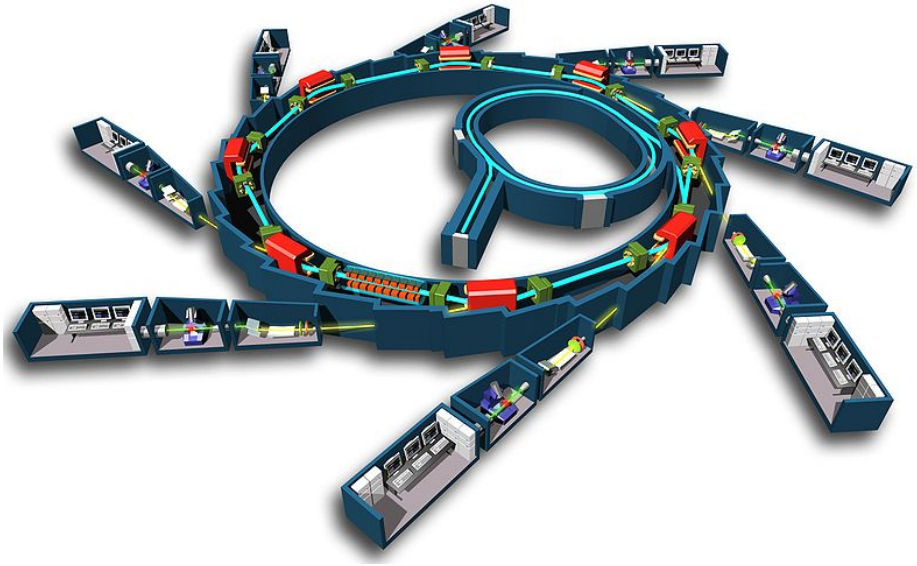

Figure 3.5. Schematic diagram of a synchrotron. The outer ring is a particle accelerator that has bending magnets (shown in red) used to change the direction of the electron (radial acceleration) and emit electromagnetic radiation directed into tangentially situated diffractometers. Image used with permission from EPSIM 3D/JF Santarelli.[166]

to radially accelerate charged particles causing them to emit electromagnetic radiation at a specific wavelength. Synchrotron radiation is far more intense than laboratory diffractometers meaning excellent signal to noise ratio for even small samples. Laboratory X-ray diffractometers were used to study all of the samples in this work, but for the samples in the $Fe_xMn_{1-x}Ni_{2-y}Cr_yO_4$ x=0, ¼, ½, ¾, 1 and y=0,1,2 series synchrotron diffraction was also used in an attempt to determine cation distribution. Powders were prepared in our lab and then sent to Argonne National Laboratory 11-BM beamline and the diffraction data was then returned for us to perform Rietveld refinement analysis.

3.2.2 Neutron Diffraction

A neutron is a particle generated in a nuclear reactor or spallation source and it interacts with a material in a fundamentally different way than electromagnetic radiation. Because of this difference neutron diffraction, first performed in 1945,[167] can extract different information from a material while using essentially the same technique as X-ray diffraction. In contrast to X-rays, which scatter primarily off the electron cloud, neutrons interact directly with the nucleus of a material. This has several implications. First, the penetration depth of neutrons in a material is much greater than X-rays and larger sample sizes are typically required. Second, since nuclei don't have nearly the size range as electron clouds the atomic number dependence of neutron diffraction is removed. The atomic scattering factor for neutrons is more random and even isotopes of the same element are typically different. Third, neutron diffraction intensity does not decrease with scattering angle as it does in XRD allowing the observation of high angle peaks and very precise atomic coordinate determination.

Perhaps the most celebrated and useful aspect of neutron diffraction is that neutrons, having spin but no charge, are sensitive to magnetic moments and are therefore capable of determining the magnetic structure of materials. When neutron diffraction is measured for a magnetic material in a cryostat above and below its magnetic ordering temperature additional peaks corresponding to diffraction from the magnetic structure are observed. The magnetic moment in an atom derives from the electron cloud however, so magnetic peaks decrease in intensity at high angle just as XRD peaks do. In our work the

magnetic moment for Co_3O_4 samples air quenched from different temperatures between 300-1173 K was measured by comparing neutron diffraction collected in a cryostat at 100 K and 1.5 K.

A neutron diffractometer and cryostat is shown in Figure 3.6. Because neutrons interact less strongly with materials the diffracted signal is much weaker than XRD. This weak signal means longer scans are necessary. One way to reduce the scan time is to use an area detector, such as the one shown in Figure 3.6, to measure over a large diffraction range at the same time. Area detectors can also often measure outside the plane of diffraction increasing the signal intensity but with a slight reduction in resolution. An example of this is shown in Figure 3.7 where the Laue cone is visible at low and high angles and the tradeoff between intensity and resolution is shown.

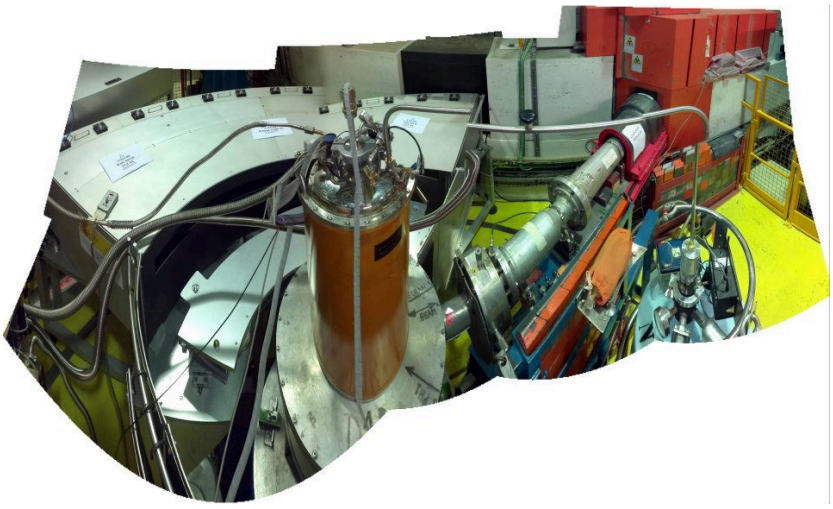

Figure 3.6. Photograph of a neutron diffractometer with a cryostat (D1B at Institut Laue Langevin).

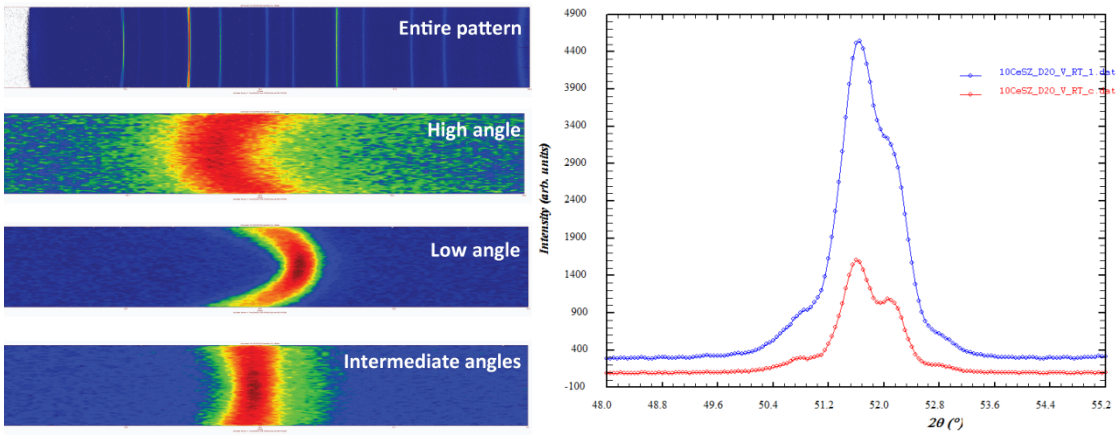

Figure 3.7. Neutron diffractometer area detector results, (left) the entire pattern, high, low and intermediate angles are shown for a measurement, (right) whole detector (blue) and center region only (red) demonstrating tradeoff between resolution and intensity.

3.2.3 Rietveld Refinement

The majority of XRD users rely on the technique for phase identification of a material only. A sample is measured and the 2θ position and intensity of the observed peaks are identified and then a search and match software such as Phillips X'Pert Highscore, MDI "Jade", or DIFFRACplus is used to match the phase or phases present to known patterns corresponding to compounds in a database. If the composition of the sample is unknown and no chemical restrictions can be applied to the database then it can be extremely difficult to correctly identify the phase using only a stick diagram (position and intensity). Furthermore, if multiple phases or uncrystallized amorphous content are present it is much more difficult to accurately determine the phases present and impossible to ascertain the phase fractions. An example of this can be seen in Figure 3.8

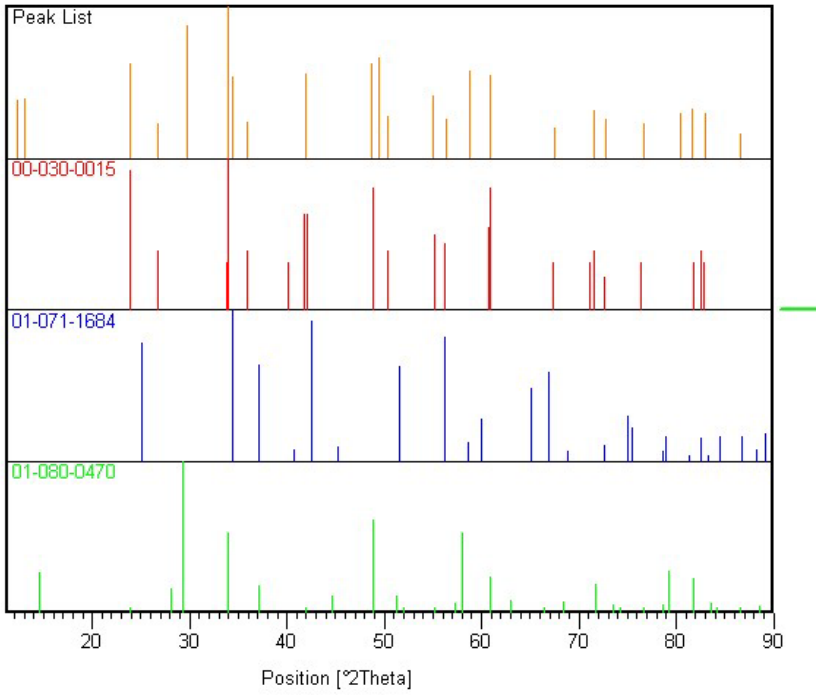

Figure 3.8. Example of a stick diagram to match measured peaks (top pattern) to candidate structures on file (bottom three patterns).

The Rietveld refinement technique described in this section and originally formulated by Hugo Rietveld [168] in 1969 can not only verify that phase identification was done correctly but also uncovers an enormous amount of additional information that X-ray diffraction can tell a user about a material. The Rietveld method can be applied to accurately determine lattice parameters, atomic positions, occupancy of atoms per site, atomic displacement parameters (ADPs), phase fraction including amorphous material content, preferred orientation, grain size and strain. Additionally the method can account for sample and instrument errors such as displacement or shift, transparency, zero of the goniometer and impurity wavelengths. The reason that Rietveld refinement can extract so much additional information is because it relies on whole profile fitting, rather than

simply search and match based on a stick diagram. Just as there are many search and match software packages available, there are many Rietveld refinement software packages available but the most widely used are GSAS (General Structural Analysis Software) [169,170] and Fullprof.[171]

The Rietveld refinement method fits a background to the collected diffractogram data, calculates all the reflected planes, assigns each peak an intensity based on Equation 3.13 and a shape and then refines attributes of the crystal structure or sample/instrument corrections using a least squares algorithm until the observed diffractogram best matches a calculated diffractogram. The least squares algorithm minimizes the following function

$$M = \sum_i W_i \left(I_i^{obs} - \frac{1}{c} I_i^{calc} \right)^2 \qquad 3.16$$

where W_i is a weighting factor (higher intensity values, such as peaks are weighted more heavily than background values), I_i is the intensity value at each point i. The variable c is a scaling factor such that $I_i^{obs} = cI_i^{calc}$. The quality of the fit is given by the weighted residual

$$R_{wp} = \sqrt{\frac{M}{\sum_i W_i \left(I_i^{obs} \right)^2}} \,. \qquad 3.17$$

For a given Bragg lattice we can calculate which (hkl) planes will have reflections. To do so we solve for all h, k and l values such that Equation 3.14 has a non-

zero result for atoms located at (u, v, w). Peak shapes can be Gaussian in nature as neutron diffraction peaks are, or they can have a significant Lorentzian component. The correct profile function, or peak shape, is the one that best fits the data. If the instrument beam has a large amount of vertical divergence, then asymmetric peaks will be observed, particularly at low diffraction angles. Fortunately, asymmetry can also be refined.

Quantitative phase analysis is one of the more useful outcomes of analyzing powder diffraction data. Estimating the phase abundance in a multi-phase material is challenging. The phase abundance can be determined by indirect methods such as the Bogue method [172] where the total chemical composition is determined and assuming a chemical composition for each phase an estimation can be made. Phase fraction can also be measured by direct methods relying on some property specific to each phase such as magnetism, selective dissolution, density, image analysis and thermal analysis. Quantitative phase analysis using powder diffraction is another such direct method. Phase fraction is determined by "single peak" methods such as Reference Intensity Ratio (RIR) [173] or by whole pattern methods such as the SMZ method.[174,175] More accurate and precise results are obtained by the SMZ method because overlapping peaks are accounted for. In Rietveld refinement the intensity of a reflection (or group of reflections), i, can be reduced to

$$I_{i\alpha} = C_{i\alpha} \frac{W_\alpha}{\rho_{D,\alpha} \mu_m^*} \qquad 3.18$$

where $C_{i\alpha}$ is a constant for reflection(s), i, in phase α, W_α is the weight fraction, $\rho_{D,\alpha}$ is the density and μ_m^* is the mass absorption coefficient. The intensity is proportional to the Rietveld scale factor, S_α

$$I_{i\alpha} \propto S_\alpha \tag{3.19}$$

and the constant $C_{i\alpha}$ is inversely proportional to the square of the unit cell volume

$$C_{i\alpha} \propto \frac{1}{(V_\alpha)^2}. \tag{3.20}$$

The density $\rho_{D,\alpha}$ is given by

$$\rho_{D,\alpha} = \frac{ZM_\alpha}{V_\alpha} \tag{3.21}$$

where Z is the number of formula units in the unit cell and M is the molecular mass of the formula unit. Substituting Equations 3.19-3.21 back into Equation 3.18 and solving for W_α we obtain

$$W_\alpha = \frac{S_\alpha (ZMV)_\alpha \mu_m^*}{K} \tag{3.22}$$

where K is a scaling factor necessary to put W_α on an absolute basis. For multiple phases, the relative weight fraction of n phases would be

$$W_\alpha = \frac{S_\alpha (ZMV)_\alpha}{\sum_{k=1}^{n} S_k (ZMV)_k}. \quad 3.23$$

Addition of a known amount of a standard allows the determination of absolute weight fraction of each phase as well as quantitative determination of unknown or amorphous phases.

3.2.4 Raman Microspectroscopy

A final structural characterization technique that we will cover is Raman Microscopy. Unlike diffraction, Raman scattering of a light source with a material relies on an inelastic process. Another contrast is the wavelength of light used. XRD of single crystals can use white light, but as described in the previous section, powder XRD relies on monochromated X-rays whereas Raman spectroscopy uses laser light in the visible, near ultraviolet or near infrared range as an excitation source. As with diffraction, a more exhaustive summary of the technique is described elsewhere.[176–178] Let us begin this section with a brief overview of the different ways light can interact with matter via scattering.

Light interacts with the electron cloud and bonds in a material. The majority of light that is absorbed will cause a molecule to be elevated to a virtual energy level and when the molecule returns to this state light is reemitted with the same energy. This type of scattering is an elastic process because there is no change in energy and is known as Rayleigh scattering. In some cases, however, there is an exchange of energy between the

light and the material (see Figure 3.9). If energy is absorbed by the material, as in Stokes scattering, then the emitted light must have less energy than the absorbed light (red shifted). Alternately, if energy is lost by the material, as in anti-Stokes scattering, then the emitted light is more energetic than the absorbed light (blue shifted). Typically, the Raman shift in energy, ΔE, is on the order of 200-4000 cm^{-1}, the conventional unit of measurement, and can be expressed as

$$\Delta E = \left(\frac{1}{\lambda_{absorbed}} - \frac{1}{\lambda_{emitted}} \right). \qquad 3.24$$

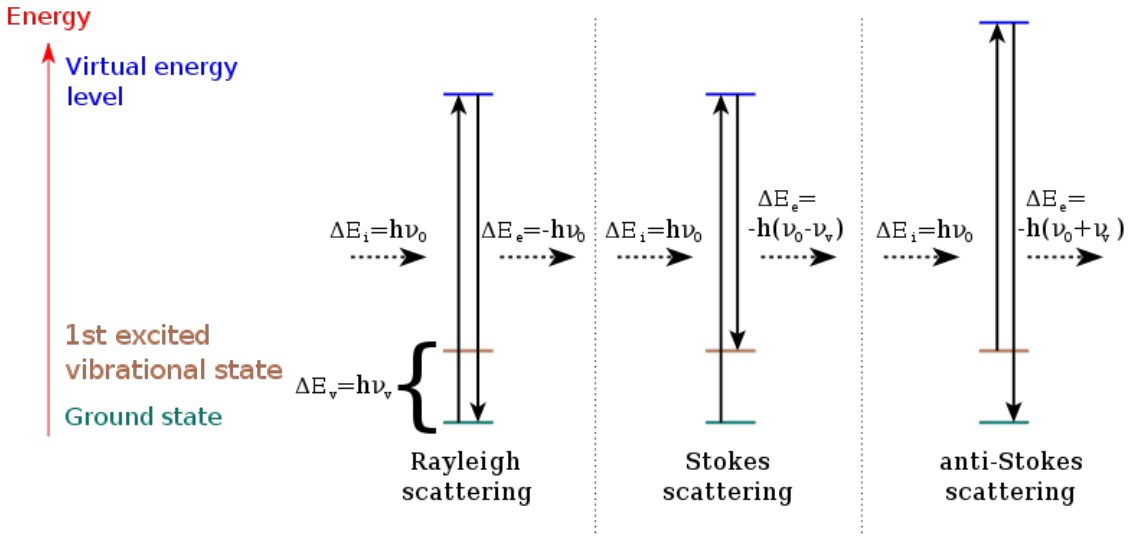

Figure 3.9. Rayleigh and Raman (Stokes and anti-Stokes) scattering. Rayleigh is eleastic light scattering while Raman scattering is inelastic with a shift in energy between absorbed and emitted light. Image used with permission.[179]

As can be seen in Figure 3.9, some molecules in a material will be in the ground state to start with (Rayleigh and Stokes scattering) and some molecules will be in an excited vibrational state (anti-Stokes scattering). For a given energy difference between the excited vibrational state and the ground state, ΔE_v, we can rely on a Boltzmann distribution to determine the number of molecules in the excited and ground states $N_{excited}$ and N_{ground}:

$$\frac{N_{excited}}{N_{ground}} = \frac{g_{orbital,excited}}{g_{orbital,ground}} \exp\left(-\frac{\Delta E_v}{k_B T}\right) \tag{3.25}$$

where $g_{orbital,excited}$ and $g_{orbittal,ground}$ are the orbital degeneracies of the excited and ground state bands. The implication of Equation 3.25 is that there is always a greater number of molecules in the ground state than in the excited vibrational state. Therefore, since scattering is related to the number of initial molecules in a state the intensity of Stokes scattering spectra is always greater than anti-Stokes scattering spectra.

Materials have unique bonding and symmetry so the Raman scattering from the vibrational modes are material specific and can be used to characterize materials. As demonstrated in Sections 3.2.1-3.2.3, the crystal and microstructural relationship to diffraction techniques is very well understood insomuch that calculated patterns can even be fitted to observed patterns with very good agreement. Vast databases of indexed patterns exist for a hundreds of thousands of inorganic and organic compounds including measurements done at non-ambient temperatures and pressures. On the other hand,

Raman spectroscopic characterization of materials is not yet as developed. Despite efforts, such as the RRUFF project,[180] to develop Raman spectra databases similar to those available for diffraction data the majority of Raman spectroscopy users rely on the technique to compare samples of different compositions, heat treatments etc. relative to one another.

Despite its shortcomings, Raman spectroscopy still features many advantages, especially when paired with optical microscopy. Raman microspectroscopy features good resolution (<1 μm), very fast data collection and little or no sample preparation. In addition, Raman scattering is also a probe of a material on a fundamentally different length scale than diffraction. Vibrational modes observed by Raman spectroscopy are more indicative of short range order in a crystal than long range.

In our experiments we relied on *in-situ* Raman microspectroscopy using a confocal LabRAM ARAMIS Raman Microscope (HORIBA Scientific) using 515 nm laser beam (Kimmon Electric US, Ltd. IK Series He-Cd LASER Englewood, USA) to observe a high temperature structural anomaly in spinel Co_3O_4. Spectra at elevated temperatures in air were obtained using a Linkam thermal stage (Scientific Instruments Ltd., Waterford Surrey, England). Spectra were taken from room temperature (298 K) up to a temperature of 1223 K and vice versa during the heating and cooling ramp (10 K/min), respectively. Spectral treatment, such as baseline adjustment, smoothing and normalization, was performed using GRAMS software package (Galactic Industries Corporation Salem, USA).

3.3 Electrical and Thermal Transport

Following the synthesis of materials and their subsequent structural characterization the final experimental step is measurement of properties. As described in Chapter 1, for thermoelectric materials, the relevant properties are thermopower, electrical and thermal conductivity. Although the emphasis of this work is to highlight the relationships between crystal structure and thermopower specifically, measurements of electrical and thermal conductivity add a degree of context and insight. We discuss the experimental methods for these measurements now.

Electrical conductivity and thermopower are normally measured simultaneously as a function of temperature for thermoelectrics. The diagram for measurement is shown in Figure 3.10. A bar-shaped sample with dimensions (8-20)×2×2 mm^3 is machined to have coplanar faces and placed between the top and bottom electrodes of the measurement system. Thermocouple probes are carefully set into contact with the face of the sample and the distance d_1 is measured via camera calibrated to the sample width. The entire fixture is enclosed in a furnace and for samples vulnerable to oxidation the chamber can be evacuated and backfilled with an inert gas, such as helium. The furnace is brought to temperature and allowed to equilibrate.

Thermopower is measured by heating the bottom electrode with an embedded wire mesh. A temperature difference, ΔT, of normally 5, 10, or 20 K is established across the sample and the potential difference, $(V_2 - V_1)$, is measured for a temperature

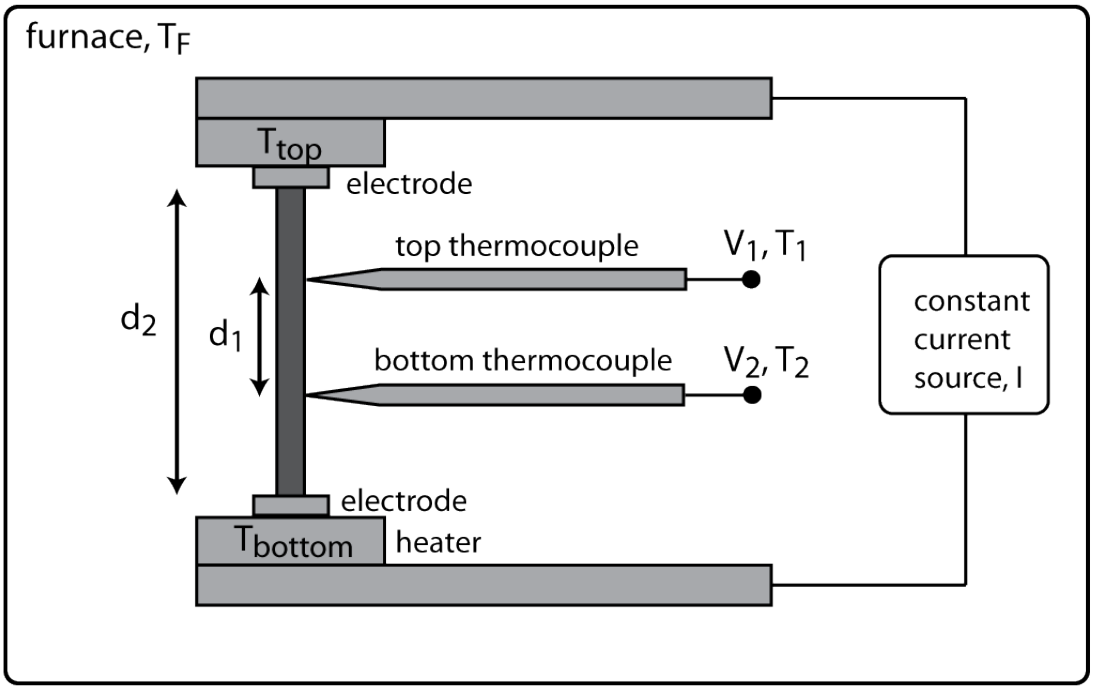

Figure 3.10. Thermopower and electrical conductivity measurement schematic. Operation described in text.

difference, $(T_2 - T_1)$. The ratio of these two measurements is the thermopower (Equation 1.8). The same fixture can be used to measure electrical conductivity. If a constant current source, I, is directed through the sample and the voltage drop is measured across the thermocouples then we can measure the resistance of the sample between the thermocouples using Ohm's law

$$V = V_2 - V_1 = IR \qquad 3.26$$

where R, the sample resistance, is given by

$$R = \frac{\rho L}{A} = \frac{\rho d_1}{A} \qquad 3.27$$

recalling that ρ is the resistivity, d_1 is the distance between thermocouple probes and A is the cross-sectional area. Electrical conductivity is, of course, the inverse of electrical resistivity.

Thermal conductivity is a much more difficult property to measure accurately. Steady-state heat flux methods such as comparative method,[181] guarded heat flow method,[182] hot wire method [183] or hot strip method [184] can be used to determine thermal conductivity directly based on the following heat flux expression

$$\frac{\Delta Q}{\Delta t\, A} = -\kappa \frac{\Delta T}{\Delta x}\,. \qquad 3.28$$

Devices using these methods are the thermal analog to the electrical conductivity measurement technique just described. These direct measurement techniques have infamously large uncertainty (>20%) in values though because accurately measuring the temperature gradient and heat flow rate is difficult. Especially challenging is how to account for radiative losses at elevated temperatures. An approach used much more frequently is to measure the thermal diffusivity, α, which is related to the thermal conductivity by the standard relation

$$\kappa = \alpha \rho_D C_p \qquad 3.29$$

where C_p is the heat capacity at constant pressure and ρ_D is the sample density. Specific heat can be easily measured but for our experiments we used the Kopp-Neumann law given by

$$C = \sum_{i=1}^{N} C_i W_i \tag{3.30}$$

where C is the total specific heat, C_i and W_i is the specific heat and weight fraction of the i-th component of an alloy containing N components. Calculating the specific heat from tabulated values [185] has been shown to be accurate to within 5%. [40]

Thermal diffusivity is measured by the laser flash method.[186,181] A pellet shaped sample is heated by a laser pulse on one side and the temperature is measured by an infrared sensor on the back side of the pellet. The infrared sensor voltage is proportional to the temperature and is plotted as a function of time. Because the sample is machined coplanar with diameter much larger than thickness (typically 10mm diameter, 1 mm thickness) approximately adiabatic boundary conditions exist and the heat flow is roughly one-dimensional. Following Thambynyagam's derivation[187] the one-dimensional thermal diffusion equation is

$$\frac{\partial T(x,t)}{\partial t} = -\alpha(T)\frac{\partial^2 T(x,t)}{\partial t^2}. \tag{3.31}$$

The general solution is of the form

$$T(x,t) = \exp(-ct)\cdot\left[A\sin\sqrt{\frac{c}{a}}x + B\cos\sqrt{\frac{c}{a}}x\right] \tag{3.32}$$

and assuming adiabatic boundary conditions for a coplanar sample with no heat flux at the surfaces this expression can be written as the series

$$T(x,t) = \sum_{n=0}^{\infty} B_n \cos\left(\frac{n\pi x}{L}\right)\exp\left(-\frac{n^2\pi^2 at}{L^2}\right). \tag{3.33}$$

For a finite pulse of very short duration the change in heat measured at the back face is

$$\Delta T(x = L,t) = \Delta T_{\infty}\left[1 + 2\sum_{n=1}^{\infty}(-1)^n \exp\left(-\frac{n^2\pi^2 at}{L^2}\right)\right]. \tag{3.34}$$

where ΔT_{∞} is the change in temperature at the back face after infinite time. Thus expression can be rearranged to solve for diffusivity with the following approximation

$$\alpha \cong -\frac{\ln(1/4)}{\pi^2}\frac{L^2(T)}{t_{1/2}(T)}. \tag{3.35}$$

where $t_{1/2}$ is an important parameter defined as the time required for the temperature to increase halfway from the equilibrium temperature to ΔT_{∞}. A number of models can be applied to calculate $t_{1/2}$ from the temperature time profile such as Clark and Taylor [188] or Cape and Lehman.[189]

To minimize radiative transport through the sample it is common practice to coat both faces with a thin metallic layer (~1μm of gold) using an Effacoater sputtering system (Ernst F. Fullman Inc, Clifton Park, NY). An additional coating of colloidal graphite is applied to ensure good absorption and emissivity. The density of the samples was calculated by the Archimedes method with deionized water as an immersion medium. A final correction to thermal conductivity was applied for compounds retaining some residual porosity using the Maxwell equation [190]

$$\kappa = \kappa_0 \frac{1-P}{1+\psi P}. \qquad 3.36$$

where κ is the thermal conductivity of the sample porosity, κ_0 is the thermal conductivity of the nonporous material, P is the porosity and ψ is a geometrical factor equal to ½ for closed spherical shaped porosity.

Chapter 4. Effect of Structural Distortion and Anti-site Disorder in Spinels

The previous chapters laid out much of the necessary groundwork for understanding the experiments I performed. As we described the fundamentals of thermoelectricity, thermopower, oxide synthesis, phase characterization and property measurement a recurring theme was that the crystal structure, materials processing, characterization and properties are inseparably related. Thermal conductivity is reduced through anti-site disorder, rattling ions and nano-engineered structures. Carrier concentration has a dramatic effect on electrical conductivity. The intensity, shape and position of diffracted X-ray reflections provide information regarding elemental composition, crystal structure, texturing, thermal displacement, grain size and more. The study of these relationships and many others is the fundamental basis of materials science as a discipline.

In this chapter we are now able to look in detail at experiments designed specifically to probe the role of crystal structure on thermopower in oxide thermoelectrics. Essentially, we are looking most closely at how changes in composition, structure and disorder will alter the electronic degeneracy ratio and carrier concentration parameters in the Heikes formula for strongly correlated systems. The effect of Jahn-

Teller structural distortions will be examined in manganate oxides including spinel $LiMn_2O_4$ and the effect of anti-site disorder will be examined in $Li_xMg_{1-x}Mn_2O_4$ spinels and the $Fe_xMn_{1-x}Ni_{2-y}Cr_yO_4$ x=0, ¼, ½, ¾, 1 and y=0,1,2 series of spinels.

4.1 Structural Distortions and Thermopower

4.1.1 Common Structural Distortions in Oxides

Structural distortions are quite common in oxides. Take perovskites, one of the most common oxides, for example. Perovskites have the nominal structure ABO_3 and the ideal structure is cubic ($Pm\bar{3}m$) with A site cations surrounded by 12 anions occupying the cube corners, B site cations surrounded by 6 anions located at the cube center and oxygen atoms centered on the cube faces. Modeling the ions as space filling hard spheres with radii r_A, r_B and r_O the ideal structure requires geometrically that the A-O distance (cube corner to center of cube face, $\sqrt{2}a/2 = r_A + r_O$) to be equal to the B-O distance (center of cube face to center of cube, $a/2 = r_B + r_O$). The tolerance factor describes the deviation from the ideal structure by comparing these distances and is given by the following expression

$$t^* = \frac{r_A + r_O}{\sqrt{2}(r_B + r_O)}. \qquad 4.1$$

For the ideal perovskite structure $t^* = 1$ and this tolerance factor can be used to predict crystal structure of ABO_3 compounds.[191] For tolerance factor values near 1, i.e. $0.9 < t^* < 1$, a cubic structure is formed. For larger values $1 < t^* < 1.13$ a hexagonal

symmetry is favored and for smaller values $0.75 < t^* < 0.9$ orthorhombic Pnma crystal structures will form. Finally, values $t^* < 0.75$ will result in hexagonal ilmenite type structures.

These changes in symmetry can be accomplished through relatively small distortions in the crystal structure. This can be seen in compounds with smaller r_A and larger r_B values leading to tilting of the BO_6 octahedra in order to fill space. For orthorhombic structures the tilting is about the b and c axes and for rhombohedral structures the tilting is about each axis. This tilting leads to a reduction in coordination number for A, B or both ions (see Figure 4.1). In addition to tilting, cations can also be displaced to distort the structure.

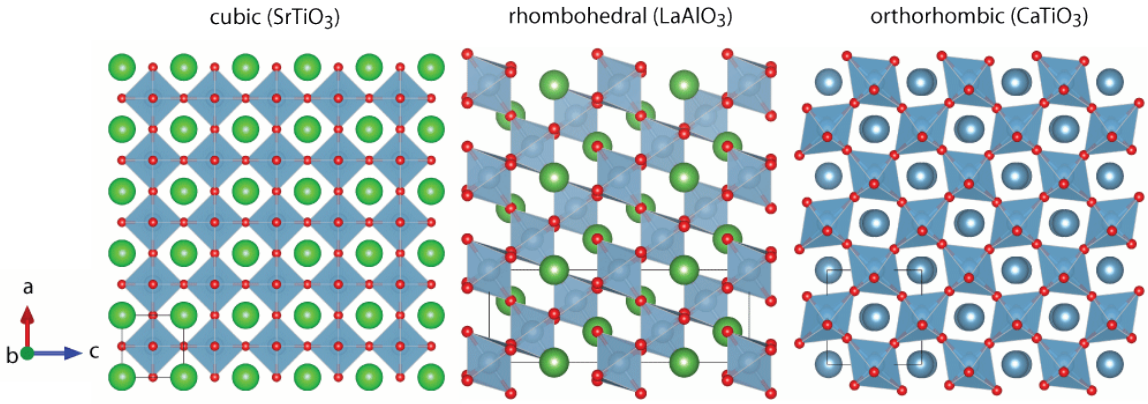

Figure 4.1. Examples of ideal and distorted perovskite structures. (left) cubic $SrTiO_3$, (center) rhombohedral $LaAlO_3$ and (right) orthorhombic $CaTiO_3$. Structures all shown projected along the b-axis to demonstrate octahedral tilting. Unit cell outline in black.

Another common structural distortion in oxides is a Jahn-Teller distortion. For a number of electronic configurations, most strongly in HS d^4 and d^9 and LS d^7 and d^9 in an octahedral coordination, the overall energy of a system can be lowered by removing the orbital degeneracy of the bands.[192] Figure 4.2 shows this energy lowering for Jahn-Teller distortions featuring octahedral HS d^4 cations. The lifting of the e_g orbital degeneracy is accomplished through the contraction of some bonds to ligands and simultaneous elongation of others. Elongation of bonds leads to greater overlap of electron clouds between cation and bonded oxygen anion and therefore higher energy of the orbital. By convention the axis of elongation is labeled z-axis. The spatial displacement of ions caused by the Jahn-Teller distortion reduces the symmetry of an ideal cubic perovskites to a tetragonal crystal structure. Jahn-Teller distortions in tetragonal/cubic/dodecahedral coordinations are less common because the CFSE for these coordinations is smaller and therefore the energy stabilization benefit of lifting orbital degeneracy is reduced.

4.1.2 The Spinel Crystal Structure

The spinel structure differs from the perovskite structure but it, too, can exhibit symmetry lowering structural distortions such as tilting, cation displacement and Jahn-Teller distortions. Spinels have the nominal formula unit AB_2O_4 where the A site, 8(a), -43m, is tetrahedrally coordinated and the B site, 16(d), .$\bar{3}$m, is octahedrally coordinated.

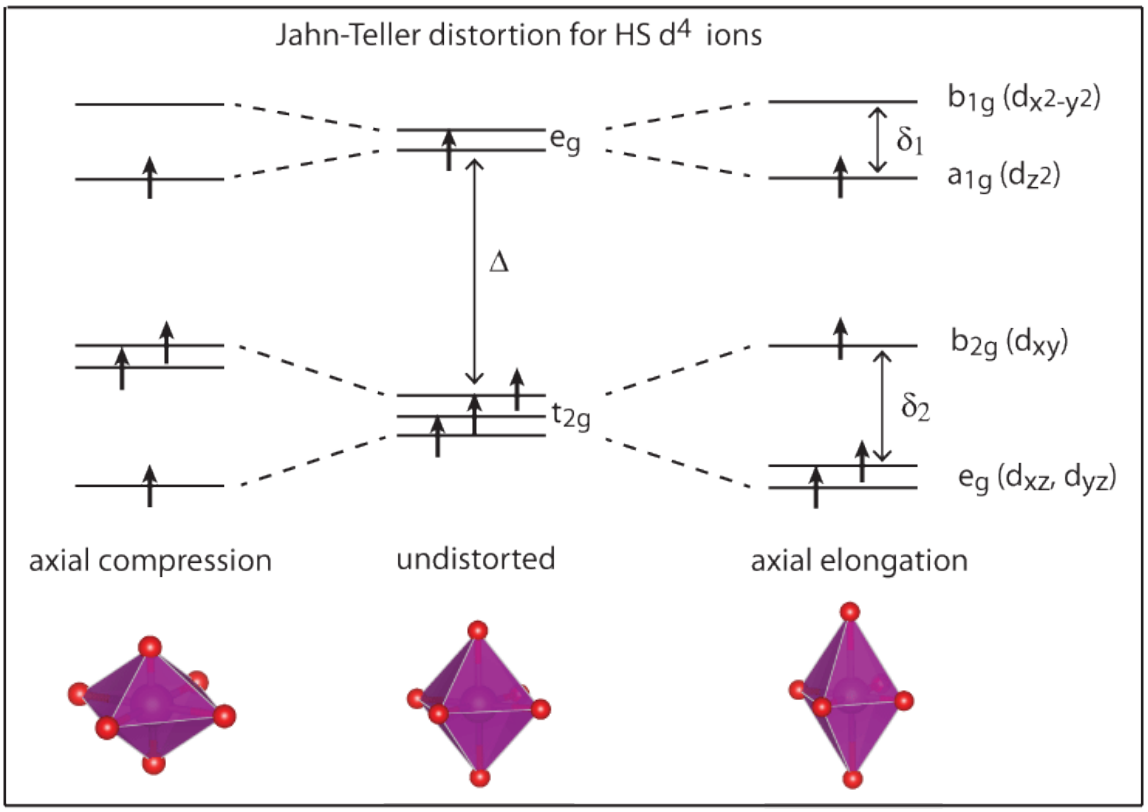

Figure 4.2. Jahn-Teller distortion examples for d^4 cations under axial compression and elongation along the z-axis.

The anion sublattice is a close-packed cubic structure and cations partially fill the octahedral and tetrahedral interstices. In terms of polyhedra, the structure contains perpendicular layers of crisscrossed edge-shared BO_6 polyhedra interconnected through AO_4 tetrahedra. The undistorted cubic ($Fd\bar{3}m$) and Jahn-Teller distorted tetragonal ($I4_1/amd$) spinel structures are shown in Figure 4.3.

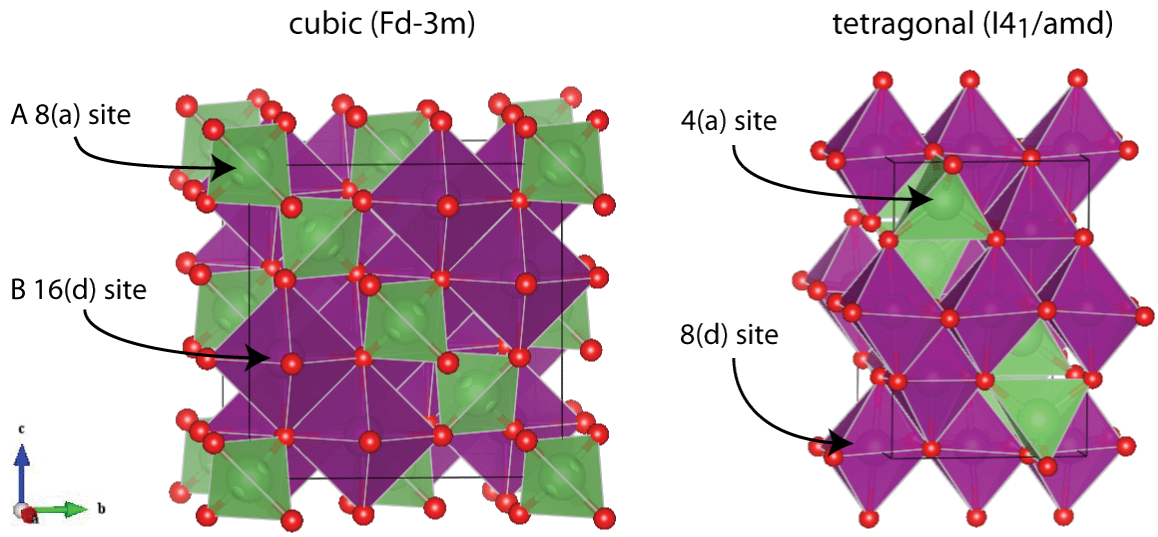

Figure 4.3. Undistorted (left) and distorted (right) $LiMn_2O_4$ crystal structures with A and B cation sites labeled. Green, purple and red atoms correspond to lithium, manganese and oxygen respectively.

Before going on, it is necessary to define inversion, a term used frequently with spinels. A large number of compounds crystallize in the spinel structure. There are 2,3 spinels where the cations have +2 or +3 oxidation states; examples include $MgAl_2O_4$, $CuFe_2O_4$, Fe_3O_4, Mn_3O_4, Co_3O_4 and many others. There are also 4,2 spinels where cations have +4 and +2 oxidation states; examples include $TiMg_2O_4$ and $SiMg_2O_4$. The distribution of the different cations is tied intimately to materials properties. A normal spinel has the A site completely occupied by cations of lower oxidation state as in Co_3O_4. Alternately, an inverse, or inverted spinel has no cations of lower oxidation state on the A site as in Fe_3O_4. Gorshkov et al. observe that synthetical spinels synthesized at high temperatures are frequently inverted but naturally occurring spinels are normal.[193] The nomenclature “partial inversion” or “disordered spinel” describes a situation with anti-

site disorder where the lower oxidation state cations partially occupy both A and B sites as in $(Fe^{2+}_{1-x}Fe^{3+}_{x})^{A}[Fe^{2+}_{x}Fe^{3+}_{2-x}]^{B}O_4$. Throughout the remainder of this dissertation the terms “A site” and “tetrahedral site” or the subscript T are all used interchangeably to denote the 8(a) cation site in $Fd\bar{3}m$ space group. Similarly, the terms “B site” and “octahedral site” or the subscript O denote the 16(d) cation site.

Distortions in crystals are strongly related to many properties including electrical conductivity, thermal conductivity, dielectric constant and colossal magnetoresistance. Too small ions can rattle on a site to scatter phonons. Cations shifted off site will also mean a charge is displaced and a dipole will result. We now discuss how a Jahn-Teller distortion affects thermopower in manganate oxides.

4.1.3 Thermopower and Jahn-Teller Distorted Manganates

In Section 2.4 we described how the modified Heikes formula can be used as a screening tool for identifying new oxide thermoelectric materials. The search for n-type materials in particular led researchers to consider strongly correlated compounds with Mn^{3+}/Mn^{4+} ion combinations.[136] Assuming the ions take a HS undistorted state the electronic degeneracy ratio in Equation 2.30 is 10/4 and with equal concentrations of Mn^{3+}/Mn^{4+} ions the thermopower is given by

$$S = -\frac{k_B}{q}\ln\left(\frac{10}{4}\frac{0.5}{1-0.5}\right) = -79\mu V/K\,. \qquad 4.2$$

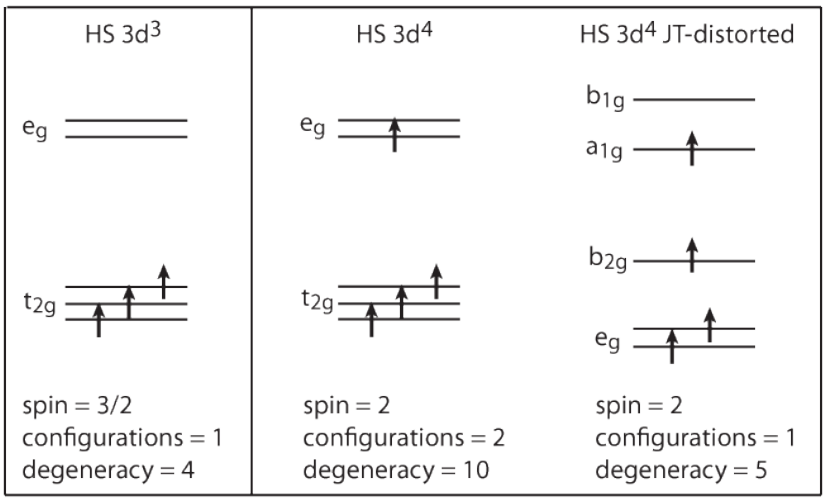

Figure 4.4. Spin and orbital degeneracy values for d^3 and d^4 cations. Jahn-Teller distortions in Mn^{3+} ions reduce the orbital degeneracy by a factor of 2.

If, however, the Mn^{3+} ions are stabilized by a Jahn-Teller distortion then the electronic degeneracy is reduced to 5/4 (see Figure 4.4) and the thermopower is reduced to

$$S = -\frac{k_B}{q}\ln\left(\frac{5}{4}\frac{0.5}{1-0.5}\right) = -19\mu V/K\,. \qquad 4.3$$

Koshibae et al. [113,114] predicted that due to the strong likelihood of Mn^{3+} forming Jahn-Teller distortions a small n-type thermopower of -19 μV/K is expected in compounds containing Mn^{3+}/Mn^{4+} ions. Experiments performed by Kobayashi et al. and Massarotti et al. seem to confirm this.[136,194] The thermopower for the mixed ion (Mn^{3+}/Mn^{4+}) manganates $CaMn_{3-x}Cu_xMn_4O_{12}$ x=0, ¼, ½, ¾, 1, $Pr_{0.5}Ca_{0.5}MnO_3$ and $LiMn_2O_4$ were measured up to 1000 K (see Figure 4.5). Despite the different composition and crystal structures of these compounds (double-perovskite, perovskites, spinel, respectively) each tended to approach the high temperature thermopower limit of -25

μV/K in close agreement with the Jahn-Teller distorted limit for thermopower. Notably, though none of the compounds reached the undistorted limit (-79 μV/K), at very high temperatures (> 950 K) the thermopower of the compounds increased to -32 μV/K and seemed to approach the undistorted limit perhaps indicating that enough thermal energy was available to recover the e_g orbital degeneracy by overcoming the Jahn-Teller distortion.

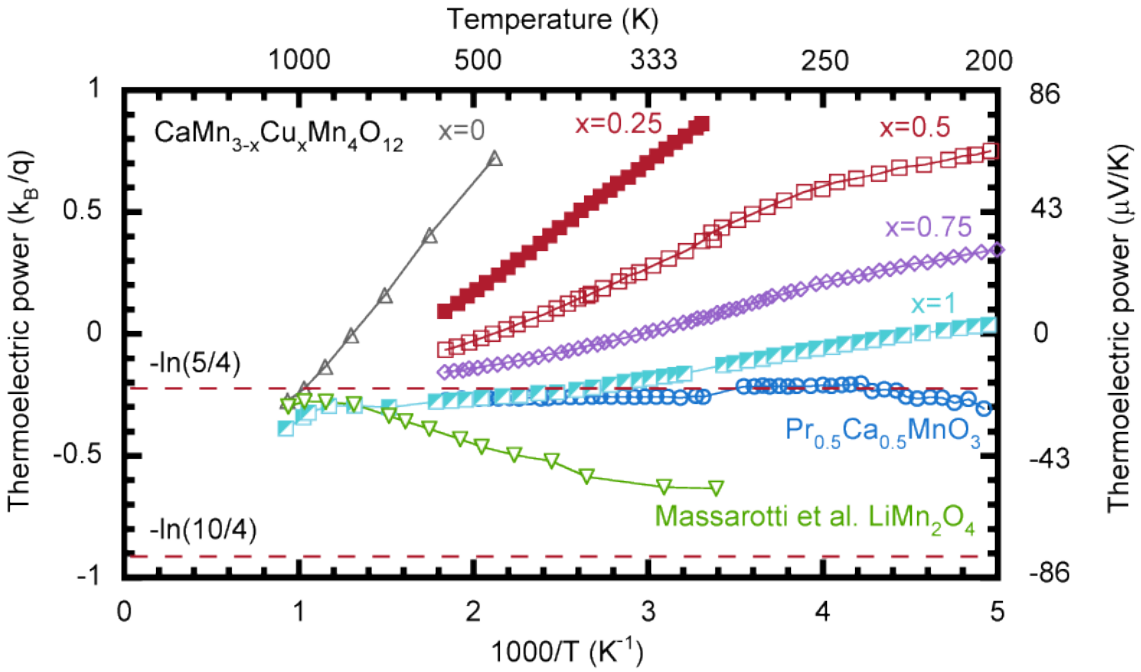

Figure 4.5. Thermopower for a variety of mixed ion manganates. The high temperature theoretical thermopower limit is shown for Jahn-Teller distorted compounds, -ln(5/4), and undistorted compounds, -ln(10/4). The compounds agree with the distorted limit until very high temperatures when the orbital degeneracy recovers. Redrawn from Kobayashi et al.[136]

Further examination of the thermopower results reported by Massarotti et al. led us to detect an inconsistency; $LiMn_2O_4$ is a spinel and previous studies [195] demonstrate clearly that a Jahn-Teller distorted tetragonal phase is only observed below 280 K, yet the high temperature thermopower in Figure 4.5 corresponds to the distorted limit. This apparent discrepancy motivated us to re-examine this compound and clarify the role of Jahn-Teller distortions, using high temperature X-ray diffraction, between the crystal structure of $LiMn_2O_4$ and thermopower measurements.

4.2 Enhanced Thermopower in Jahn-Teller distortion free $LiMn_2O_4$

Powders of $LiMn_2O_4$ were prepared by combustion synthesis and dense samples were characterized by high temperature X-ray diffraction to ensure a cubic (undistorted) structure at high temperatures.

Phase composition and structural refinement.

The results of the in-situ heating X-ray diffraction confirmed that in the air-sintered samples the major phase is an undistorted, cubic spinel-type $LiMn_2O_4$ ($Fd\bar{3}m$, a=8.2514 Å, Z=8). At room temperature, there was only 1.5 wt% of the tetragonal phase ($I4_1/amd$, a=5.82 Å, c=8.315 Å, Z=4) and no appreciable amount at elevated temperatures (Table 4.4, Figure 4.6). The finding of a cubic spinel complements the work of Yamada et al. who showed that full transition to the tetragonal phase ($I4_1/amd$) only occurs below 280 K.[195]

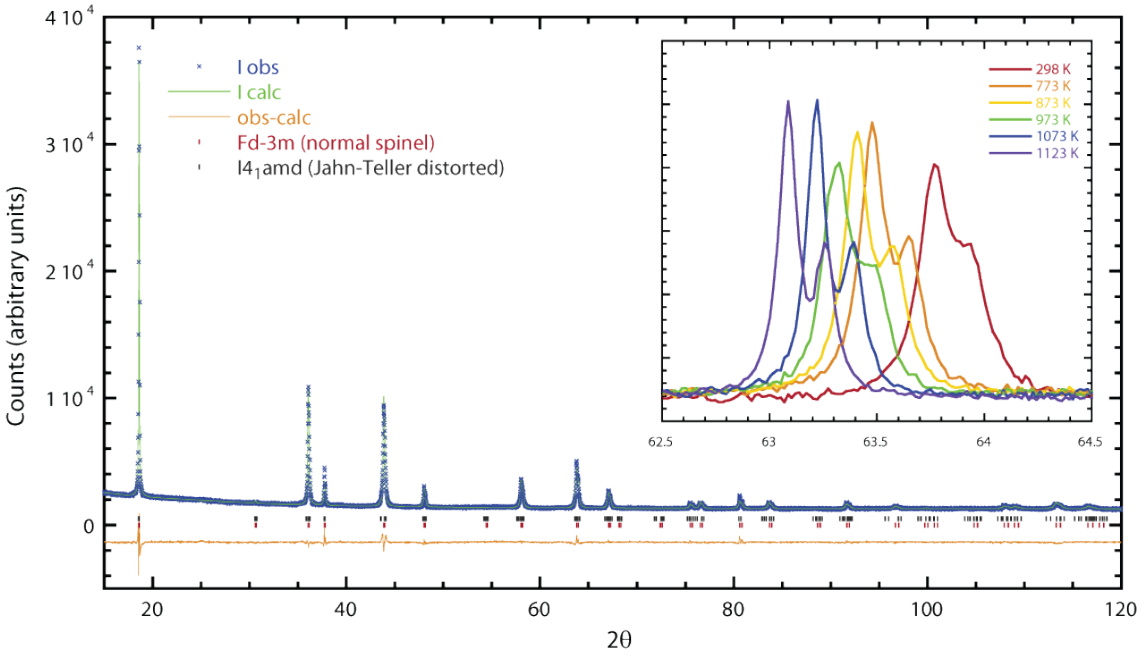

Figure 4.6. X-Ray diffraction pattern and Rietveld refinement results for $LiMn_2O_4$ at 298 K. The weighted residual, R_{wp}, for the refinement was 3.46% and the fraction of the undistorted spinel $LiMn_2O_4$ phase ($Fd\bar{3}m$) was 98.5 wt% with only 1.5 wt% tetragonal ($I4_1/amd$) $LiMn_2O_4$ phase. The inset shows the XRD pattern of the (440) reflection for the $Fd\bar{3}m$ phase for different temperatures. The lattice parameter increases with temperature evidenced by the peak shifting to smaller 2θ values. Also, the 298 K peak is considerably wider than the others because the lower symmetry tetragonal phase includes convolutions of two closely-spaced additional reflections; (224) at 63.5^o and (440) at 63.9^o.

The Rietveld refinement of room temperature XRD data is presented in Figure 4.6 with an inset showing elevated temperature data. (Table 4.4 has detailed results for all temperatures) With increasing temperature the XRD patterns visibly changed (see inset inFigure 4.6) in two ways: (1) the peaks shifted to smaller 2θ values as thermal expansion

Table 4.4. Structure refinement details for $LiMn_2O_4$ measured in air as a function of temperature (standard deviations in shift shown beneath in parenthesis)

T, K	a ($Fd\bar{3}m$), Å	u *	%Li A site, *y*	%Mn B site	R_{wp}%	wt% $I4_1/amd$
298 (first)	8.25138(7)	0.26195 (20)	94.7 (6)	97.3 (3)	3.46	1.5
773	8.29354(8)	0.26275 (20)	89.1 (7)	94.6 (3)	3.21	-
873	8.30474(8)	0.26271 (20)	87.3 (7)	93.7 (4)	3.21	-
973	8.31846(8)	0.26333 (20)	83.4 (7)	91.7 (4)	3.05	-
1073	8.33191(7)	0.26263 (20)	84.4 (7)	92.2 (3)	3.22	-
1123	8.34952(7)	0.26168 (20)	83.7 (6)	91.9 (3)	3.27	-
298 (last)	8.25209(7)	0.26177 (20)	95.2 (7)	97.6 (3)	3.22	-

** oxygen fractional coordinate, origin at inversion center ($\bar{3}m$) at octahedral vacancy (-1/8, -1/8, -1/8)*

caused the unit cell volume to increase and (2) the peak widths decreased and the distinction between Cu $K_{\alpha 1}$ and $K_{\alpha 2}$ increased. The peak widths are greatest at room temperature because of the presence of the tetragonal phase. The convolutions for additional peaks from the lower symmetry $I4_1/amd$ phase produce wider peaks. Although the weight fraction of the tetragonal phase refined to zero for all non-ambient temperatures, the width of the peaks at high temperatures do seem to very slightly, yet systematically decrease indicating that perhaps there is a very small amount of tetragonal phase remaining that is not being accounted for in the Rietveld refinement.

The coefficient of thermal expansion (CTE) is calculated to be 93-120 ppm/K over the range 298-1123 K based on the increase in the lattice parameter for the $LiMn_2O_4$ $Fd\bar{3}m$ phase. The compound also demonstrated slight anti-site disorder upon heating, that is to say, a fraction of Li^+ ions occupied the octahedral B 16(d) site instead of the tetrahedral A 8(a) site and Mn ions did the opposite (see Figure 4.7). At room temperature only 2.5% of the B site ions were Li^+ but by 1123 K the percentage had increased to 8.1%. The anti-site disorder can likely be ascribed to strain minimization as the larger Li^+ ions (ionic radius 73/90 pm for tetrahedral and octahedral coordination) respectively increase their coordination from 4 to 6. The smaller manganese ions (ionic radius 64/78.5 and 53/67 pm for high spin Mn^{3+} and Mn^{4+} in tetrahedral and octahedral coordination, respectively) decrease coordination. The ionic radius for Mn^{3+} in tetrahedral coordination is not available in the literature but was calculated from the average bond length $d(Mn_T^{3+} - O^{2-}) = 188(1)pm$ in spinels [196] taking the radius of O^{2-} as 124 pm

The anti-site disorder of $LiMn_2O_4$ structure with increasing temperature has not been reported previously. However, the structure of $LiMn_2O_4$ is very sensitive to cooling/ heating conditions and can undergo complex phase transformation and cation rearrangement since the lithium, manganese and oxygen stoichiometry are freely adjustable and the mean Mn oxidation state is not fixed.[197]

At the time of writing we do not have any independent experimental data confirming the occupancies of tetrahedral and octahedral sites by Mn^{3+} and Mn^{4+} ions.

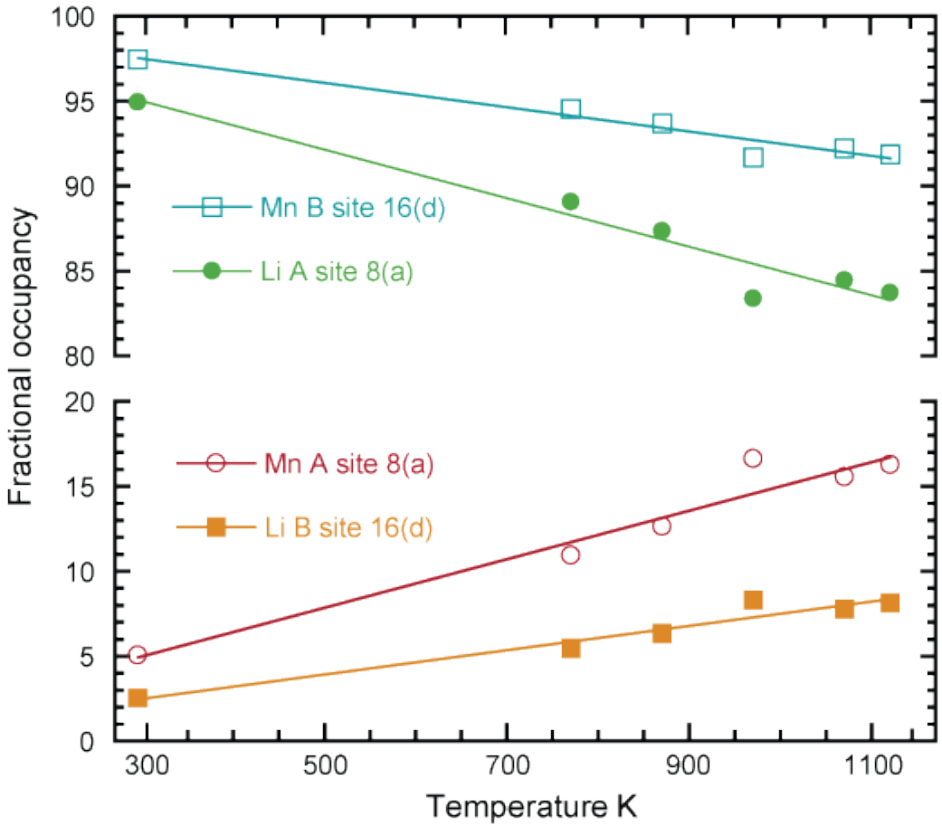

Figure 4.7. Fraction of the A (tetrahedral) and B (octahedral) sites in the $LiMn_2O_4$ spinel occupied by Li and Mn ions plotted against temperature. The lines represent linear best fits (R^2 = 0.971). Anti-site disorder on the B site is observed to increase linearly over the temperature range.

Instead, we estimated possible occupancies by comparing experimental (u=0.26195 / 0.26168 at 298 K and 1073 K, respectively) and calculated oxygen fractional coordinate (u) for $LiMn_2O_4$ employing different distortion models, i.e. occupancies of A-sites by (i) equal amount of Mn^{3+} and Mn^{4+} cations in $[Li_{1-i}{}^{+}Mn_{i/2}{}^{3+}Mn_{i/2}{}^{4+}]^{A}[Li_{i}{}^{+}Mn_{1-i/2}{}^{3+}Mn_{1-i/2}{}^{4+}]^{B}O_4$ (u=0.26223 / 0.26133), (ii) only by Mn^{3+} cations in $[Li_{1-i}{}^{+}Mn_{i}{}^{3+}]^{A}[Li_{i}{}^{+}Mn_{1-i}{}^{3+}Mn_{1}{}^{4+}]^{B}O_4$ and (u=0.26240 / 0.26183), (iii) only by Mn^{4+} cations in $[Li_{1-}$

$_i^{+}Mn_i^{4+}]^A[Li_i^{+}Mn_1^{3+}Mn_{1-i}^{4+}]^BO_4$ (u=0.26207 / 0.26084) and (iv) that in undistorted $[Li^+]^A[Mn^{3+}Mn^{4+}]^BO_4$ spinel (u=0.26269). The oxygen fractional coordinate, u, was calculated according to Equations 4.4-4.7 [198] using the experimentally determined fractional occupancy ,i, of Li^+ on A sites (i=0.01y, see Table 4.4):

$$u = 0.25 + \left\{ 0.375 - \left[0.3876 \left(\frac{\langle r(B) \rangle}{\langle r(A) \rangle} \right)^{0.07054} \right] \right\}, \quad 4.4$$

$$\langle r(M) \rangle = 0.33 \langle r(A) \rangle + 0.67 \langle r(B) \rangle, \quad 4.5$$

$$\langle r(A) \rangle = i_{Li^A} r_{tetr}(Li) + (1 - i_{Li^A}) r_{tetr}(Mn^{3+/4+}), \quad 4.6$$

$$\langle r(B) \rangle = 0.5 i_{Li^B} r_{oct}(Li) + (1 - i_{Li^B}) r_{oct}(Mn^{3+/4+}). \quad 4.7$$

As the distortion of the spinel structure is small, the comparison between experimental and calculated structural parameters given above does not provide unambiguous evidence for preferential site occupancies. Our assessment is that the fraction of octahedral Mn^{4+} lies in the range between 0.46 and 0.54 at 1073 K. However, as we have found that the lattice parameter of the cubic $LiMn_2O_4$ increases with temperature, we can exclude the possibility of an increase in mean oxidation state of manganese (for this, an opposite effect will be observed [197]). According to TGA data,[199] at T > 1053 K $LiMn_2O_4$ loses oxygen becoming nonstoichiometric. This is not the case for our study. Since we also did not observe the decomposition of $LiMn_2O_4$, which

typically happens at T > 1113 K (XRD) upon heating in air,[199] we can exclude the formation of delithiated and manganese deficient spinels.

Summarizing, our in-situ heating XRD characterization has unambiguously demonstrated that: (i) single-phase undistorted normal $LiMn_2O_4$ spinel is stable over a broad temperature range (298-1123 K) and, (ii) the inversion of spinel structure is less than 8% even at the highest temperature studied (1123 K). Therefore, as $LiMn_2O_4$ is free of a Jahn-Teller distortion it provides a model to ascertain the contribution of the electron degeneracy term to the thermopower of Mn^{3+}/Mn^{4+} in the $LiMn_2O_4$ compound.

Electrical conductivity

The temperature dependence of the electrical conductivity is consistent with previous measurements on $LiMn_2O_4$. For example, Figure 4.8 shows the electrical resistivity approaching a minimum value of 9 mΩ cm. This is comparable to the high temperature Ioffe-Regel limit [200] of 2 mΩ cm where the carrier mean free path is nearly equal to the lattice constant given by

$$\rho = \frac{3\pi^2\hbar}{q^2\hat{a}k_F^2} \qquad 4.8$$

where $\hbar$ is the reduced Planck's constant, $\hat{a}$ is the Mn-O-Mn distance (estimated to be 0.4 nm) and k_F^2 is the three dimensional Fermi wave vector.[136] The activation energy, E_A, for small polaron conduction was calculated to be 0.36±0.01 eV by plotting $ln(\sigma T)$ against

1/T and setting the slope equal to $-E_A/k_B$ (see inset to Figure 4.8). This value agrees well with the 0.4 eV reported experimentally [136,194] for small-polaron conduction in $LiMn_2O_4$ but contrasts with a recent computational study using density functional theory (DFT).[201] In that study, the activation energy was found to be 0.34 eV

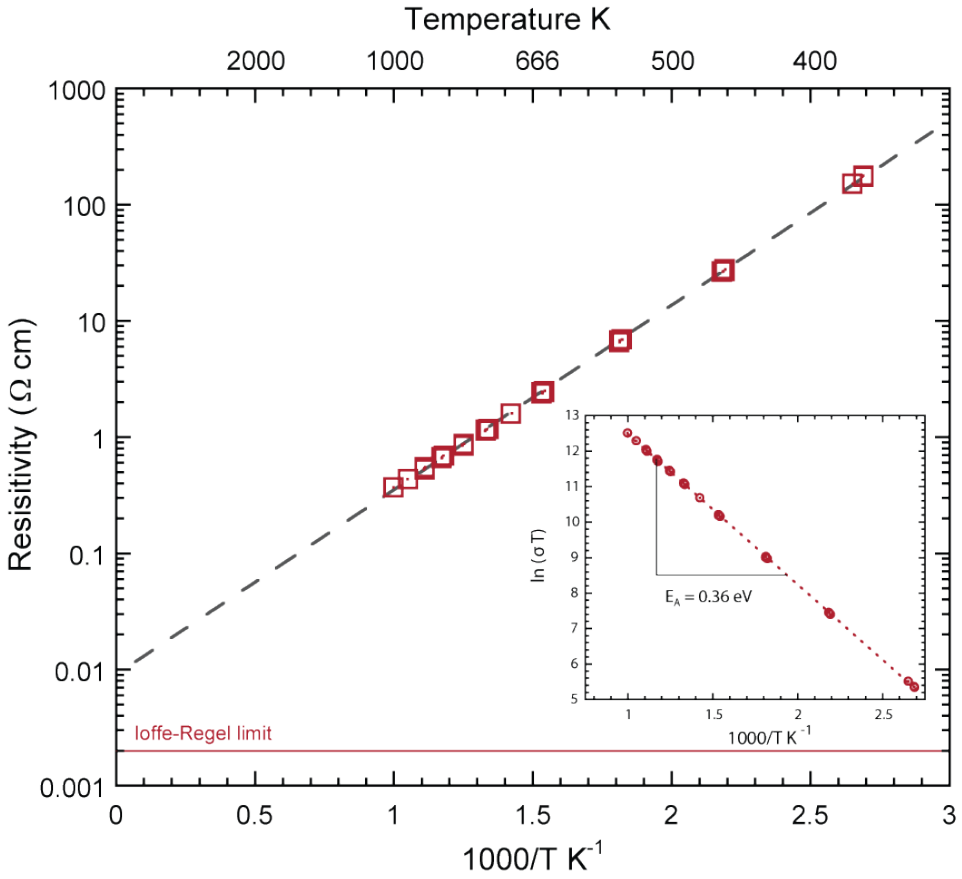

Figure 4.8. Arrhenius plot of the electrical resistivity. The high temperature value of the $LiMn_2O_4$ series approaches (dashed line) 9 mΩ cm, close to the Ioffe-Regel limit (solid line) of 2 mΩ cm for a mean free electron path of 2.9 Å. The inset is an Arrhenius plot confirming small-polaron conduction with an activation energy of 0.36±0.01 eV.

when a Jahn-Teller distortion was associated with the high-spin Mn^{3+} ions. Interestingly, in the case where there was no Jahn-Teller distortion, the activation energy was significantly lower, 0.062 eV.

Seebeck Coefficient

In contradiction to an earlier thermopower report for $LiMn_2O_4$ [194] the thermopower measured in this work reaches a high temperature value of -73 μV/K. Interestingly, this value is more than 3 times larger than previously reported in small-polaron conducting manganates (see Figure 4.9). It is, however, fully consistent with the high temperature limit of the modified Heikes formula (see Equation 2.30 and Figure 4.4) for small-polaron conduction between undistorted octahedrally coordinated Mn^{3+} and Mn^{4+} ions.

In the following paragraphs we address the effect of anti-site disorder on thermopower. Koshibae et al. [114] shows that when multiple ion pairs are present (which differ either in oxidation state or coordination environment, for example, Mn^{3+} /Mn^{4+} on tetrahedral and octahedral sites) the total thermopower should simply be the weighted fraction of each pair's contribution:

$$S = \frac{-k_B}{q}\left\{\ln\left(\frac{g_{i,c}}{g_{i,c}}\frac{y_c}{1-y_c}\right)\frac{c}{c+d} + \ln\left(\frac{g_{j,c}}{g_{j,c}}\frac{y_d}{1-y_d}\right)\frac{d}{c+d}\right\}, \qquad 4.9$$

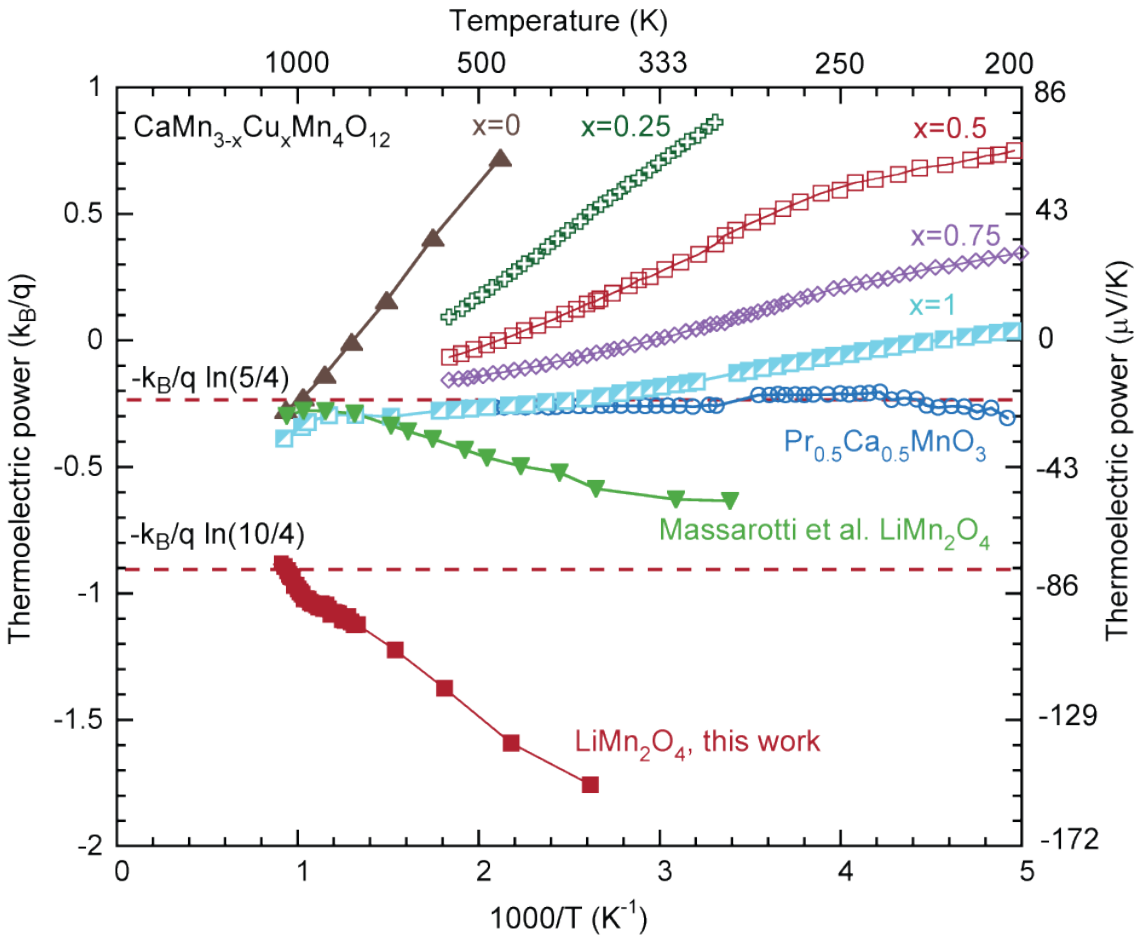

Figure 4.9. Thermopower versus temperature for $LiMn_2O_4$ from this work compared with other Mn compounds as reported by Kobayashi et al. [136] The dashed lines at -19 and -79 μV/K represent the predictions based on the high temperature limit of the Heikes formula for Mn^{3+} /Mn^{4+} ions in equal concentration with and without a Jahn-Teller distortion ($g_{(I)}/g_{(II)}$= 5/4 or 10/4). The measured values reach -73 μV/K in good agreement with the Heikes formula for an undistorted structure.

Here c and d are fractions of each ion pair, $g_{(i,j),(c,d)}$ is the electron degeneracy of the ion pairs (i,j) on sites (c,d) and $y_{(c,d)}$ is the fraction of Mn^{4+} on each site. Considering

contributions only from Mn^{3+} /Mn^{4+} pairs and assuming their equal distribution between tetrahedral and octahedral sites ($x_c = x_d = 0.5$), we obtain for 1073 K

$$S = \frac{-k_B}{q}\left\{0.06\ln\left(\frac{15}{12}\right) + 0.94\ln\left(\frac{10}{4}\right)\right\}, \qquad 4.10$$

Evaluation of this expansion indicates only a slight reduction in thermopower from -79 to -75 μV/K due to anti-site disorder.

Summarizing, $LiMn_2O_4$ samples with the cubic ($Fd\bar{3}m$) spinel structure exhibit a large n-type high temperature thermopower of -73 μV/K. This large thermopower is larger relative to other mixed valence Mn^{3+} /Mn^{4+} compounds studied previously. The increase in thermopower can be understood as due to an absence of a Jahn-Teller distortion in cubic $LiMn_2O_4$ as verified by high temperature *in-situ* XRD. Relative to the structure with a Jahn-Teller distortion, the orbital degeneracy is doubled. As a result, the electron degeneracy ratio $g_{(I)}/g_{(II)}$ for the two ions involved in small-polaron conduction, Mn^{3+} & Mn^{4+}, is increased from 5/4 (Jahn-Teller distorted) to 10/4 (Jahn-Teller distortion free). Our experimentally observed high temperature thermopower of -73 μV/K is consistent with the prediction of the thermopower from the modified Heikes formula (-79 μV/K) using this latter value of the electron degeneracy.

4.3 Anti-site Disorder in $Li_xMg_{1-x}Mn_2O_4$ and $Mn_xFe_{1-x}Ni_yCr_{2-y}O_4$ Spinels

In the remainder of this chapter we examine the effect of anti-site disorder on thermopower in other strongly correlated spinels. The $Li_xMg_{1-x}Mn_2O_4$, series of compounds provide an excellent segue and to compare Jahn-Teller distortions and anti-site disorder. Then we discuss anti-site disorder in $Fe_xMn_{1-x}Ni_{2-y}Cr_yO_4$ x=0, ¼, ½, ¾, 1 and y=0,1,2 spinels addressing specifically the contribution from tetrahedral sites to thermopower in spinels. We will return to this subject in greater detail in the following chapter (Chapter 5) on thermopower as a structural characterization tool.

4.3.1 Universal Charge Transport

In Section 2.3.1 we derived the modified Heikes formula and observed that the thermopower depends strongly on the carrier concentration. This can be seen clearly in Figure 2.2. When the majority of oxide thermoelectric materials are doped with aliovalent ions such that the oxidation state of the conducting ions is altered the carrier concentration and thermopower are changed as well.[24,136,139,140] For example, the oxygen nonstoichiometry of $RBaCo_2O_{5+x}$ (R=Gd, Nd) compounds is altered by quenching samples from different temperatures. As oxygen vacancies are introduced charge neutrality is accomplished by altering the mean oxidation state of the Co ions. When the carrier concentration is quantified by titration and the measured thermopower is compared to that predicted by the modified Heikes formula good agreement is observed.[140]

An unusual deviation in the modified Heikes formula is observed for mixed valence oxide manganates.[136] In what the authors termed universal charge transport, the thermopower of $CaMn_{3-x}Cu_xMn_4O_{12}$ x=0, ¼, ½, ¾, 1 compounds was inexplicably found to be independent of the carrier concentration. Despite the average oxidation state of Mn ions shifting from +3.25 to +3.5 the thermopower of all the compounds approached the same high temperature limit, -25 μV/K, corresponding to an average oxidation state of +3.5, or equal concentrations of Mn^{3+} and Mn^{4+}.

In order to examine the feasibility of universal charge transport further we selected candidate oxides with different Mn^{3+} /Mn^{4+} ratios. To do so we turned to the closely related field of mixed valence oxides as cathode materials for lithium ion batteries. In that body of work, a number of lithium manganese spinels have been identified with variations of the mean oxidation state of manganese. As shown in Figure 4.10, a number of lithium manganese spinels with different mean oxidation states of manganese and /or site occupancies are possible.[197,202] In this work, we also show that it is possible to produce variations, and even a change in the sign of thermopower, by altering the mean oxidation state of manganese, and therefore the fraction x of Mn^{4+} ions.

In order to alter the Mn^{3+} /Mn^{4+} ratio in lithium manganese spinels several strategies can be employed including: (i) doping with aliovalent ions to substitute for Li^+ on tetrahedral sites, (ii) synthesis of cation-mixed $[Li]^A[Li_z^+Mn^{3+}Mn_{1-z}^{4+}]^BO_4$ and delithiated $[Li_{1-z}]^A[Mn_{1-z}^{3+}Mn_{1+z}^{4+}]^BO_4$ spinels, and, finally, (iii) post-synthesis

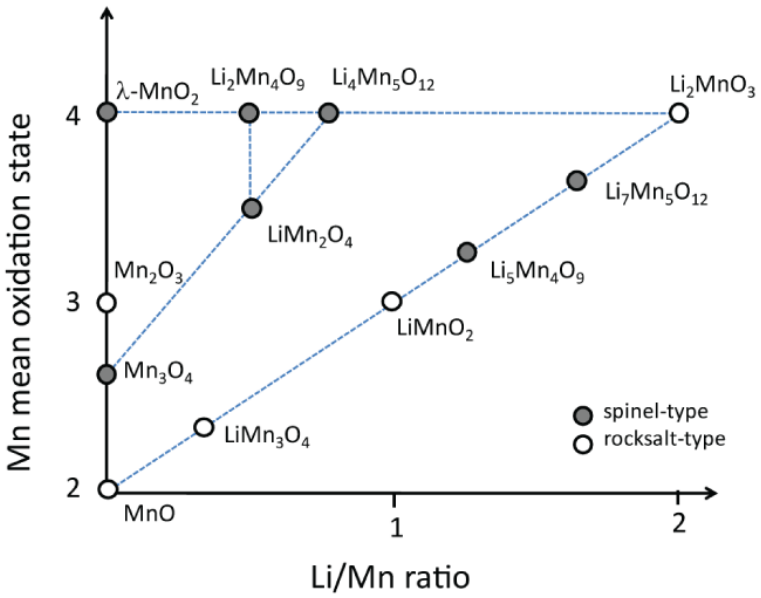

Figure 4.10. Mean oxidation state of manganese ions and Li/Mn ratio for different Li-Mn-O compounds. Figure modified from Julien et al.[202]

processing and measurements of $LiMn_2O_4$ in oxygen-deficient atmospheres. The first strategies, (i) will be considered now, and the final strategy (iii) will be described in the next section (4.3.2).

Single phase, dense samples of $Mg_{1-x}Li_xMn_2O_4$ x=0, 1/5, 2/5 were obtained by combustion of oxalates and CADPro sintering. The X-ray diffraction patterns are presented in Figure 4.11. The scans were not optimized for high resolution (fast collection times, large slits) but the peaks seem to correspond well with the cubic structure and only the x=2/5 sample has significant peak broadening. Curiously, the peaks shift to larger 2θ values indicative of a lattice parameter decrease with Li content in contradiction to expectations based on the change ionic radii for Li^+ and Mg^{2+} (r_A^{Li+}=0.59

Å, r_A^{Mg2+}=0.57 Å, r_B^{Li+}=0.76 Å, r_B^{Mg2+}=0.66 Å). However, this observation could be explained by a small shift displacement in the sample height during diffraction (higher quality patterns are needed before Rietveld refinement can determine the shift displacement).

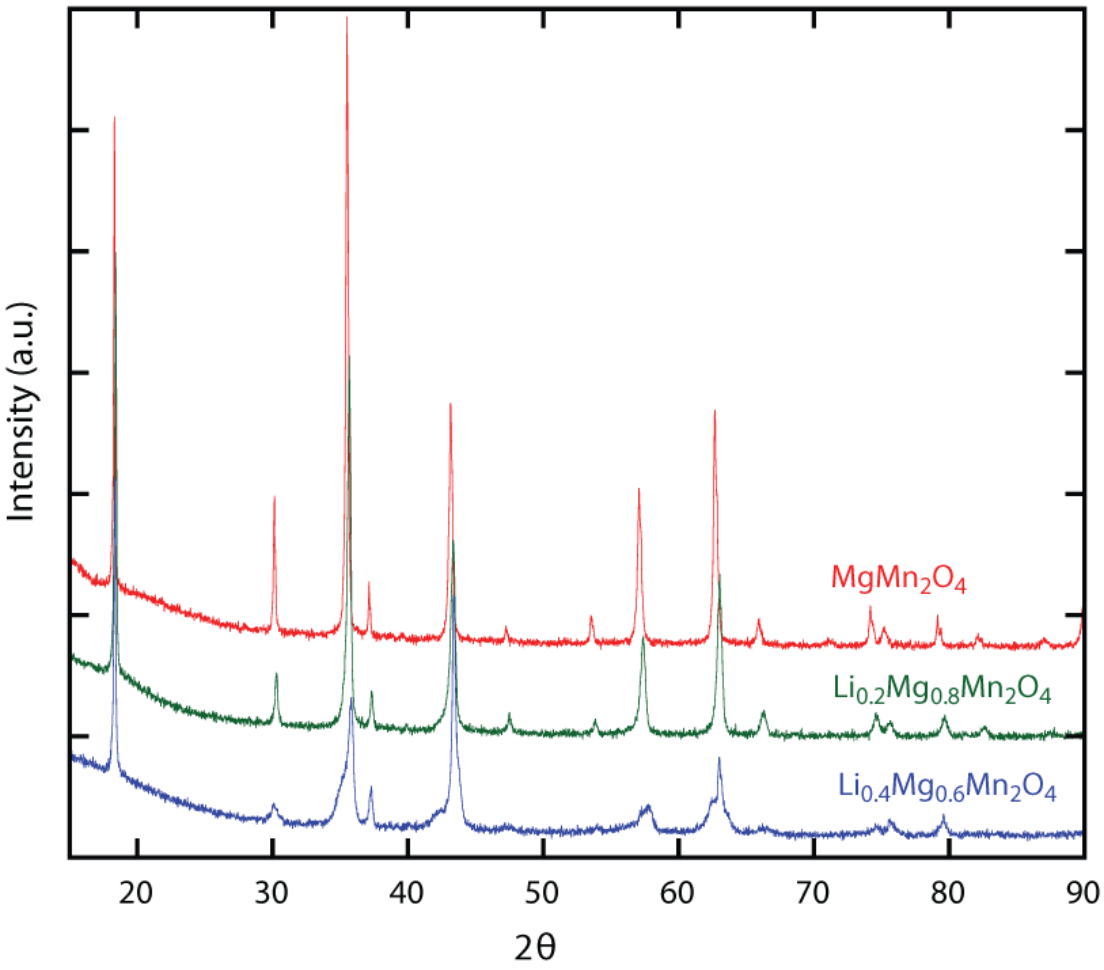

Figure 4.11. X-Ray diffraction $Mg_{1-x}Li_xMn_2O_4$ x=0, 1/5, 2/5 samples. The x=2/5 sample has significantly broader peaks which could be due to a secondary phase.

An Arrhenius plot (see Figure 4.12) of the conductivity shows little change in the slope for different $Mg_{1-x}Li_xMn_2O_4$ samples so the activation energy is not changed significantly. The x=1/5 and x=2/5 samples have comparable electrical conductivity compared to undoped $LiMn_2O_4$, but the the x=0 sample, $MgMn_2O_4$ is lower.

In all three Mg doped samples, there is a reduced oxidation state for the manganese cation relative to $LiMn_2O_4$. Reducing the oxidation state means the fraction of Mn^{4+} is reduced which, in turn, should lead to positive thermopower values (>300 μV/K for x=0, 110 μV/K for x=1/5 and 40 μV/K for x=2/5). However, as seen in Figure 4.12, the thermopower of the x=0 and x=2/5 compounds reach -20 to -25 μV/K at high temperatures in very good agreement with the distorted limit observed for other manganese oxides whereas the x=1/5 compound reached -70 μV/K in good agreement with the undistorted limit. It isn't clear why the x=1/5 compound reaches the undistorted limit while the other two correspond to a distorted limit. High resolution optimized X-ray diffraction is still needed, particularly at high angles, to probe for evidence of tetragonal Jahn-Teller distortion in the x=0 and x=2/5 compounds. Nevertheless, these intriguing results are a second evidence of the universal charge transport phenomenon first observed by Kobayashi et al. whereby the thermopower seems to be invariant to the carrier concentration.

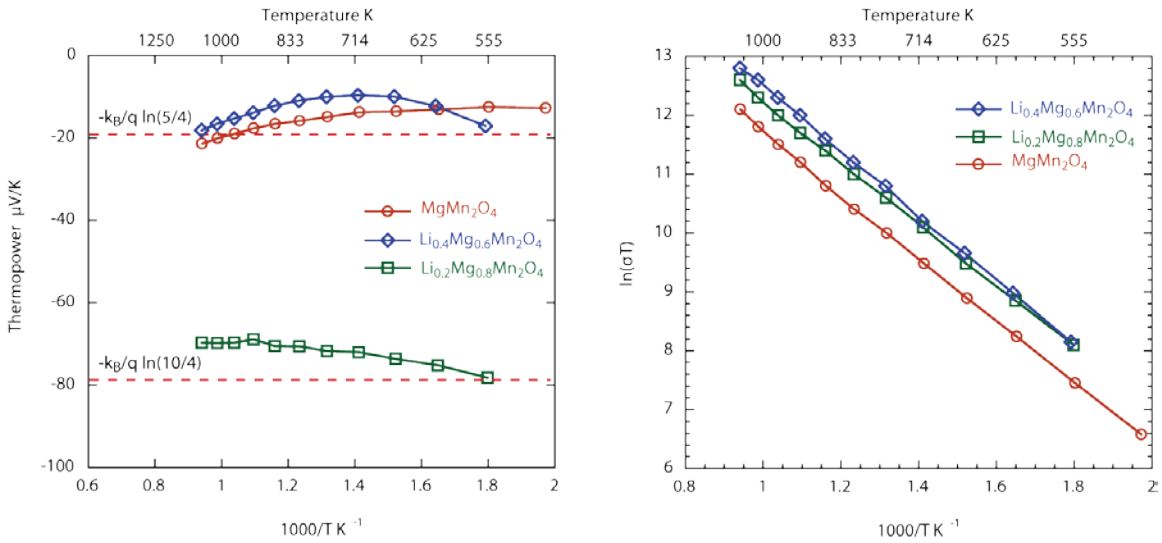

Figure 4.12. Thermopower (left) and electrical conductivity (right) of $Mg_{1-x}Li_xMn_2O_4$ x=0, 1/5, 2/5 compounds. The thermopower of the compounds approached either the Jahn-Teller distorted or undistorted limits despite the variation in Mn^{3+}/Mn^{4+} ratio due to doping. The activation energy is similar for all compounds, including undoped, stoichiometric $LiMn_2O_4$.

4.3.2 N to P-type Transition in Oxygen Deficient $LiMn_2O_4$

In contrast to samples sintered in air, $LiMn_2O_4$ specimens densified under vacuum (CADPro) crystallized in the tetragonal structure exhibiting a Jahn-Teller distortion. Rietveld refinement of *in-situ* high temperature XRD performed in argon indicates a three phase mixture of $LiMn_2O_4$ ($I4_1/amd$, a=5.653Å, c=9.329Å, Z=4), $LiMnO_2$ (Pmnm, a=2.823Å, b=5.749Å, c=4.575Å, Z=2) and Mn_3O_4 (Hausmannite, $I4_1/amd$, a=5.755Å, c=9.462Å, Z=4). From room temperature up to 950 K the majority phase (60-70 wt%) is the tetragonally distorted $LiMn_2O_4$ but this phase decomposes to a mixture of Mn_3O_4 (60-40 wt%) and $LiMnO_2$ at temperatures above 950 K (see Figure 4.13). Upon cooling back

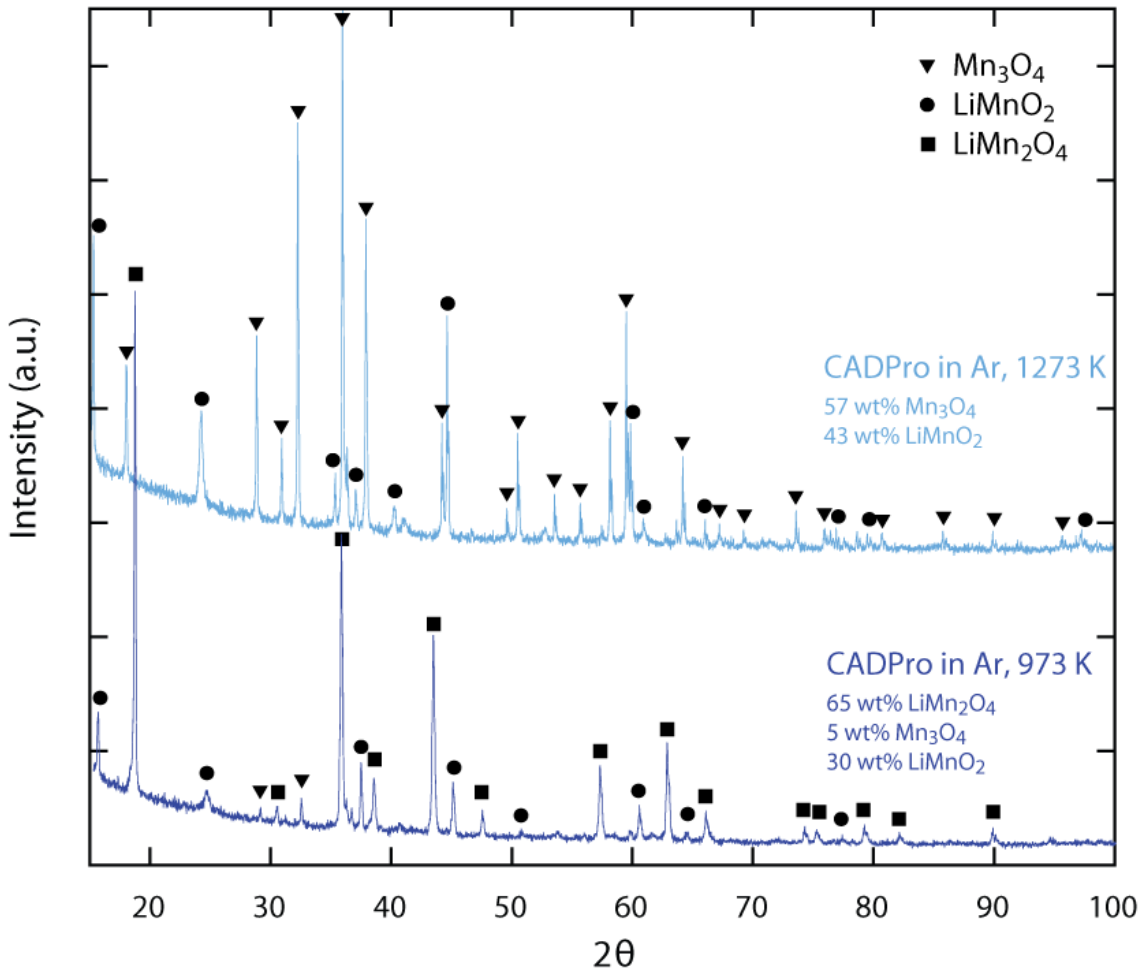

Figure 4.13. In-situ high temperature X-Ray diffraction pattern, measured in argon, of $LiMn_2O_4$ after CADPro. The sample is a mixture of spinel, Mn_3O_4 and $LiMnO_2$ below 973 K, at high temperatures the spinel phase decomposes entirely leaving only Mn_3O_4 and $LiMnO_2$.

to room temperature the only phase present is, again, the undistorted cubic spinel $LiMn_2O_4$ ($Fd\bar{3}m$, a=8.251, Z=8).

The decomposition of $LiMn_2O_4$ into Mn_3O_4 and $LiMnO_2$ is accompanied by a dramatic n-type to p-type shift in thermopower of approximately 400 μV/K (see Figure

4.14). Above 950 K the thermopower of this specimen (measured in He) approaches large positive values of about 400-500 μV/K agreeing well with thermopower measured for pure Mn_3O_4 in air. The origin of large positive thermopower in tetragonal Mn_3O_4 (i.e. $(Mn^{2+})^A[Mn_2^{3+}]^BO_4$) is still under debate.[203,204] Taking into account the disproportionation at high temperatures to $(Mn^{2+})^A[Mn_x^{2+}Mn_{2-2x}^{3+}Mn_x^{4+}]^BO_4$ and assuming that the tetrahedral concentrations of Mn^{3+} /Mn^{4+} are negligible, we obtain from Equation 2.30 the Mn^{4+} fraction x as being <0.01. Upon cooling, the sample transformed completely to cubic $LiMn_2O_4$. The shift in thermopower between points 1 and 4 in Figure 4.14 is attributed to the removal of the Jahn-Teller distortion after heating the reduced material above 950 K. When the chamber is vented with air and the same sample is remeasured the thermopower reaches the high temperature value of -79 μV/K.

Summarizing, there is a reversible transition from large negative (-79 μV/K) to large positive (400-500 μV/K) thermopower upon the phase transformation $LiMn_2O_4 \leftrightarrow Mn_3O_4$. Although this cannot be independently confirmed, the observation provides strong evidence for the influence of mean oxidation state of manganese on thermoelectric properties in spinels.

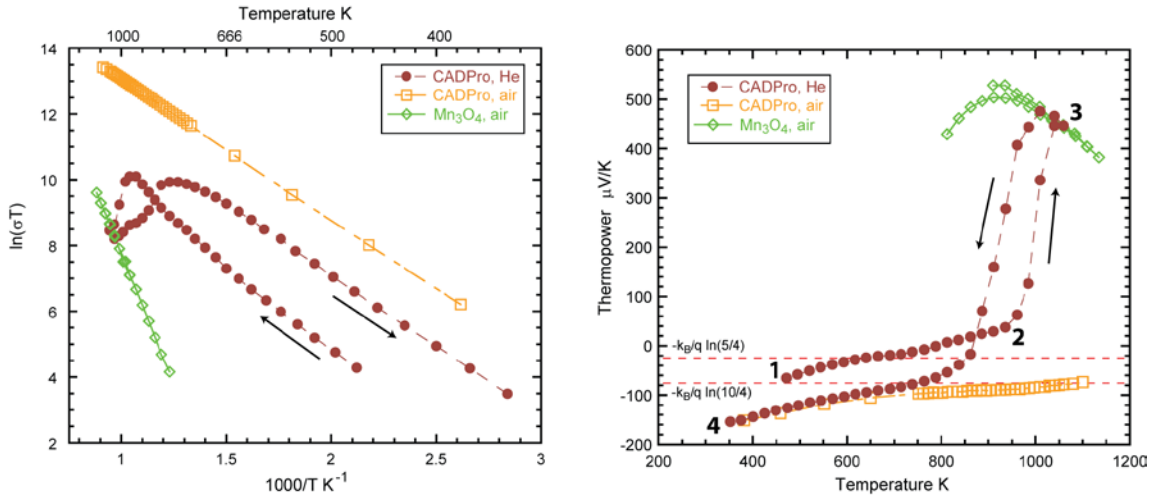

Figure 4.14. Electrical conductivity (left) and thermopower (right) of $LiMn_2O_4$ pressed in a reducing atmosphere. The sample was measured in He first (circles) and upon cooling the chamber was filled with air and the thermopower was re-measured (squares). The numbers 1-4 are points at which quantitative X-ray phase analysis was performed to determine weight fraction of phases. At points 1 and 2 the phase fraction is a majority (60-70 wt%) $LiMn_2O_4$ ($I4_1/amd$) with Mn_3O_4 and $LiMnO_2$ impurities. At point 3 the $LiMn_2O_4$ has decomposed entirely to 60 wt% Mn_3O_4 and 40 wt% $LiMnO_2$. The thermopower of Mn_3O_4 (diamonds) is shown for comparison. Upon cooling to point 4 the sample converts entirely to cubic spinel $LiMn_2O_4$.

4.3.3 Substitutions on the Tetrahedral Site in Spinels

In order to calculate the thermopower in spinels, typically only contributions from the octahedral sites are considered, ignoring possible contributions from tetrahedral sites. Whether or not this is a valid assumption that is appropriate for all spinels is a central question that will be discussed in the next chapter. In this final section of Chapter 4, however, we describe our initial attempt to observe a change in thermopower due only to

anti-site disorder on the tetrahedral site in $Fe_xMn_{1-x}Ni_{2-y}Cr_yO_4$ x=0, ¼, ½, ¾, 1 and y=0,1,2 series.

The B site cations, Ni^{2+} and Cr^{3+}, were selected as ions to occupy the octahedral site since having 3 and 8 d-shell electrons, respectively, they would either half fill the t_{2g} band or fill the t_{2g} band and half fill the e_g band. These electronic configurations are expected to be very stable and should, therefore, minimize inversion of the spinel structure allowing us to independently control the A site anti-site disorder. The experimental hypothesis is that ions on tetrahedral sites may contribute to thermopower. Therefore, if the Ni and Cr ions remain on the B site but the A site is altered from pure Fe^{3+} to pure Mn^{3+} any change in thermopower can be attributed to tetrahedral contribution.

The compounds designed to have only Ni or only Cr on the B site (y=0 and y=2) resulted in mixed phase materials with $(Cr,Fe)_2O_3$ or NiO impurities (see Figure 4.15 and Figure 4.16).

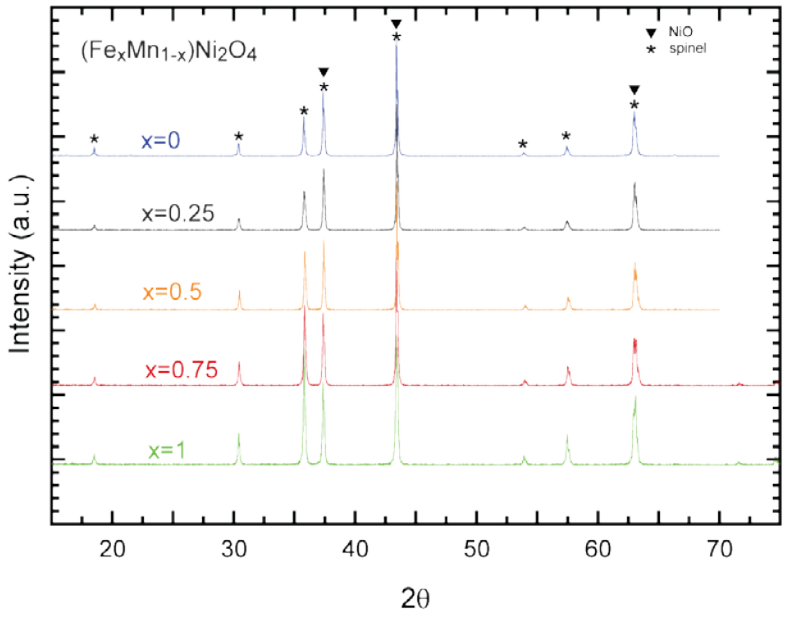

Figure 4.15. X-Ray diffraction of $Fe_xMn_{1-x}Ni_2O_4$ x=0, ¼, ½, ¾, 1 compounds. NiO impurities are observed in all compounds.

The $Fe_xMn_{1-x}NiCrO_4$ x=0, ¼, ½, ¾, 1 compounds appeared by laboratory XRD to be pure phase spinel (see Figure 4.17). Samples featuring A site disorder (x=½, ¾) had reduced electrical conductivity and thermal diffusivity measurements relative to the pure end member samples (x=0, 1) (see Figure 4.18 and Figure 4.19)

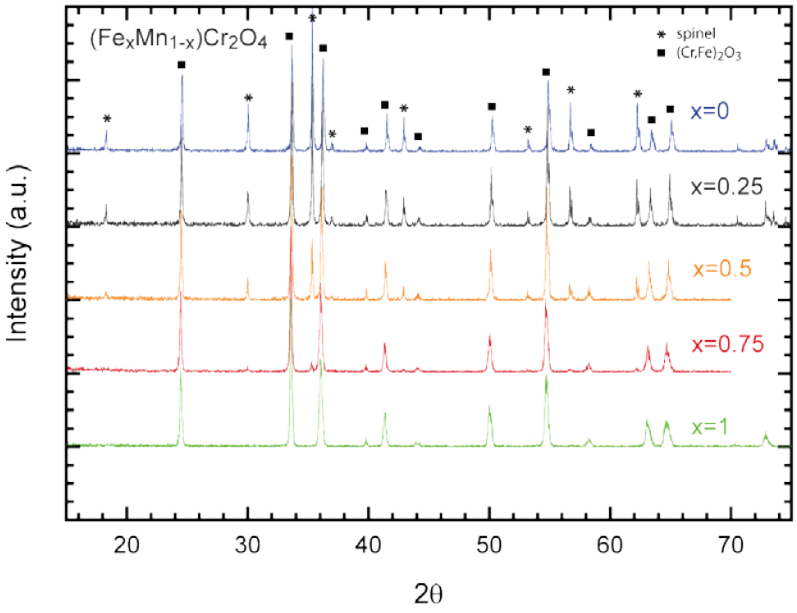

Figure 4.16. X-Ray diffraction of $Fe_xMn_{1-x}Cr_2O_4$ x=0, ¼, ½, ¾, 1 compounds. $(Cr,Fe)_2O_3$ impurities are observed in all compounds but x=1.

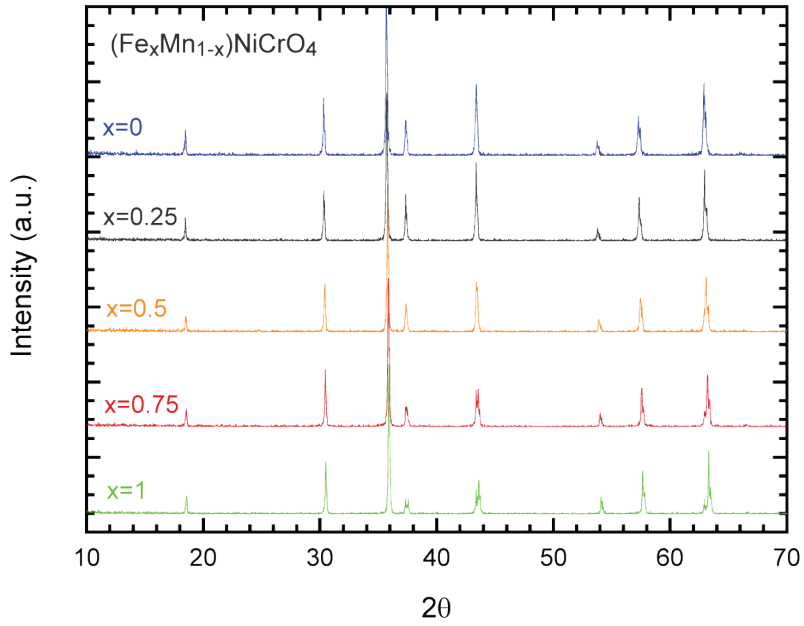

Figure 4.17. X-Ray diffraction of $Fe_xMn_{1-x}NiCrO_4$ x=0, ¼, ½, ¾, 1 compounds.

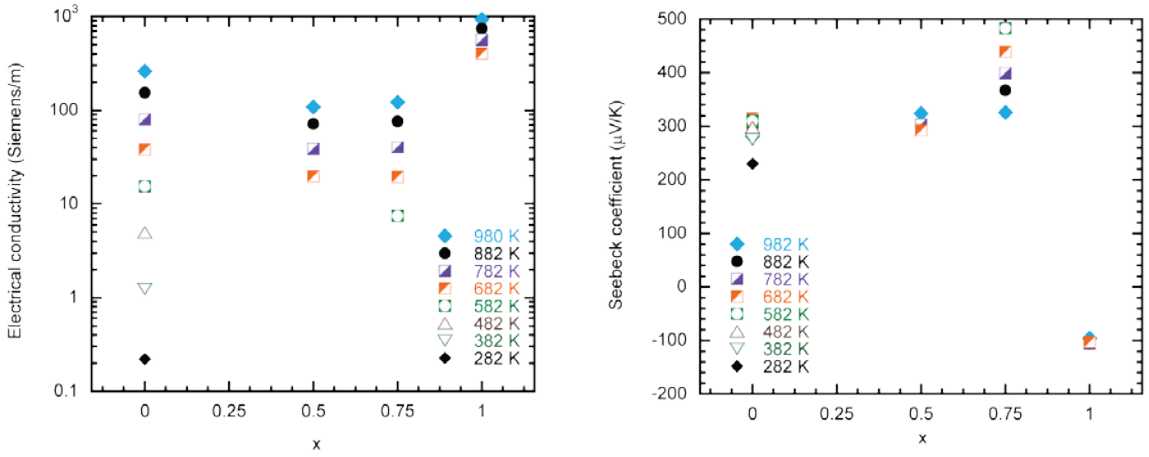

Figure 4.18. Electrical conductivity (left) and thermopower (right) of $Fe_xMn_{1-x}NiCrO_4$ x=0, ½, ¾, 1 compounds.

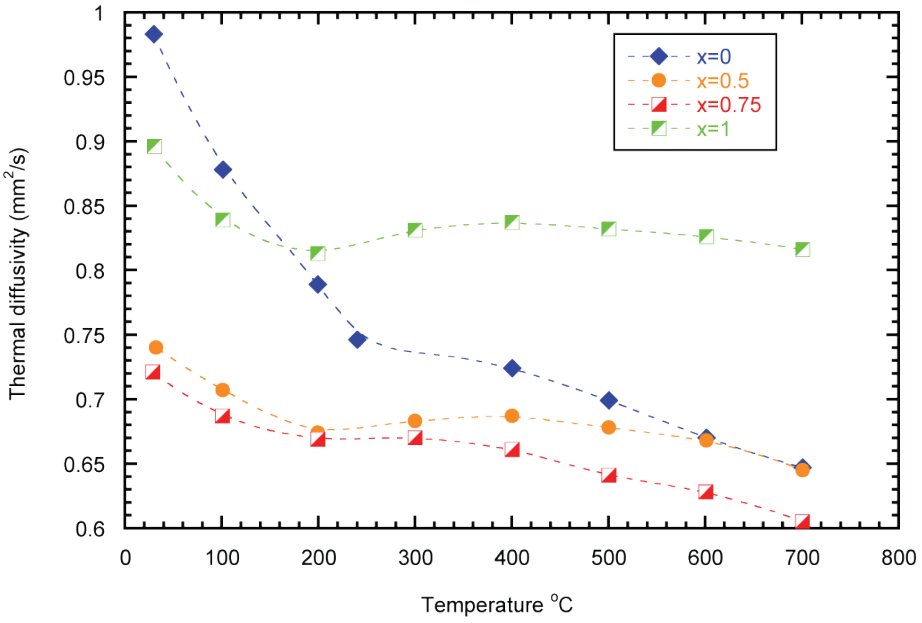

Figure 4.19. Thermal diffusivity of $Fe_xMn_{1-x}NiCrO_4$ x=0, ½, ¾, 1 compounds.

The reflections from $Fe_xMn_{1-x}NiCrO_4$ x=0, ½, ¾, 1 spinels and NiO impurities overlap strongly so to ensure that pure phase spinels were obtained synchrotron diffraction was measured for the series. The results of the synchrotron diffraction, shown in Figure 4.20, demonstrate that the samples, while being a majority spinel phase, contain significant amounts of NiO and unreacted Ni impurities. The fraction of NiO impurities decreases linearly from ~22% to ~10% across the series with increasing iron content (see Figure 4.21). An unfortunate consequence of the impurities is that the composition of the

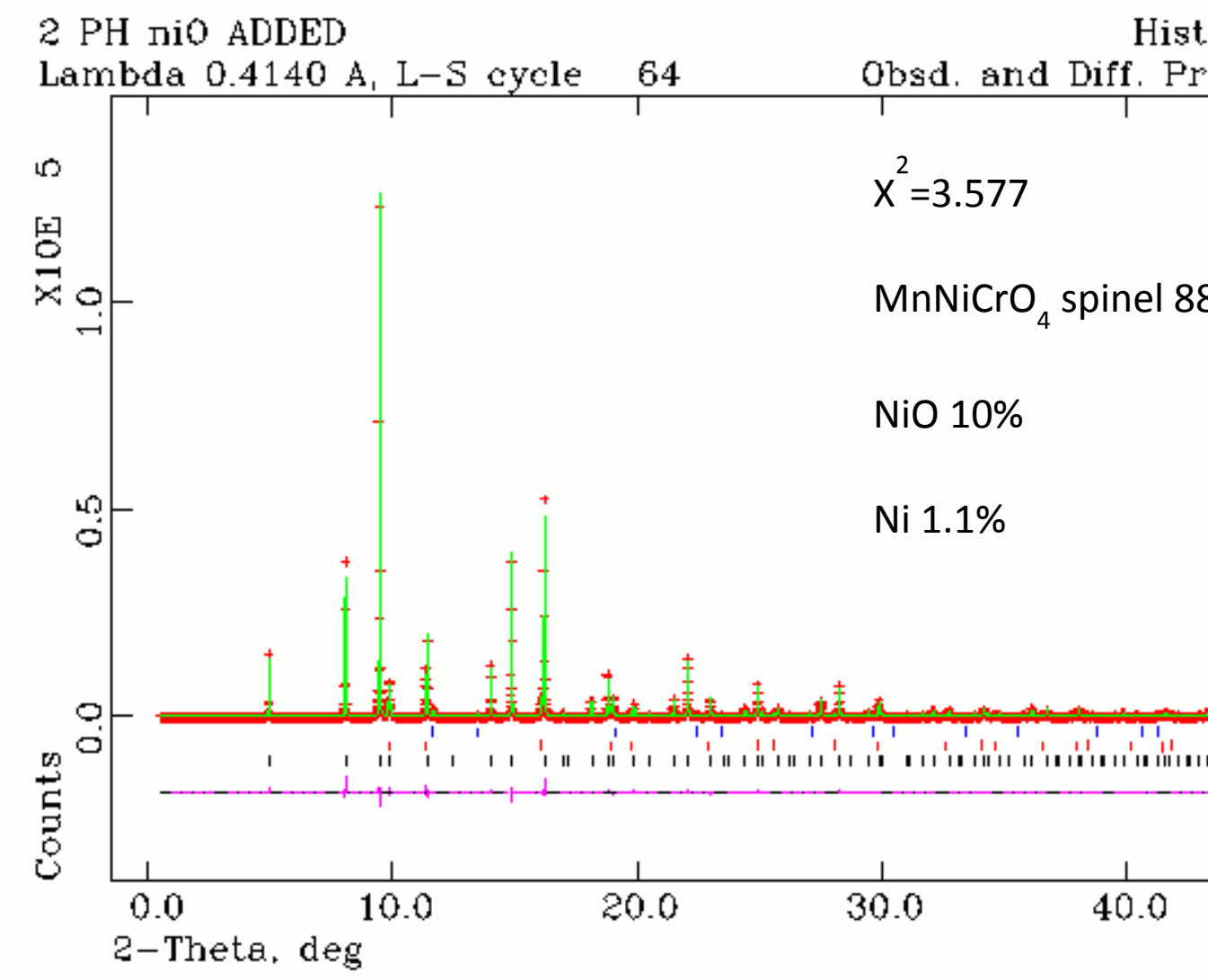

Figure 4.20. Synchrotron diffraction pattern of $MnNiCrO_4$. The compound is a majority (88.9%) spinel but has significant NiO and unreacted Ni impurities. These impurities suggest the stoichiometry of the spinel has been altered.

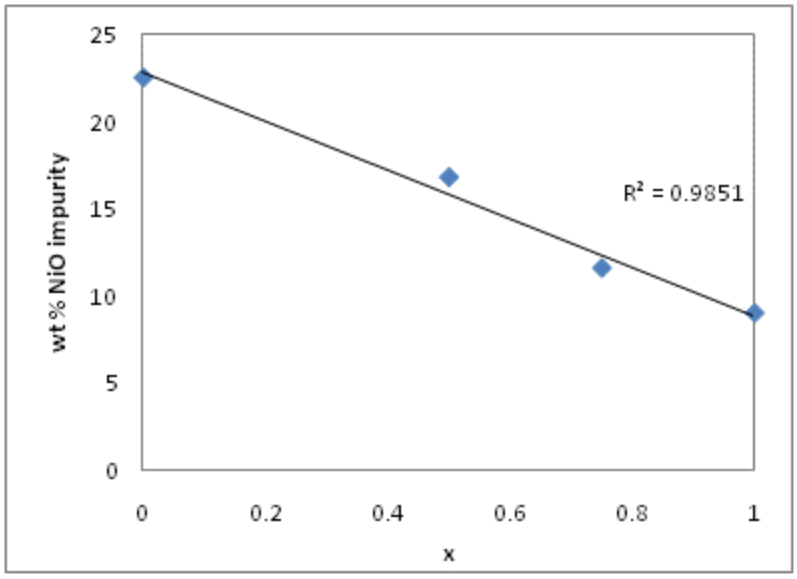

Figure 4.21. Weight fraction of NiO impurity in $Fe_xMn_{1-x}NiCrO_4$ x=0, ½, ¾, 1 compounds determined by quantitative phase analysis using synchrotron diffraction. With increasing iron content the NiO fraction decreases. The line is a linear best fit.

spinel phase is no longer known. For example, if the original cation ratio for $MnNiCrO_4$is $[Mn] = [Cr] = [Ni]$ but some of the Ni is used up to form NiO and Ni then the ratio for the spinel has been altered $[Mn] = [Cr] \neq [Ni]$ and a nickel deficient spinel is obtained. As a result of the impurities, deviation from spinel composition and unknown cation distribution we can draw no firm conclusions in this section regarding the role of tetrahedral site contribution to thermopower in spinels.

Summarizing, in this chapter the thermopower of $LiMn_2O_4$, Mg-doped $LiMn_2O_4$ and $Fe_xMn_{1-x}NiCrO_4$ spinels was investigated and correlations to structural distortions, crystal field and anti-site disorder were assessed. An argument was presented that larger thermopower can be obtained if Jahn-Teller distortions in manganese oxides are avoided.

Another evidence of universal charge transport was observed in Mg-doped $LiMn_2O_4$ samples. Regardless of the mean oxidation state of manganese ions the thermopower of the samples corresponded to an equal fraction of Mn^{3+} and Mn^{4+} with a Jahn-Teller distortion ($MgMn_2O_4$, $Mg_{0.6}Li_{0.4}Mn_2O_4$) or without ($Mg_{0.8}Li_{0.2}Mn_2O_4$). Finally, $Fe_xMn_{1-x}NiCrO_4$ spinels were synthesized to probe whether or not anti-site disorder on the tetrahedral site would alter thermopower. However, due to the formation of significant NiO and Ni impurities, the chemical composition and cation distribution of the remaining spinel phase was not known. As a result, we cannot come to any firm conclusions yet regarding tetrahedral site contribution to thermopower in spinels.

Chapter 5. Thermopower as a Structural Characterization tool

In Chapter 4 the effect of structural distortions and anti-site disorder on thermopower was described. A useful application of the crystal structure thermopower relationship is to use thermopower as in *in-situ* measurement technique for determing cation distribution. This quantity, along with the spin state of the ions, is critical in determining many optical, electrical and magnetic properties in a material and results from energetic considerations of ionic size, charge of the cations and crystal field stabilization energy. Though it is an important quantity, it is also notoriously difficult to measure experimentally. For example, X-ray diffraction patterns can be refined to determine site occupancy for atoms, but atomic scattering factors for elements with a small difference in atomic number are very similar and greater contrast is needed. Neutron diffraction doesn't involve the electron cloud so scattering lengths are more random, but certain pairs of atom will still have too little contrast for differentiation.

Still more complicated are compounds featuring only different oxidation states of the same element. For instance, the iron (II, III) and cobalt (II, III) oxides, Fe_3O_4 and Co_3O_4 are amongst the most studied group of the 2,3 spinel-type oxides. Despite similar compositions and elements, they form completely different structures in terms of cation distribution. Ideally, at low temperature Co_3O_4 possesses a normal spinel-type structure $(Co^{2+})^{A}[Co^{3+}]^{B}{}_2O_4$ with Co^{2+} (S=3/2) and low-spin (LS) Co^{3+} (S=0) cations on the

tetrahedral A and octahedral B sites, respectively. On the other hand, Fe_3O_4, is an inverse spinel $(Fe^{3+})^{A}[Fe^{2+}Fe^{3+}]^{B}O_4$ with Fe^{3+} and Fe^{2+}/Fe^{3+} cations on the tetrahedral A and octahedral B sites, respectively. In practice, however, the cation distribution over the tetrahedral and octahedral sites strongly depends on the specimen history, including synthesis conditions, calcination/annealing temperature and heating and cooling rates. In addition, the degree of cation inter-mixing between the tetrahedral and octahedral sites increases with increasing temperature, making the correlation between the oxide structure and properties, particularly thermopower, highly dependent on the experimental conditions.

The difficulty in directly measuring the cation distribution in spinels has led some to calculate the distribution using thermodynamic models. In this approach thermochemical and phase equilibrium data such as phase transformation temperatures, enthalpies of formations etc. are collected for pure elements and then Gibbs energy expressions based on entropic, magnetic or other interactions are best fit to the thermochemical data. Using these expressions the phase diagram, structure, heat capacity and composition of binary, tertiary and even more complex compounds can be calculated. Chen et al.,[205] for example, use such a thermodynamic assessment to estimate the cation distribution for the difficult to measure compound Co_3O_4 described in the previous paragraph. Chen et al. did not consider the possibility that the octahedral Co^{3+} ions transitioned from a LS to a HS state. This assumption may not be valid and will be

important when comparing thermodynamically calculated cation distributions to thermopower measured cation distributions later in the chapter.

In this chapter I will describe how thermopower is used as a structural characterization tool to determine cation distribution. The original model, proposed by Wu and Mason[206] will be analyzed and alternate models will be proposed and evaluated using Co_3O_4 as a case study. Thermopower analysis will be complimented by X-ray and neutron diffraction, Raman scattering and TGA/DTA techniques. At the end of this chapter I will briefly describe future work and a few other possible characterization techniques.

5.1 Thermopower Measurement of Cation Distribution

Wu and Mason [206] were the first to use thermopower measurements to determine the cation distribution in spinels. The basic principle is that, for small-polaron conductors, the thermopower depends on the fraction of conducting sites as described in Section 2.3. This is quantified by the Heikes formula

$$S = \frac{k_B}{q} \ln\left(\beta \frac{y}{1-y} \right). \qquad 5.1$$

When this approach was first introduced in 1981 the real innovation was recognizing that one oxidation state in particular acts as a dopant, donating or accepting an electron, fixing it, therefore, to the fraction of conducting sites in the Heikes formula. In their seminal paper on the subject, Wu and Mason used thermopower measurements of magnetite,

Fe_3O_4, to argue that the structure goes from inverse at low temperatures to a disordered spinel at high temperatures.

The Wu and Mason model makes two important assumptions. The first was that the thermopower and electrical conductivity of the spinel oxides originates solely from the ions occupying the octahedral B site. The second assumption was that the orbital degeneracy term is unity, as a result of a Jahn-Teller distortion and the subsequent formation of a Kramers doublet, leaving only a spin degeneracy term.[207] However, subsequently, several authors [208–210] have reported they were unable to explain their experimental results on other oxides using these assumptions. In fact, instead of calculating the degeneracy term, β, outright, it has commonly been used as a variable, fitting parameter, ranging between 1 and 2. Non-integer values have been justified by ignoring the vibrational entropy term associated with ions surrounding the polaron site.[207] One report [209] even showed that the value would have to change from $\beta=1$ at low carrier concentrations to $\beta=2$ at high concentrations to fit their data.

As I described in Section 2.3, Koshibae et al. proposed a modified version of the Heikes formula in 2000 for strongly-correlated systems accounting for thermopower arising from spin and orbital degeneracy as well as the degeneracy ratio between conducting sites.[111] Despite the success of Koshibae et al's modified Heikes formula there remain two outstanding issues regarding thermopower measurements of cation distribution in spinels: (i) incorporating the ratio of spin and orbital degeneracy terms for

each ion, and (ii) accounting for the thermopower contributions from ions on both tetrahedral A and octahedral B sites in the spinel structure, ie in the mixed spinels.

5.1.1 Revisiting Thermopower Measurement of Cation Distributions

To address these issues, we have investigated the temperature dependence of the thermopower of Co_3O_4 and calculated the cation distributions at different temperatures by applying four different variations of the model to examine the role of tetrahedral vs octahedral site contributions, electron degeneracy terms and change in spin states. The results of these calculations will be compared with cation distributions calculated from equilibrium free energy thermodynamic arguments by Chen et al [205] as well as from a bond length and ionic radius argument.

Cobalt oxide, Co_3O_4, is a particularly suitable compound for evaluating the veracity of the different models because the cation distribution in Co_3O_4 is strongly dependent on temperature. Furthermore, as will be discussed in detail in the next section, heat capacity and lattice parameter measurements suggest there is a high temperature structural anomaly. A consensus has not yet been reached as to whether this high temperature behavior is due to anti-site disorder (inversion), a possible spin-state transition (1000-1200 K [211]) or some combination of both. Because of the incipient decomposition of Co_3O_4 to rock-salt type CoO (1165-1270 K [212]) we have applied a variety of characterization techniques as a function of temperature to monitor the phase and structure evolution from room temperature up to almost 1200 K and these results will

be presented in the next section prior to analyzing thermopower models for cation distribution.

5.1.2 Investigating High Temperature Anomaly in Co_3O_4

According to the calculated binary Co-O phase diagrams, [213,214] Co_3O_4 decomposes at elevated temperatures to first CoO and then to Co. The region of Co_3O_4 stability depends strongly on oxygen partial pressure as well as the size of Co_3O_4 crystallites and their surface hydroxylation, shifting to higher temperatures with decreasing crystallite size and increasing oxygen partial pressure. Bulk Co_3O_4 decomposes to CoO at 1242 and 909 K at $p(O_2)=1$ and 10^{-6} bar, respectively. [213,214] There are two studies that report significantly lower temperatures. Results of an *in-situ* heating Infrared Emission Spectroscopy [215] have indicated the disorder of the spinel structure begins at 873K and its conversion to the rock-salt CoO occurs at 923 K. There is also a high temperature X-ray diffraction study that reports that the transformation of Co_3O_4 to a disordered spinel occurs at 1150 K. [216]

Our initial attempts to produce dense sample of Co_3O_4 by sintering resulted in a mixture of spinel Co_3O_4 and rock-salt CoO. To find the optimum conditions to produce phase-pure Co_3O_4, we varied the sintering conditions and different heating and cooling rates. We found that dense samples of phase-pure spinel Co_3O_4 could be reproducibly prepared by sintering at 1148 K and then slowly cooling at 1K/min. CoO was produced if, instead of cooling slowly, the samples were quenched from 1148 K. These results are

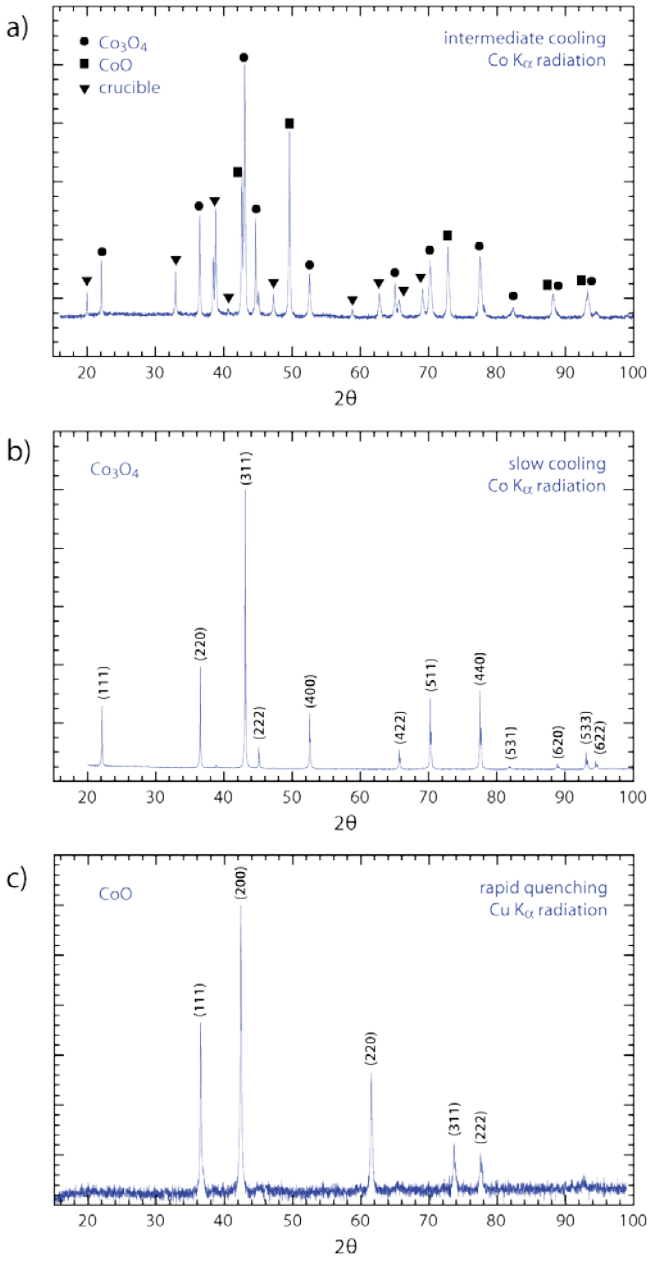

Figure 5.1. X-Ray diffraction for mixed phase Co_3O_4 and CoO samples obtained by intermediate cooling rates (a), pure Co_3O_4 obtained by slow cooling rates (b) and pure CoO obtained by rapid quenching (c). The poor signal-to-noise ratio for CoO is due to fluorescence from using Cu K_α radiation.

summarized in Figure 5.1 (a)- mixture Co_3O_4 and CoO after 1373 K sintering, (b)- Co_3O_4, (c)- CoO.

Additional information concerning the phase stability of spinel Co_3O_4 was obtained by thermal analysis, high temperature XRD and Raman microscopy. The thermal analysis data indicates that Co_3O_4 decomposition in air starts at about 1165 K and is completed at about 1270 K (see Figure 5.2). The observed weight loss of 6.42% corresponds well to the theoretical weight loss of 6.64% for the decomposition:

$$Co_3O_4 \rightarrow 3CoO + 1/2\, O_2 \qquad 5.2$$

In an argon atmosphere, the Co_3O_4 decomposition starts at a lower temperature, i.e. at about 1084 K, and is completed by about 1200 K with the same weight loss. Upon slow cooling, the increase in the specimen weight is observed at T < 990 K, which could be explained through the incomplete oxidation of CoO to Co_3O_4 by some oxygen residuals.

The results of the XRD characterization agree very well with the results of the thermal analysis. According to analysis of the X-ray diffraction patterns, the spinel Co_3O_4 remains phase-pure from room temperature up to 1163 K upon heating in air (Figure 5.3). A non-linear increase of the lattice parameter (Table 5, Figure 5.4) above 900 K was observed in agreement with reports by others [216] who attributed this phenomenon to the onset of a change in spin state that will be described later.

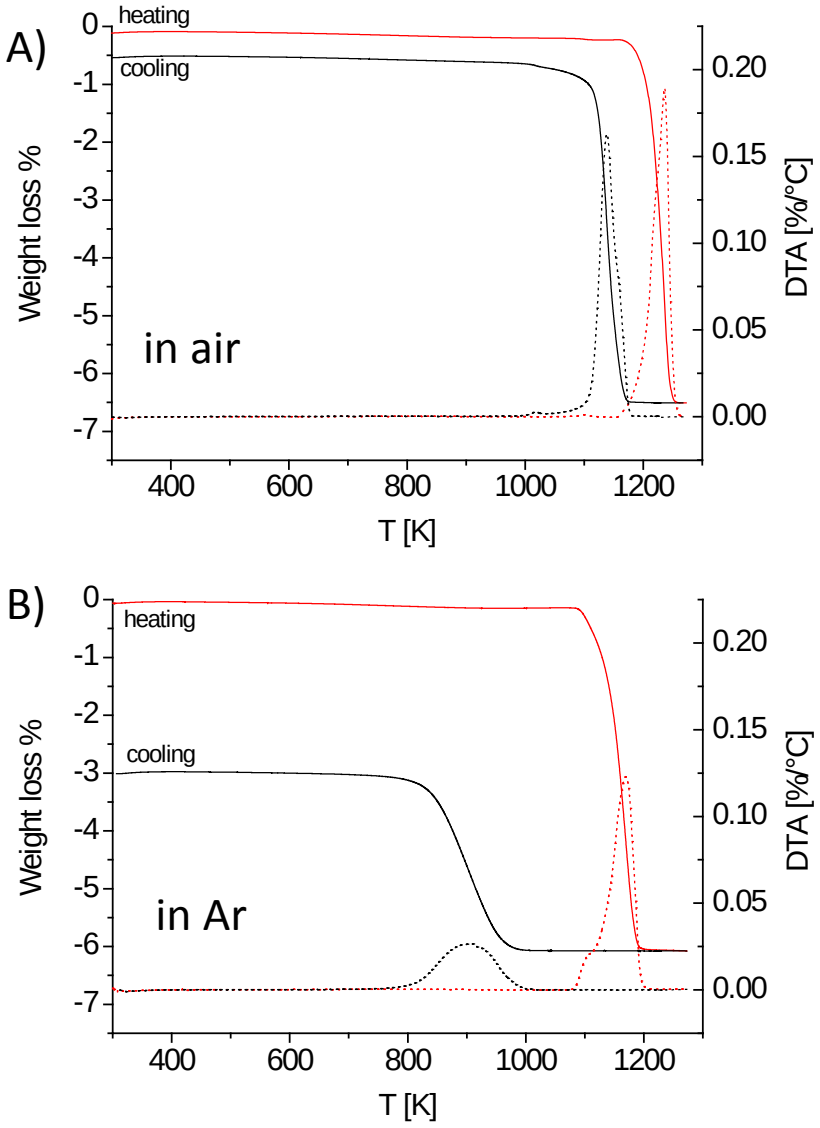

Figure 5.2. Thermogravimetric analysis and differential thermal analysis of Co_3O_4 samples in air and Ar. The sample transforms to CoO at 1165 K in air and 1084 K in Ar. In both cases the oxygen weight loss corresponds very closely with the predicted amount and, unexpectedly, the sample in Ar gained back a portion of the weight suggesting the chamber retained some residual oxygen.

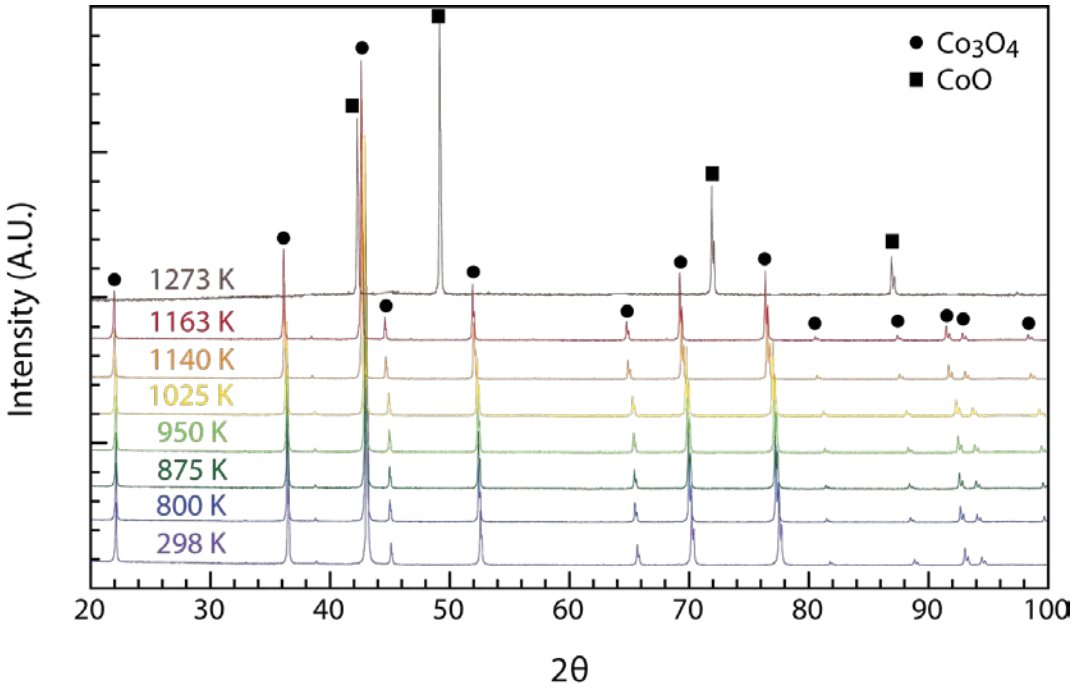

Figure 5.3. X-Ray diffraction of Co_3O_4 from room temperature up to 1273 K. The sample converts entirely to CoO between the scan at 1163 K and 1273 K.

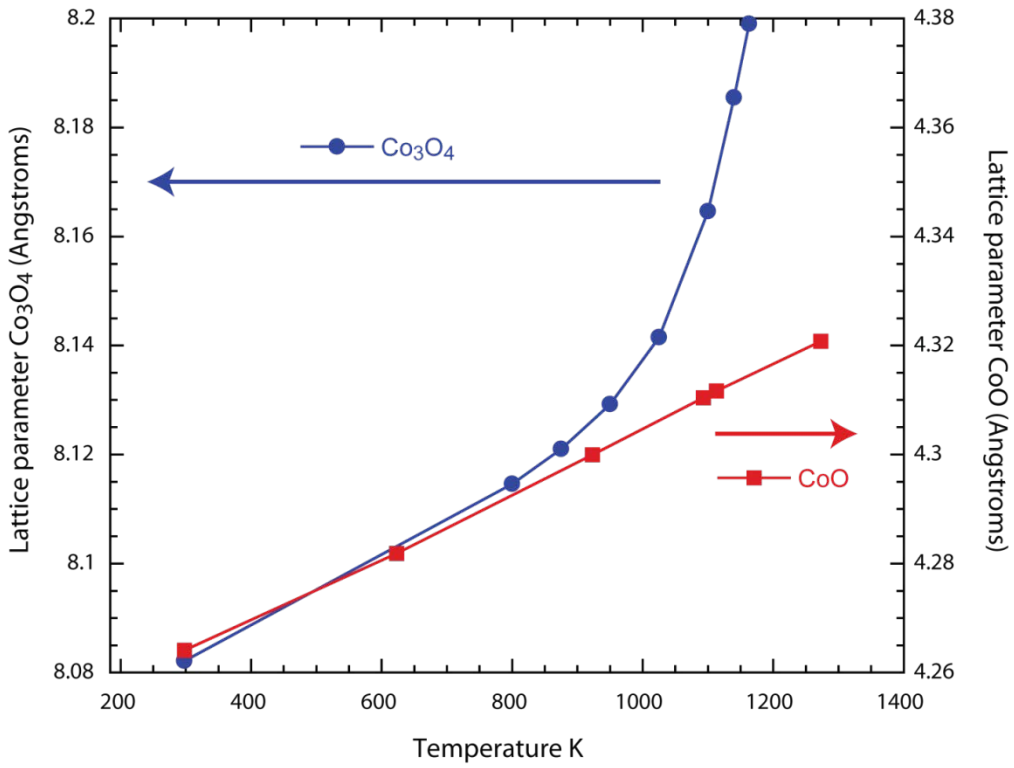

Figure 5.4. Temperature dependence of the lattice parameter of Co_3O_4 (left-hand side y axis) and CoO (right-hand side y axis) determined from in-situ XRD. The scale of both y-axes are the same, but whereas the CoO lattice parameter increases linearly through all temperatures the Co_3O_4 lattice parameter rapidly increased above 900 K.

At 1273 K Co_3O_4 had completely decomposed to the rock-salt structured CoO (see Figure 5.3). This decomposition was reversible: upon cooling in air the CoO oxidized back to phase-pure spinel Co_3O_4. The results of the quantitative Rietveld analysis results for phase fraction, lattice parameter and oxygen fractional parameter, u, are recorded in Table 5. Specimens quenched to retain the rock-salt CoO phase remain

Table 5. Structure refinement details for Co_3O_4 as a function of temperature (standard deviations in shift shown beneath in parenthesis)

Temp K	Wt% Co_3O_4	Wt% CoO	a Co_3O_4	u Co_3O_4	a CoO	R_{wp}
298	100	-	8.0821 (2)	0.2349 (1)	-	2.95%
800	100	-	8.1146 (3)	0.2351 (1)	-	2.53%
875	100	-	8.1210 (2)	0.2353 (1)	-	2.56%
950	100	-	8.1292 (2)	0.2354 (1)	-	2.55%
1025	100	-	8.1415 (3)	0.2357 (1)	-	2.71%
1100	100	-	8.1646 (2)	0.2359 (1)	-	2.53%
1140	100	-	8.1855 (3)	0.2365 (1)	-	2.50%
1163	100	-	8.1999 (3)	0.2368 (1)	-	2.46%
1273	-	100	-	-	4.3207	3.79%
298	100	-	8.0818 (3)	0.2348 (1)	-	2.88%

stable in air on heating from room temperature until 950-1188 K, when they are oxidized to Co_3O_4, and then above 1188 K Co_3O_4 again decomposes reversibly to 100 wt% CoO.

The results of the Raman spectroscopy (Figure 5.5) are also consistent with the high-temperature XRD phase determination providing additional information about the microstructure of the specimens. The Co_3O_4 exhibit four Raman active modes: A_{1g} (689 cm^{-1}), F_{2g} (619 and 521 cm^{-1}) and E_g (481 cm^{-1}).[217] The high frequency A_{1g} mode is due to vibrational mode of octahedral cations, whereas E_g and F_{2g} modes are determined by both tetrahedral and octahedral cations. With increasing temperature on heating from

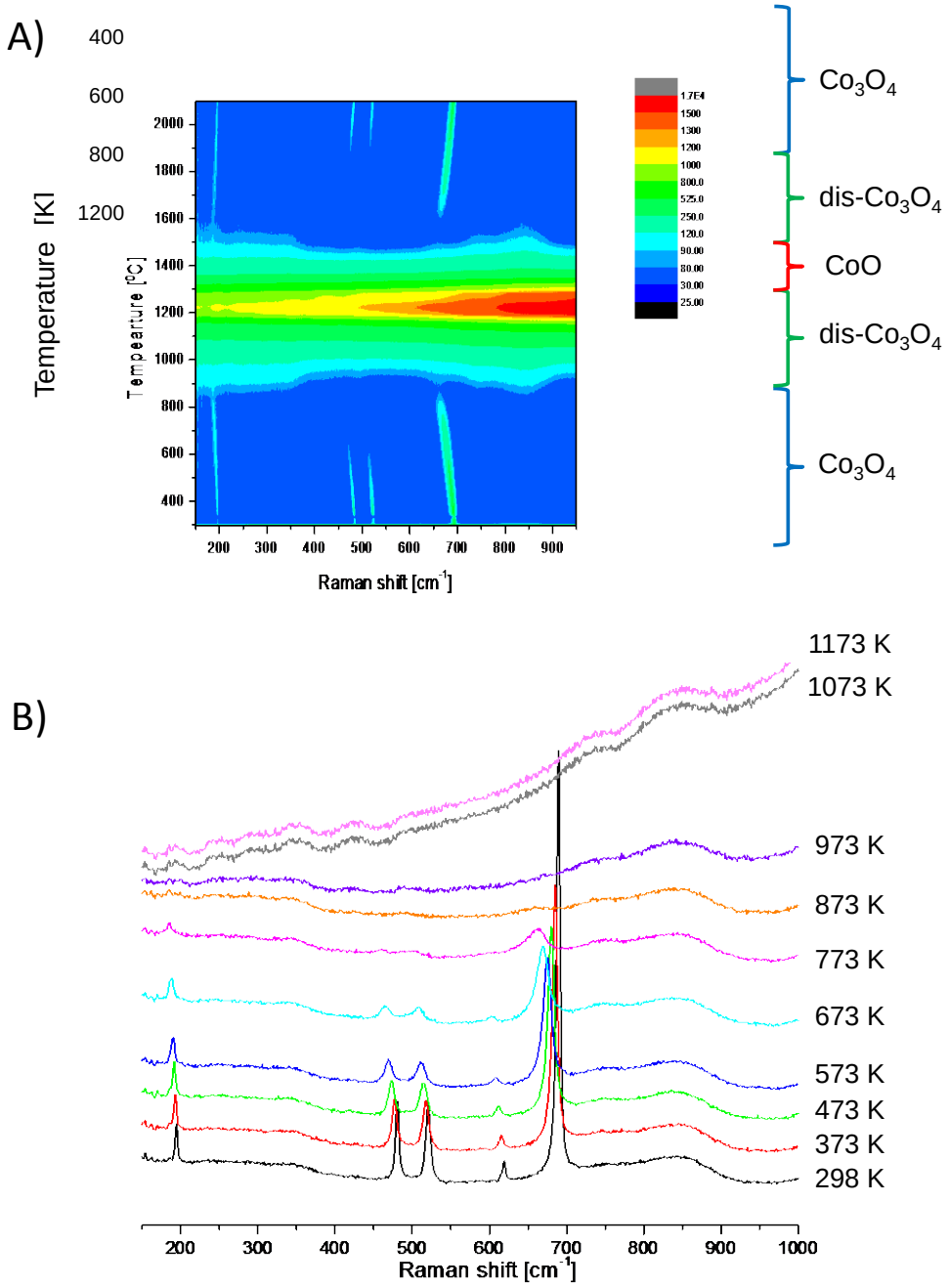

Figure 5.5. Raman shift plotted as a function of temperature for Co_3O_4 samples. The five peaks resulting from the spinel modes disappear above 800 K before transformation to CoO rock-salt which has no Raman active modes.

room temperature, the Co_3O_4 bands shifts towards lower energies and broaden, consistent with thermal expansion. Above about 850 K the peaks undergo significant broadening indicating structural disordering since cobalt ions in different oxidation/spin states possess a different Raman response due to a difference in length and covalency of Co-O bonds. The spinel structure transforms above 1100-1200 K, decomposing to rock-salt CoO, a NaCl type crystal having no first-order Raman active modes. Despite this, several reports [218–220] observe peaks at 475, 515, 555, 600 and 680 cm^{-1} yet, in our study, even at the highest temperatures these peaks are not observed. These processes are reversible (in air) and the temperature range of hysteresis is the same as observed by X-ray diffraction.

Electrical conductivity measurements as a function of temperature (Figure 5.6) reveal three characteristic conductivity regimes with an activation energy of 0.35±.08 eV (418-540 K), 0.15±.05 eV (540-890 K) and 2.28±.06 eV (890-1188 K). These are attributed to the ionization, extrinsic and intrinsic conduction regimes, respectively, in reasonable agreement with the reported hopping energy value 0.17 eV and optical absorption transition ($O^{2-} \rightarrow Co^{2+}$) of 2.14 eV.[221] We believe it is significant that the temperature ranges corresponding to different conduction mechanisms are in good agreement to the thermopower temperature regimes as well as structural changes monitored by Raman spectroscopy. The measurements of the conductivity in the CoO phase give an activation energy of 0.47±.02 eV.

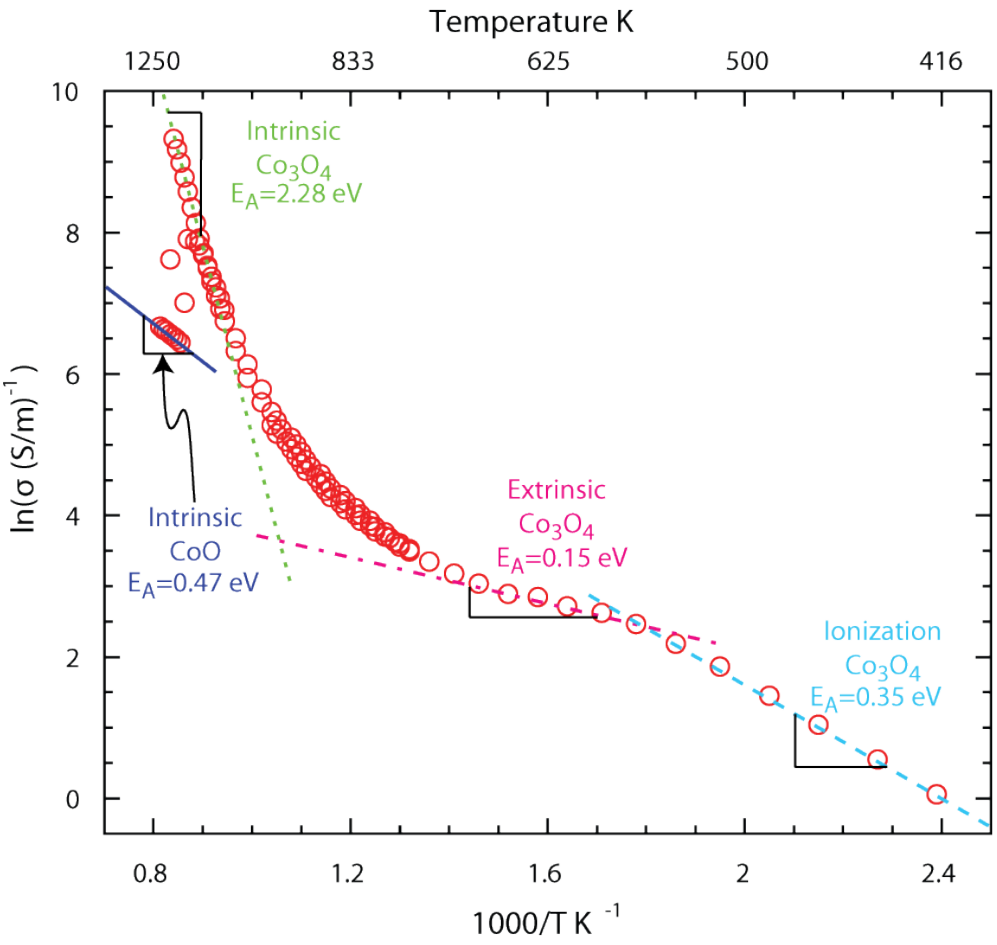

Figure 5.6. Arrhenius plot of electrical conductivity for Co_3O_4 showing three characteristic regions each with a different activation energy. Above 1188 K Co_3O_4 decomposes to CoO, a band conductor.

The Seebeck coefficient of Co_3O_4 as a function of temperature (measured in air and helium) is shown in Figure 5.7 together with that of CoO (measured in helium only). A key feature of the graph is that the spinel Co_3O_4 samples measured in air and helium both have a maximum in thermopower of ~600 μV/K around 850 K. Above this temperature, the thermopower decreases almost linearly with increasing temperature until it abruptly increases with a slope of ~250 μV/K in air and ~400 μV/K in helium. The

region of approximately linear decrease correlates to inversion of the spinel structure as will be discussed in the next section. The discontinuity in thermopower (1188 K in air

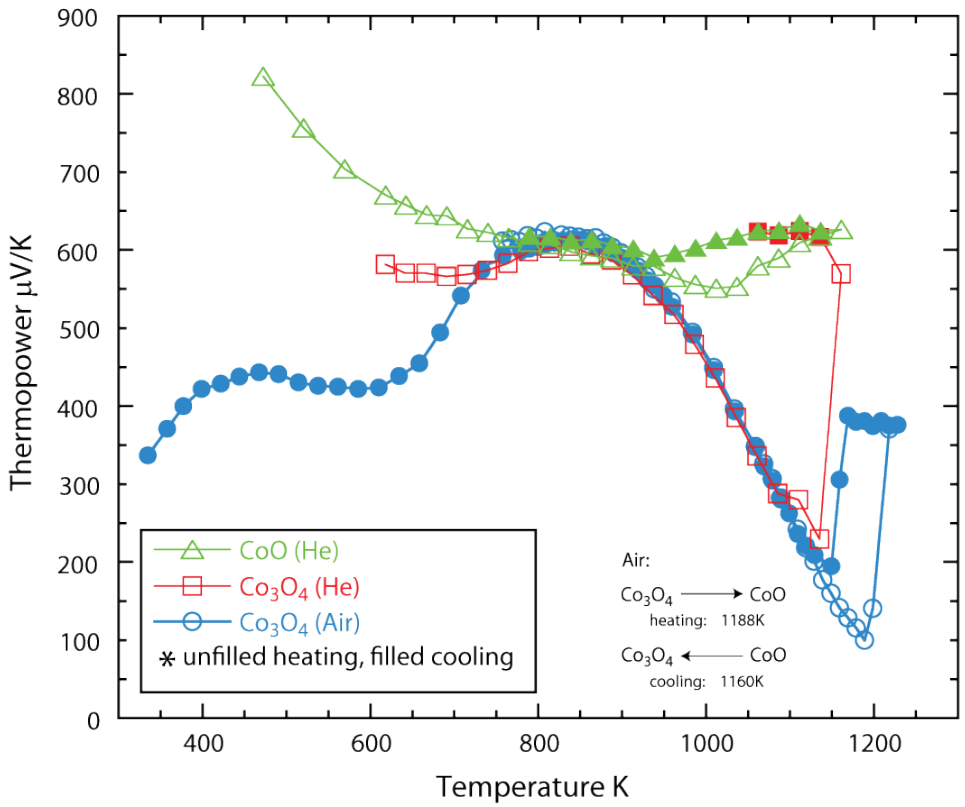

Figure 5.7. Thermopower as a function of temperature of Co_3O_4 measured in helium (squares) and air (circles) as well as of CoO measured in helium (triangles). Heating (unfilled) and cooling (filled) of the samples is indicated. For Co_3O_4, a relative maximum of ~600 µV/K is observed near 850 K before the thermopower decreases linearly with temperature until transformation to CoO. This decrease is attributed to inversion of the spinel structure. In the range 900-1100 K the CoO sample likely begins to transform to Co_3O_4 due to residual oxygen in the chamber or by partial reduction to Co metal during the thermopower measurement before returning to the CoO phase at high temperatures.

and 1150 K in He) is attributed to the decomposition of the spinel Co_3O_4 to rock-salt CoO as indicated by both high-temperature XRD and Raman observations reported earlier.

In Co_3O_4 with the normal spinel-type structure, positive thermopower at low temperature suggests hole hopping conduction dominates and at high temperature a decreasing thermopower indicates that electron hopping (with much higher mobility) contributes to the conductivity.[222]

5.1.3 Effect of Inversion on Co_3O_4 structure

At low temperatures the octahedral sites in Co_3O_4 are occupied almost entirely by Co^{3+} ions, consistent with the normal spinel structure. Neutron diffraction [223] and magnetic susceptibility measurements [224] suggest that the d^6 electrons from Co^{3+} pair up to completely fill the octahedral t_{2g} triplet whereas the d^7 electrons from Co^{2+} on the tetrahedral site leave 3 unpaired electrons on t_{2g} orbitals that account for the observed magnetic moment of 3.25 μ_B.

These structural findings have been attributed to two main effects. The first is a disordering of the spinel structure leading to a partial occupation of tetrahedral sites by Co^{3+} and octahedral sites by Co^{2+}. The consequence of this being that electron exchange (hopping) can occur between octahedral Co^{2+} and Co^{3+} ions, resulting in increased conductivity in this temperature region. Effectively, this is equivalent to an electron transfer from Co^{2+} to Co^{3+} (hopping) which is also involved in the explanation of transport properties (electrical conductivity and thermopower):

$$Co_A^{2+} (e_g^4 t_{2g}^3) + Co_B^{3+} (LS, t_{2g}^6 e_g^0) \leftrightarrow Co_A^{3+} (LS, e_g^4 t_{2g}^2) + Co_B^{2+} (LS, t_{2g}^6 e_g^1) \quad 5.3$$

The effective change of the lattice parameter due to the reaction in Equation 5.3 is not obvious and required detailed calculation which will be performed below. The question arises also about the spin state of Co^{2+}/Co^{3+} on tetrahedral and octahedral sites.

The second effect that could, in part, explain our structural findings is an unpairing of the electron spins of the octahedral Co^{3+} ions: [225]

$$Co_B^{3+} (LS, t_{2g}^6 e_g^0, S=0) \rightarrow Co_B^{3+} (HS, t_{2g}^4 e_g^2, S=2) \quad 5.4$$

with possible formation of an intermediate state, IS- Co_B^{3+}, with $t_{2g}^5 e_g^1$, S=1.[221]

The HS and IS Co_B^{3+} ions have a larger ionic radius compared to that of LS Co_B^{3+}. The result is an increase in the lattice parameter as well as in the thermal expansion coefficients if LS Co_B^{3+} transition to IS or HS states. The influence on thermopower and electrical conductivity require detailed analysis which will be described below. Due to the partially filled e_g level, the IS state is Jahn-Teller active, creating distortions of (CoO_6) octahedral (see Figure 4.2), associated with lattice distortion and broadening of Raman bands. [221]

As the result of simultaneous lattice disordering and spin unpairing, it is likely that the tetrahedral sites will be occupied by both Co^{2+} ($e_g^4 t_{2g}^3$) and Co^{3+} ($e_g^4 t_{2g}^2$) cations, whereas the octahedral sites will be occupied by LS Co^{2+} (LS, $t_{2g}^6 e_g^1$), and Co^{3+} (d^6) in

different spin states. Furthermore, as disordering begins at the lower temperatures, it is most probable that the spin state changes from LS ($t_{2g}^6 e_g^0$), to HS ($t_{2g}^4 e_g^2$) at the highest temperature (Table 6). Consequently, several possible charge transfer (hopping) processes need to be considered in the calculation of cation distributions from the thermopower measurements. This will be discussed in the next section.

Table 6. Possible occupation of tetrahedral and octahedral sites in spinel-type Co_3O_4 at elevated temperatures due to the inversion (anti-site disorder) and spin unpairing (LS⇄ HS) processes and the corresponding electronic degeneracies ($g = g_{spin}\, g_{orbital}$).

	tetrahedral sites		octahedral sites			
	Co^{2+} HS	Co^{3+} HS	Co^{2+} LS	Co^{2+} HS	Co^{3+} LS	Co^{3+} HS
spin diagrams and degeneracy	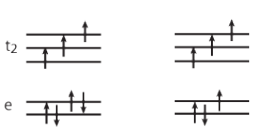		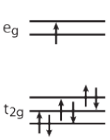	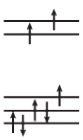		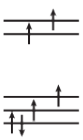
	S = 3/2 Γ = 1 g = 4	S = 2 Γ = 2 g = 10	S = 1/2 Γ = 2 g = 4	S = 3/2 Γ = 3 g = 12	S = 0 Γ = 1 g = 1	S = 2 Γ = 3 g = 15
inversion	Co^{2+} LS & Co^{3+} HS $g_e/g_h = 4/10$		Co^{2+} LS & Co^{3+} LS $g_e/g_h = 4/1$			
spin unpairing	--		--			
inversion and spin unpairing	Co^{2+} LS & Co^{3+} HS $g_e/g_h = 4/10$		Co^{2+} LS & Co^{3+} LS $g_e/g_h = 4/1$ Co^{2+} HS & Co^{3+} LS $g_e/g_h = 12/1$ Co^{2+} LS & Co^{3+} HS $g_e/g_h = 4/15$ Co^{2+} HS & Co^{3+} HS $g_e/g_h = 12/15$			

5.2 Alternate Thermopower Cation Distribution Models

As discussed above, we aim to explain the behavior of the Co_3O_4 thermopower at elevated temperatures through the distribution of Co^{2+}/Co^{3+} cations in different spin states over the tetrahedral and octahedral sites in the spinel-type Co_3O_4.

Initially, we ignore possible spin unpairing transition and argue through thermopower measurements made on Co_3O_4 sample measured in air (circles, Figure 5.7) that Co_3O_4 changes from a normal spinel below 850 K to a disordered spinel, $\left[Co_O^{3+}\right]$ =0.64, (complete disorder would be 2/3 ≈ 0.67) at the highest temperature before the onset of the spinel to rock-salt transformation. The gradual inversion of the structure is accompanied by transferring an electron from the B to the A site. The result is that on the octahedral site there is a mixture of low spin d^6 and d^7 electrons with the Co^{2+} ion behaving as an electron donor because of its unpaired electron occupying the e_g orbital (see Table 6). The results from these calculations will be compared to the predicted cation distribution in Co_3O_4 based on a thermodynamic assessment of the Co-O system [205] as well as the distribution based on cation radius and bond length described in detail later.

5.2.1 Cation Distribution from Thermopower Measurements: Inversion Only

In discussing the relationship between thermopower measurements and the cation distribution, we consider three cases of increasing sophistication:

(i) The original model proposed by Wu and Mason,[206] in which only hopping between the ions on the B sites occurs and β is arbitrarily selected to be 2,

(ii) again, B site contributions only but including Koshibae et al.'s [111] treatment with both orbital and spin degeneracy ratio for Co^{2+} and Co^{3+},

*(iii)*contributions to the thermopower from ions on both A and B sites calculated using Koshibae et al.'s expression.

Case (i). According to Wu and Mason's model, the thermopower for small-polaron octahedral hopping mechanism, S_O, is give by Equation 5.1 where *y* is the concentration $\left[Co_O^{3+}\right]$. Combining the spin degeneracy, *2S+1*, and orbital degeneracy, 2, the degeneracy term of this electron donor should have the value of β = 2*(2*1/2+1) = 4. However, as will be explained in discussing *case (ii),* a value of β=4 produces inconsistent results for the cation distribution. If we treat β as a fitting parameter, as some previous authors have done, and select its value arbitrarily to be 2, then there is closer agreement to Chen et al.'s calculations, as shown in Figure 5.8. Such an assignment would be reasonable if there were a Jahn-Teller distortion of the B site since the orbital degeneracy of the e_g levels would be lifted and the resulting degeneracy would, in fact, be 2. However, there is no evidence of such a Jahn-Teller distortion either in our own XRD results or in the literature so the β=2 assignment appears to have no physical basis. It is also appropriate to mention that the distribution determined by Chen et al. using free energy arguments assumes equilibrium conditions but our samples might not have been able to reach perfect equilibrium at every temperature for thermopower measurements.

Therefore, the low temperature deviation could be the result of kinetically limited anti-site disorder. At higher temperatures the thermopower determined distribution and the thermodynamically calculated distribution are in closer agreement, including the point of inflection.

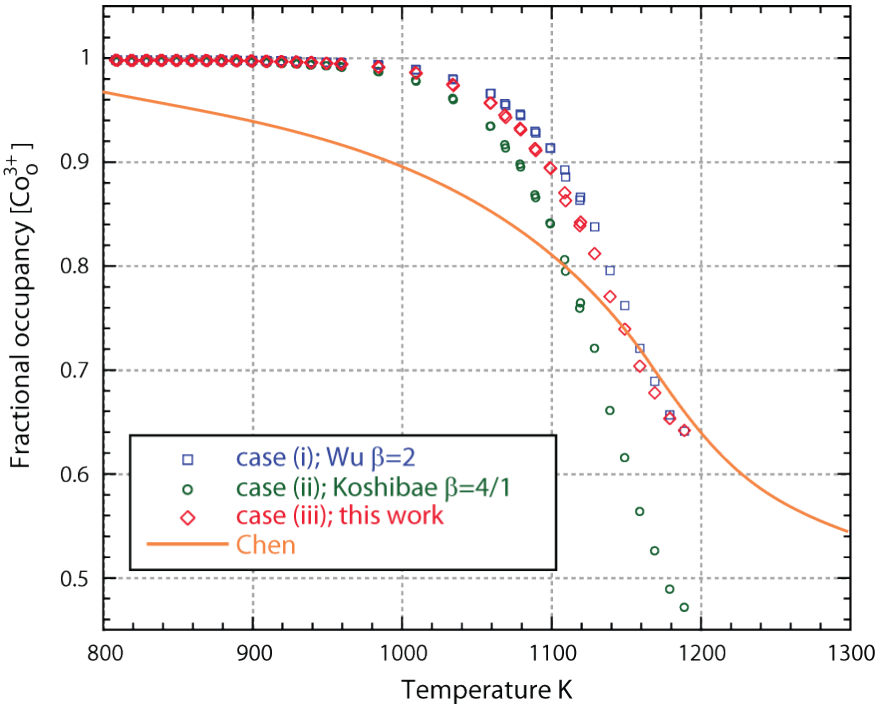

Figure 5.8. Fractional occupancy of Co^{3+} ions on the octahedral sublattice in Co_3O_4 as a function of temperature calculated from the thermopower measurements of Co_3O_4 in air according to case (i) (squares), case (ii) (circles) and case (iii) (diamonds) described in detail in the text. The solid line is the distribution calculated thermodynamically from free energies according to the procedure given by Chen et al.[205] Good agreement with Chen et al.'s prediction was found for case (iii), proposed in this work with no variable parameters. Case (i) also had good agreement, but only when an unphysical value of 2 was selected for β.

Case (ii). Following Koshibae et al.'s treatment, the spin and orbital degeneracy of both octahedral Co^{2+} and Co^{3+} ions are needed to calculate the thermopower. The Co^{2+} ion degeneracy is the same as in *case (i)*, 4. The Co^{3+} d^6 electrons are low spin and fully occupy the t_{2g} orbital so the degeneracy is 1*(2*0+1)=1 and the degeneracy term β is 4/1. The thermopower expression is the same as Equation 5.1. This distribution result is not stoichiometrically consistent though because it requires more Co^{2+} ions on the octahedral site than are initially present in the formula unit; the $\left[Co_O^{2+}\right]$ fraction cannot be larger than ½ without introducing oxygen vacancies. A nearly stoichiometric composition with minimal oxygen vacancies is a good approximation for Co_3O_4 because the Seebeck coefficient and electrical conductivity in Co_3O_4 do not depend on oxygen partial pressure (P_{O_2}). [222] Furthermore, thermal analysis data do not show any weight loss below ~ 1100 K in Ar and the oxygen loss at the CoO transformation agrees very well with the assumption of a stoichiometric composition.

At the highest temperature measured, before decomposition to the rock-salt CoO occurs, the fraction of $\left[Co_O^{2+}\right]$ calculated from thermopower according to *case (ii)* was already slightly greater than ½ (see Figure 5.9) and it's possible, even likely, that the decomposition from Co_3O_4 to CoO occurs before inversion in Co_3O_4 is complete. Interestingly, Mocala et al., using heat capacity measurements at different oxygen partial pressures, demonstrated an ability to shift the spinel to rock-salt transformation temperature.[211] They found that in air the transformation took place at 1180 K whereas at 1 bar of oxygen it had increased to 1240 K. Furthermore, Mocala et al. calculates that in

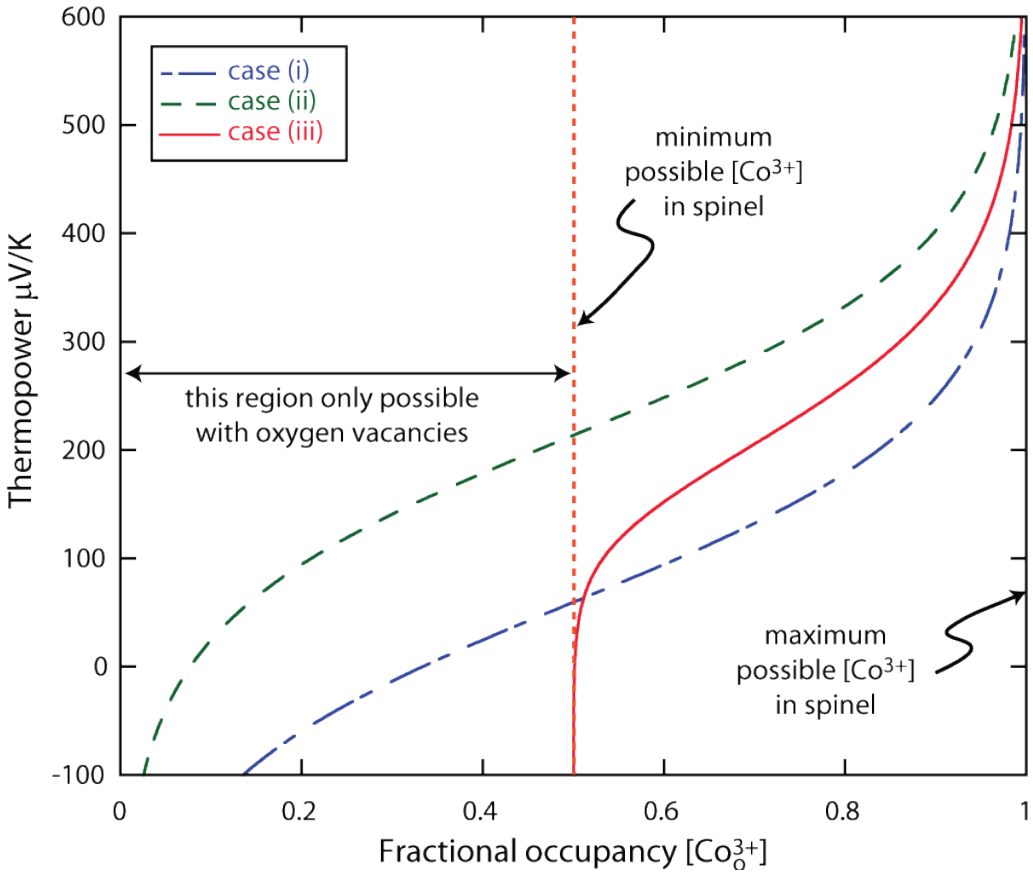

Figure 5.9. Thermopower plotted against fractional occupancy of Co^{3+} ions on the octahedral sub-lattice according to cases (i), (ii) and (iii) described in detail in the text. The vertical dotted line represents the minimum possible value for $\left[Co_O^{3+}\right]$ in Co_3O_4. As thermopower decreases due to inversion both cases (i) and (ii) approach the limit of $\left[Co_O^{3+}\right]=0$, in violation of stoichiometry in the spinel structure, but case (iii) remains consistent.

20 bars of oxygen, the transformation would increase up to 1350 K. Because our values of the thermopower decreased linearly with increasing temperature up until the abrupt transformation to rock-salt CoO, we consider it highly probable that the thermopower would continue to decrease further if larger oxygen pressures can suppress the

transformation. Then, both *case (i)* and *case (ii),* based on the thermopower contribution from the B site only using Wu et al.'s and Koshibae et al.'s models, respectively, would be stoichiometrically inconsistent. This finding, shown in Figure 5.9, is perhaps the most significant in the entire chapter because it provides evidence that Wu et al.'s original model requires review for Co_3O_4 and possibly other spinels.

Case (iii). In this third case, we consider the thermopower contributions from both A and B sites in the spinels using Koshibae et al.'s thermopower expression. An earlier analysis by Dieckmann et al. [226] also considered octahedral, tetrahedral and octahedral-tetrahedral small-polaron hopping in magnetite, but did so using Heikes' original thermopower expression with Wu et al's $\beta=2$.

As described in *case (i)*, inversion creates electron donors on the octahedral site. Interestingly, as suggested by Koumoto and Yanagida, [222] it is also possible that inversion simultaneously hole dopes the tetrahedral site. Tetrahedral Co^{2+} ions are high spin with 3 unpaired electrons in the t_{2g} triplet, but tetrahedral Co^{3+} ions have only 2 unpaired electrons in the t_{2g} triplet. The contribution to thermopower from multiple, parallel conduction mechanisms, octahedral and tetrahedral hopping, is calculated according to a weighted fraction of the electrical conductivity of each mechanism as follows [226]

$$S_{total} = \frac{\sigma_O S_O + \sigma_T S_T}{\sigma_{total}} \qquad 5.5$$

where σ_O, σ_T, S_O and S_T, are the contributions to electrical conductivity and thermopower from octahedral and tetrahedral hopping, respectively.

To proceed we need to evaluate the electrical conductivity on each sub-lattice. Let us take Fe_3O_4 (magnetite) case. The results of Mössbauer spectroscopy of Fe_3O_4 at low temperatures have been attributed to electron hopping along the octahedral sub-lattice.[227] A later detailed analysis by Dieckmann et al. [226] separated octahedral sub-lattice hopping contributions to electrical conductivity from other mechanisms and found that octahedral hopping dominated conduction, but significant tetrahedral or octahedral-tetrahedral conduction exists at high temperatures. We attempted a similar analysis for Co_3O_4 , but is not straight forward because Co_3O_4, unlike Fe_3O_4, which is a half-metal, is a large band-gap semiconductor and the onset of thermally activated carriers masks the contribution of tetrahedral and octahedral-tetrahedral hopping mechanisms at high temperatures. Furthermore, analysis at higher temperatures is not possible because of the intervention of the decomposition of Co_3O_4 to CoO.

Nevertheless, consider, for the sake of qualitative argument that at high temperatures significant conduction occurs via the hole-doped tetrahedral sub-lattice in addition to the electron doped octahedral sub-lattice. If we assume that conduction is proportional to the site fraction such that 1/3 of the conduction occurs via tetrahedral conduction and 2/3 via octahedral conduction, then we can use Equation 5.5 to express the total thermopower as:

$$S_{total} = \tfrac{2}{3} S_O + \tfrac{1}{3} S_T \qquad 5.6$$

The thermopower due to conduction on the octahedral sites would be the same as in *case (ii)* and the thermopower due to the tetrahedral sites would depend on the degeneracies of high spin Co^{2+} and Co^{3+} in tetrahedral coordination, 4 and 10 respectively. Because the carriers are now holes, instead of electrons, the sign is also changed to give

$$S_T = -\frac{k_B}{q} \ln\left(\frac{4}{10}\frac{y}{1-y}\right) \qquad 5.7$$

with *x* now being $\left[Co_T^{3+}\right]$.

When we calculate the cation distribution for *case (iii)* we can make two observations. The first is that it agrees with Chen et al.'s at least as well as *case (i)* which relied on an arbitrary β parameter. The second is that, even if the thermopower were to continue to decrease with temperature, as we predict it will for samples measured in high oxygen pressures, the inversion would remain stoichiometrically consistent because $\left[Co_O^{2+}\right]$would approach the high temperature limit of 0.5, in agreement with Chen et al.'s prediction of the site occupancies. To illustrate this important point, consider Figure 5.9 where we have plotted thermopower against $\left[Co_O^{3+}\right]$ based on each of the three cases considered here. The lowest value for thermopower measured in air on our samples was 109 μV/K and the lowest permissible thermopower values according to Koshibae et al's and Wu and Mason's models are 119 and 60 μV/K, respectively. In contrast to both of

these we see that in our model the $\left[Co_O^{2+}\right]$ fraction approaches the physically sensible limit of 0.5 even for very low thermopower values.

5.2.2 Cation Distribution from Thermopower Measurements: Inversion and Spin Unpairing

Finally, we discuss what the change in spin state could play in determining the thermopower of Co_3O_4. A key feature of Koshibae's model is that it successfully accounts for the change in spin state from low-spin (LS) to high spin (HS) of Co^{4+} ions in $NaCo_2O_4$ with increasing temperature [111] There has been extensive debate regarding the spin-state of Co^{3+} in Co_3O_4 at high temperatures. Chen et al. argue that measurements as diverse as lattice parameter,[212,216,228] EMF of oxygen potential,[212,229] and heat capacity [211] all indicate a high temperature anomaly at 1120 K, just before Co_3O_4 transforms to CoO. The general consensus is that a second-order transition from LS-HS in Co^{3+} ions takes place at this temperature. However, the effect this would have on cation distribution is still debated. Kale, for example, suggests an inverse spinel,[212] Liu and Prewitt favor a disordered spinel and Mocala et al. suggests a normal spinel with only 5-10% disorder.[216]

A change in spin-state alters the spin and orbital degeneracy and would, therefore, affect the thermopower analysis of *case (ii)* and *(iii)* in equation 2. For example, the octahedral Co^{3+} degeneracy term increases from 1 to 15 with a LS→HS transition. The cation distribution calculated according to *case (ii)* and *(iii)* assuming different spin-states for octahedral cobalt cations is shown in Figure 5.10. We note that when a Co^{3+} LS→HS transition is assumed, a stoichiometrically consistent cation distribution is obtained for

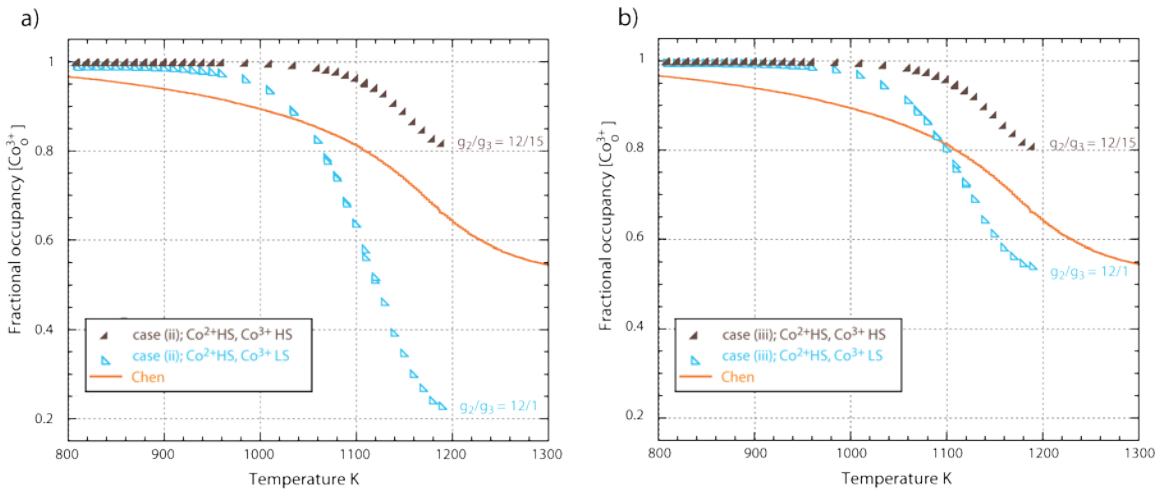

Figure 5.10. Fractional occupancy of Co^{3+} ions on the octahedral sublattice in Co_3O_4 as a function of temperature accounting for different cobalt ion spin states in case (ii) (a) and case (iii) (b). In case (iii) a fixed high spin state for Co^{2+} and Co^{3+} ions on the tetrahedral site was assumed.

case (ii). For *case (iii)* a stoichiometrically consistent cation distribution is found regardless of the spin state of Co^{3+}, but the scenario closest to Chen et al's prediction is if Co^{3+} ions remain low spin.

Figure 5.10 also shows that neither *case (ii)* nor *case (iii)* can account for the thermopower produced by a spin state transition alone; both cases show that a minimum of ~20% anti-site disorder on the B site must be present. Mocala et al. showed the anomaly in heat capacity, reportedly due to Co^{3+} LS→HS, begins at 1000 K and continues until decomposition. Figure 5.7 shows that thermopower decreases at an almost continuous rate from 900 K until transformation to CoO with no abrupt change that could be attributed to a high temperature change in spin state. For these reasons, we cannot

conclude definitively that a change in spin state occurs; it remains possible that the thermopower results solely from inversion of the Co_3O_4 structure, or by a combination of inversion and change in spin state.

5.3 Evaluating Thermopower Cation Distribution Models

Considerable clarification would be gained from *in-situ* measurements of the magnetic susceptibility and determination of the magnetic structure over the temperatures 850-1200 K. Unfortunately, such measurements have not yet been performed for Co_3O_4 though magnetic moment measurements using a vibrating sample magnetometer (VSM) are underway. In their absence, other than Chen et al.'s prediction of the ion distributions, which is limited to the assumption that no change in spin state occurs, there are very few remaining methods whereby we can compare and assess the three cases described here. In this section we describe one method to evaluate the thermopower cation distribution models. X-ray diffraction is measured independently from thermopower. This allows us to examine the bond lengths measured by XRD as a function of temperature and determine what combination of Co^{2+} and Co^{3+} ionic radii could account for the observed bond lengths.

5.3.1 Bond Lengths Calculated from Ionic Radii

The fraction of Co^{3+} on the octahedral site, $\left[Co_O^{3+}\right]$, was calculated using the bond lengths of tetrahedral and octahedral ions [216] (r_{A-O} and r_{B-O}) as well as the coefficient of thermal expansion [230] reported previously for Co_3O_4 up to high temperatures. The ionic radii [149] for Co^{2+}, Co^{3+} and O^{2-} were used at room temperature and the coefficient of

thermal expansion for Co_3O_4 was applied for non-ambient calculations. The distribution as a function of temperature (Figure 5.11) is calculated as follows

$$\left[Co_O^{3+}(T)\right]_{A-O\ bond} = 1 - \frac{\left(\frac{r_T^{Co2+}(T) - r_{A-O}(T) - r^{O2-}(T)}{r_T^{Co2+}(T) - r_T^{Co3+}(T)}\right)}{2} \qquad 5.8$$

and

$$\left[Co_O^{3+}(T)\right]_{B-O\ bond} = \left(\frac{r_O^{Co2+}(T) - r_{B-O}(T) - r^{O2-}(T)}{r_O^{Co2+}(T) - r_O^{Co3+}(T)}\right) \qquad 5.9$$

where $r_{T,O}^{Co2+}$ and $r_{T,O}^{Co3+}$ are the ionic radii for Co^{2+} or Co^{3+} in tetrahedral or octahedral coordination respectively (HS r_T^{Co2+}, LS r_O^{Co2+}, HS r_T^{Co3+}, LS r_O^{Co3+}), r_{A-O} and r_{B-O} are the tetrahedral and octahedral bond lengths respectively [216] and r^{O2-} is the ionic radius for O^{2-}. Both sets of data show the same trend in approximate agreement with the cation distribution calculated in *cases (i), (ii)* and *(iii)*; i.e. little or no inversion at lower temperatures and the onset of inversion above ~1000 K. At 1200 K the octahedral bond length data suggests complete inversion while the tetrahedral bond length data indicates a random distribution of cations ($\left[Co_O^{3+}\right]$=62%). However, due to the large variation in bond lengths, we are unable to use the bond length data and the analysis of the ionic radii to assess the accuracy of the thermopower cation distributions.

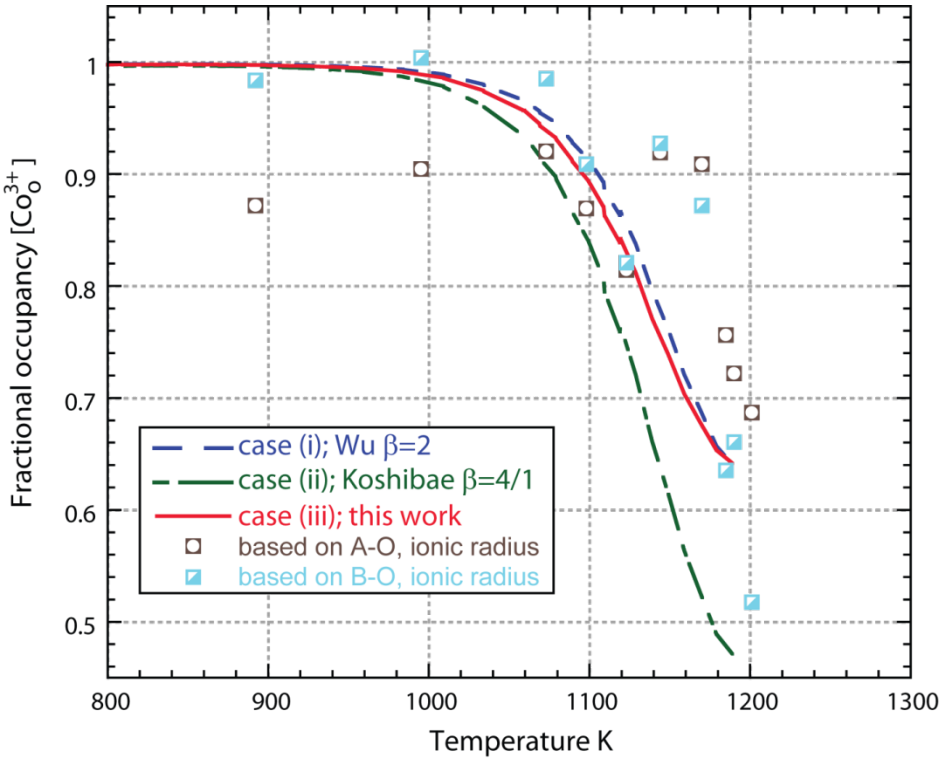

Figure 5.11. Fractional occupancy of Co^{3+} ions on the octahedral sub-lattice in Co_3O_4 as a function of temperature calculated from ionic radii and tetrahedral (brown squares with circles) and octahedral (squares with triangles) bond lengths. The cation distribution calculated from thermopower measurements according to cases (i), (ii) and (iii) are shown for comparison. The low precision in the bond length data is due to variation in the bond lengths determined by the Rietveld refinement of high temperature X-ray diffraction data.

5.4 Future Work and Conclusions

In addition the inconclusive bond lengths analysis of cation distribution there are a few other techniques and measurements that could offer insight to cation distribution and the high temperature anomaly in Co_3O_4. Measuring the magnetic moment via

vibrating sample magnetometry (VSM) could be performed *in-situ* at high temperatures or on rapidly quenched samples from a range of high temperatures in hopes that the high temperature electronic and crystal structure would be preserved. The electron binding energies of Co^{2+} and Co^{3+} ions in octahedral and tetrahedral sites are not the same so X-ray photoelectron spectroscopy (XPS) could be used to measure the kinetic energy and number of electrons from a material being irradiated by X-rays. The spectra could ideally be deconvoluted and fractional occupancy of Co^{2+} and Co^{3+} ions on octahedral and tetrahedral sites could be calculated. Synchrotron techniques such as extended X-ray absorption fine structure (EXAFS) or X-ray magnetic circular dichroism (XMCD) could also potentially be performed *in-situ* on samples. An especially promising technique is to rapidly quench samples and then to perform neutron diffraction and examine the magnetic structure. The preliminary results from this last method will be described in turn in the paragraphs that follow.

5.4.1 Magnetic Structure of Samples Quenched From High Temperatures

Refining the magnetic structure from neutron diffraction data provides a very clear measure of the magnetic moment on each site in Co_3O_4. The magnetic moment, in turn, is tied to the occupancy of Co^{2+} and Co^{3+} ions on a site. For example, Co^{2+} on a tetrahedral site has 3 unpaired electrons but introducing a high spin Co^{3+} ion on the tetrahedral site increases the magnetic moment because it has 4 unpaired electrons. As a result, determining the magnetic structure of Co_3O_4 as the structure undergoes inversion could be used to quantify the cation distribution. However, the temperatures where

inversion of the structure occurs are very high (800-1200 K) and Co_3O_4 transitions to an ordered antiferromagnetic state at very low temperatures (Néel temperature is 40 K). Above the Néel temperature, cobalt oxide is paramagnetic and no magnetic structure reflections are observed; thus, the magnetic structure can only be determined below 40 K.

Our approach to this problem was to heat a series of Co_3O_4 powders to various temperatures (298 K, 773 K, 823 K, 873 K, 923 K, 973 K, 1023 K, 1073 K, 1123 K and 1173 K). The samples were then rapidly quenched in hopes that the high temperature electronic and crystal structure would be preserved and the magnetic structure of the quenched samples could be investigated. Neutron diffraction patterns measured for a sample above (300 K) and below (1.5 K) its magnetic ordering temperature are shown in Figure 5.12 to exhibit the additional scattering from the magnetic structure.

The increase in peak intensity below the Néel temperature is not uniform for all reflections because the magnetic structure and the crystal structure belong to different space groups (F-43m and Fd3m symmetry respectively, see Figure 5.13). For example, the (200) and (420) peaks are principally magnetic reflections, (220) and (224) are principally nuclear reflections and the remainder have contributions from both. Normal spinel Co_3O_4 has no magnetic moment on the octahedral B site because Co^{3+} is low spin and has no unpaired electrons. The magnetic structure arises only from the unpaired electrons on the tetrahedral A site.

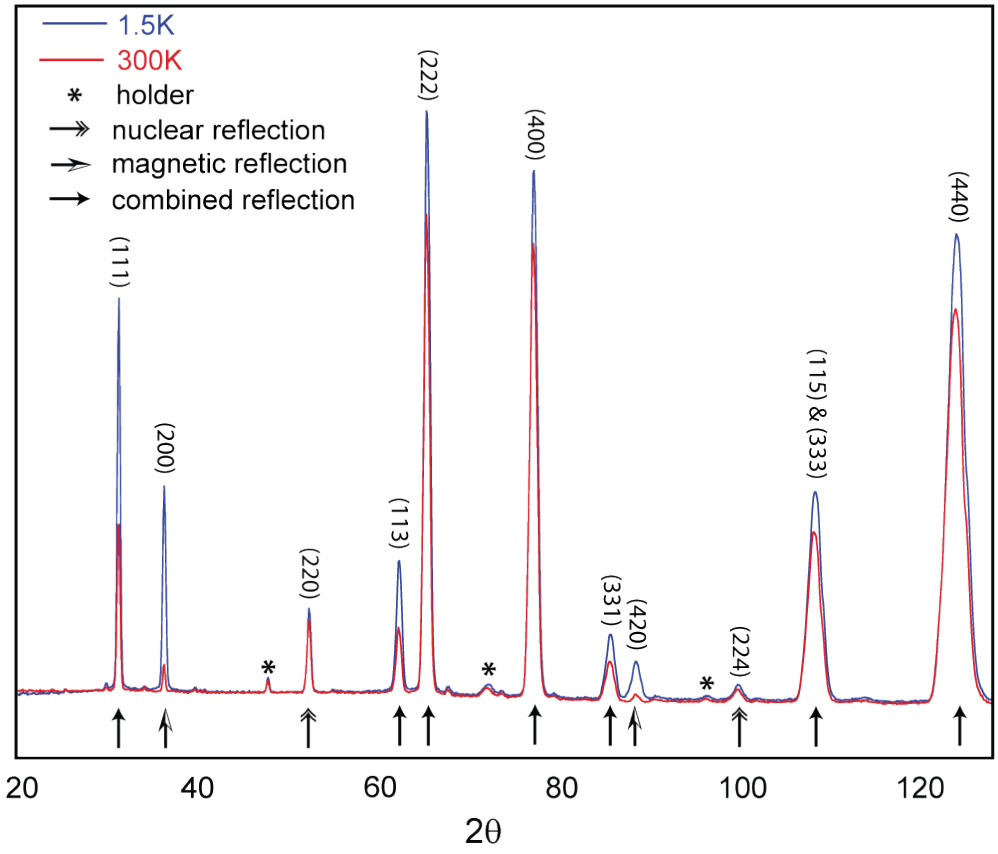

Figure 5.12. Neutron diffraction patterns for Co_3O_4 powder quenched from 1173 K measured at 300 K and 1.5 K. Nuclear, magnetic and combined reflections are indicated.

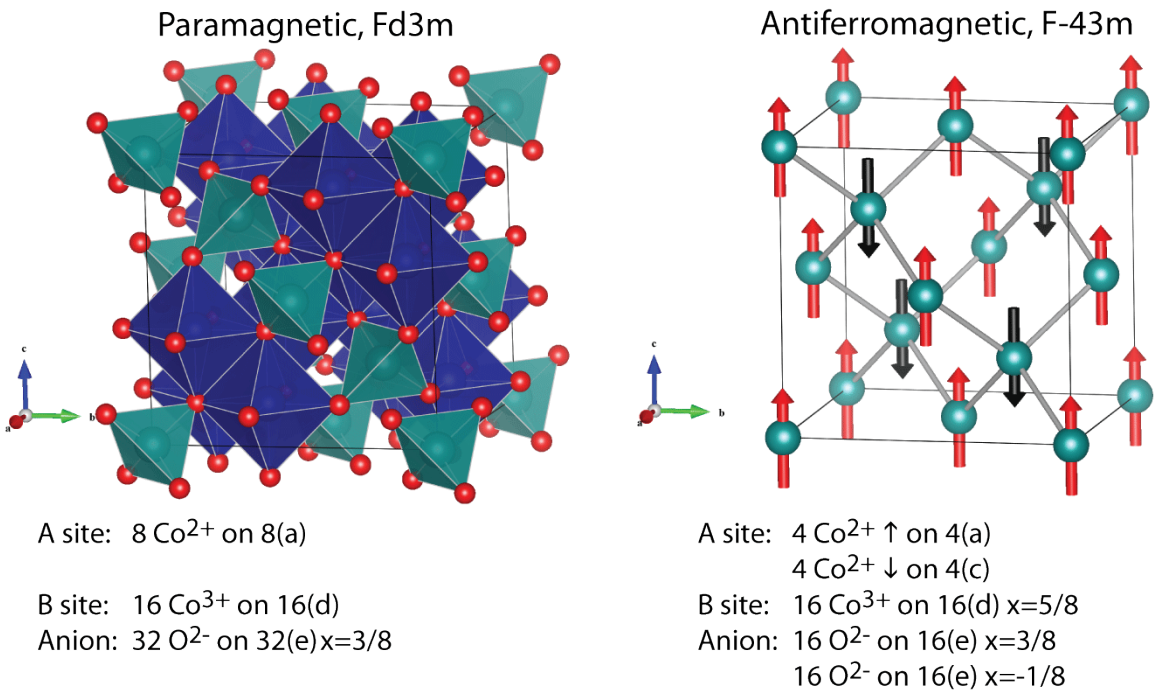

Figure 5.13. (left) Paramagnetic structure of Co_3O_4. Though both A and B sites have cobalt ions, for clarity, the B site octahedra are shown in blue and A site tetrahedra are shown in teal. (right) Antiferromagnetic structure of Co_3O_4. B site octahedra are omitted because they contain no magnetic moment. Red and blue arrows indicate up and down spins.

Refinement of the magnetic structure for these neutron diffraction patterns is not yet complete. Nevertheless, when the patterns of samples quenched from all temperatures are compared, as in Figure 5.14, there are two important observations. First, the patterns from samples quenched at high temperatures have sharper peaks and, second, the ratio of intensity of magnetic to nuclear reflections is changing as a function of temperature. The former can be understood by the powders coarsening at elevated temperatures. The latter observation could be evidence of inversion and is quantified in Figure 5.15 where the

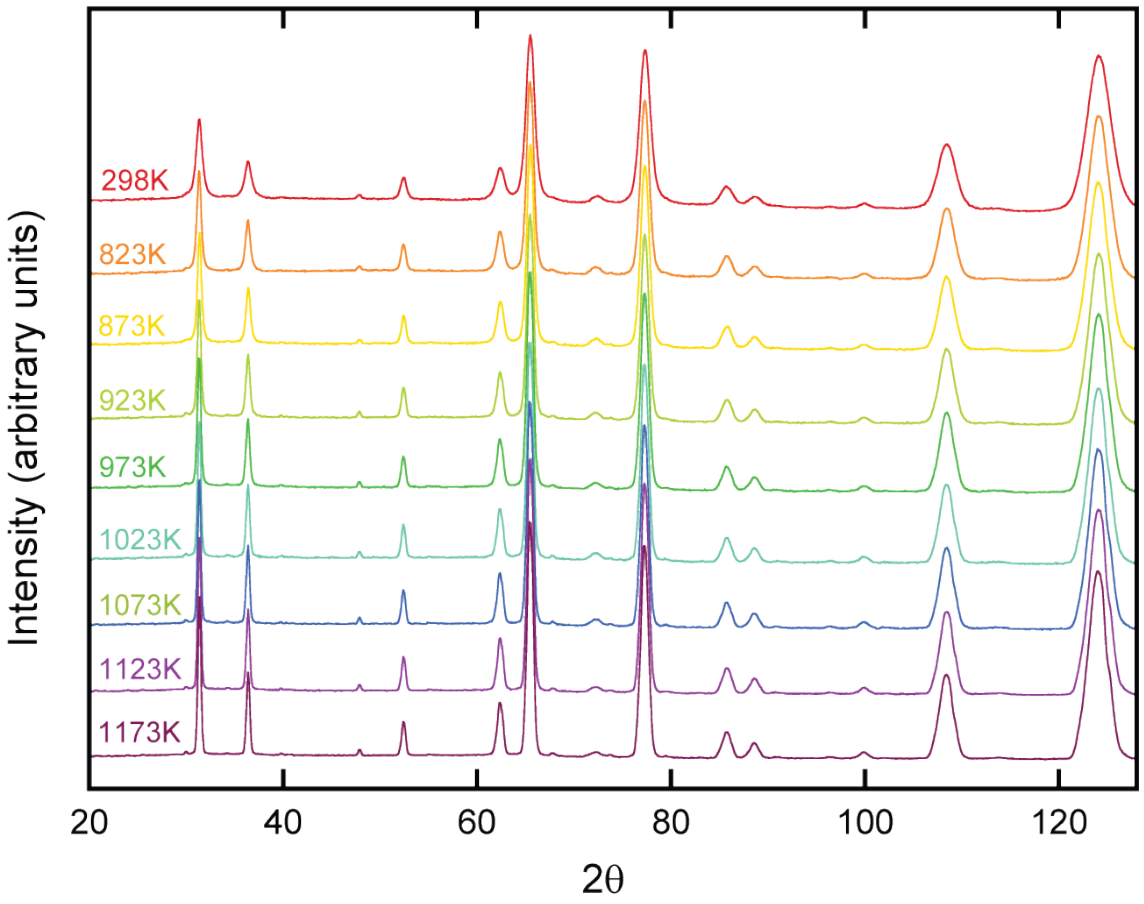

Figure 5.14. Neutron diffraction patterns measured at 1.5 K for Co_3O_4 samples quenched from various temperatures.

ratio of the magnetic (200) reflection to the nuclear (220) and (224) reflections is plotted as a function of quenching temperature.

As was portrayed in Table 6, inversion of Co_3O_4 introduces high spin Co^{3+} ions featuring four unpaired electrons on the tetrahedral site. This extra unpaired electron relative to high spin Co^{2+} ions normally on the site should increase the magnetic moment and, therefore, the magnetic scattering. While anti-site disorder qualitatively describes the

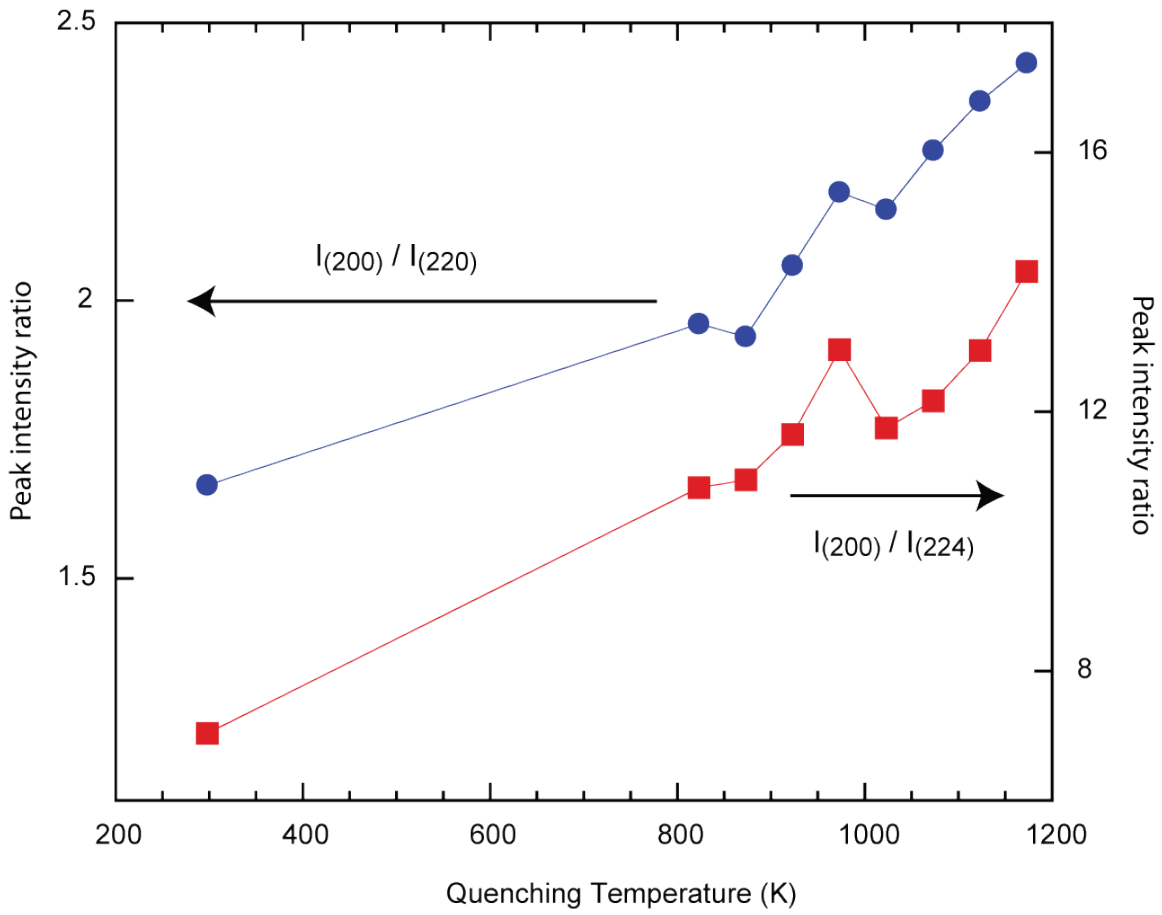

Figure 5.15. Ratio of peak intensity for magnetic (200) and nuclear reflections (220) and (224). The ratios increase as a function of temperature possibly indicating that the magnetic moment on the A site is increasing with temperature.

trend in Figure 5.15, inversion would also require that Co^{2+} ions with unpaired electrons occupy the octahedral site which should result in a magnetic moment on the B site. The effect of a small B site magnetic moment on the low temperature neutron diffraction patterns will be considered in detail when the Rietveld refinement of the magnetic structure is complete.

Clearly there remain ample opportunities for further research in both the high temperature structure of Co_3O_4 as well as in the intriguing prospect of using thermopower as a measure of cation distribution in materials.

5.4.2 Conclusions

In this chapter the electrical and thermoelectric properties as well as X-ray diffraction and Raman scattering of Co_3O_4 spinel are reported from room temperature up to 1273 K. The electrical conductivity was consistent with other large band gap semiconductors with E_G=2.28 eV and E_A=0.15 eV for a small-polaron conduction mechanism. The thermopower reaches a maximum value (~600μV/K) around 850 K and above this temperature it decreased almost linearly with temperature to 109 μV/K at which the structure transformed to CoO rock-salt. The temperature of this transformation decreased slightly (~ 40 K) when measured in helium, rather than air.

The thermopower correlates to partial inversion of the Co_3O_4 structure, but the cation distribution cannot be explained in a quantifiable and consistent way unless a change in spin state is considered using either Wu and Mason's original model *case (i)*, or one based on Koshibae et al.'s modified thermopower expression, *case (ii)*. When thermopower contributions from both electron-doped octahedral sites as well as hole-doped tetrahedral sites are included, taking into account both spin and orbital degeneracy as well as the ratio of these degeneracies, *case (iii)*, a stoichiometrically consistent cation distribution is observed with or without a change in spin state. This case agrees well with Chen et al.'s cation distribution calculated from free energies as well as the distribution

calculated from bond lengths and ionic radii. Neutron diffraction of Co_3O_4 powders quenched from elevated temperatures indicate that the magnetic moment on the A site is increasing with quenching temperature suggesting increased anti-site disorder at elevated temperature. In agreement with previous studies, the spinel lattice parameter is unusually large at values above 900 K. While this has been attributed to a change in spin-state of the Co^{3+} ions by other authors, the thermopower results in the current work show no definitive evidence of such a change in spin state.

Chapter 6. Thesis Summary and Outlook

The Seebeck coefficient is a direct probe of the carrier type and entropy per carrier and, as such, is a truly fundamental measurement in materials. For strongly correlated systems in particular, the strong coupling between charge, orbital, spin and lattice degrees of freedom means that thermopower is intimately related to the crystal structure in a way that neither electrical or thermal conductivity alone would be. The objective of this dissertation was not only to highlight these structure-thermopower relationships, but also to apply them towards developing better oxide thermoelectric materials and as a characterization tool to improve our understanding of materials.

In the context of thermoelectric power generation and refrigeration one important accomplishment resulting from our experiments was identifying that Mn oxides need not be limited to the small thermopower value of -20 μV/K at high temperatures. By understanding the effect of Jahn-Teller distortions on the electronic degeneracy a Mn oxide, $LiMn_2O_4$, was identified that had thermopower values over 3 times greater than other small-polaron conducting Mn oxides. Though the electrical resistivity of $LiMn_2O_4$ is still prohibitively large for practical thermoelectric application this study represents an advance in developing n-type oxide thermoelectric materials to compliment their better performing p-type counterparts. There is outstanding potential to use thermopower as a

probe of crystal structure in materials and to apply the modified Heikes formula as a screening tool to find new oxide thermoelectric materials as well.

For over 30 years thermopower has been used as a valuable tool to characterize cation distribution in spinels. We have revisited using thermopower to calculate the cation distribution in spinels by examining the temperature dependant thermopower and high temperature structural anomaly of Co_3O_4. The experiments offer evidence that Wu et al.'s model could be altered to include Koshibae et al.'s modified Heikes formula and to account for octahedral and tetrahedral contributions to thermopower. However, as I have demonstrated in this thesis, the complex structural and magnetic transitions (anti-site disorder, spin unpairing etc) possible in spinels make use of thermopower to precisely determine cation distribution unlikely.

References

1. Hubbert, M. K. Nuclear Energy and the Fossil Fuels. *Spring Meeting of the Southern District, American Petroleum Institute, Plaza Hotel, San Antonio, Texas, March 7–8-9* (1956).

2. U.S. Energy Information Administration Annual Energy Outlook 2011 with Projections to 2035. *DOE/EIA-0383(2011)*

3. U.S. Energy Information Administration Electric Power Monthly January 2010. *DOE/EIA-0226(2010/01)*

4. DOE/Lawrence Livermore National Laboratory Wind turbines: In the wake of the wind. *ScienceDaily* (2011).at <http://www.sciencedaily.com/releases/2011/04/110426151040.htm>

5. Lawrence Livermore National Laboratory Estimated U.S. Energy Use in 2010: 98.0 Quads. (2011).at <https://flowcharts.llnl.gov/content/energy/energy_archive/energy_flow_2010/LLNLUSEnergy2010.pdf>

6. Rama Venkatasubramanian Nanoscale Thermoelectric Materials and Devices. (2007).

7. Yang, J. & Stabler, F. R. Automotive Applications of Thermoelectric Materials. *Journal of Electronic Materials* **38**, 1245–1251 (2009).

8. Kraemer, D. *et al.* High-performance flat-panel solar thermoelectric generators with high thermal concentration. *Nat Mater* **10**, 532–538 (2011).

9. Sales, B. C. Smaller Is Cooler. *Science* **295**, 1248 –1249 (2002).

10. Robert D. Abelson *et al.* Enabling Exploration with Small Radioisotope Power Systems. **04-10**, (2004).

11. Huffman, F. N., Migliore, J. J., Robinson, W. J. & Norman, J. C. Radioisotope Powered Cardiac Pacemakers. *IEEE Transactions on Nuclear Science* **21**, 707–713 (1974).

12. Föll, H. Electronic Materials. at <http://www.tf.uni-kiel.de/matwis/amat/elmat_en/index.html>

13. Selberherr, S. *Analysis and Simulation of Semiconductor Devices*. (Springer: 1984).

14. Tamer F., R., William S., L. & Russell J. De, Y. *Temperature Control of Avalanche Photodiode Using Thermoelectric Cooler*. (NASA Langley Technical Report Server: 1999).

15. Goldsmid, H. J. *Electronic refrigeration*. (Pion: 1986).

16. Heikes, R. R. & Ure, R. W. *Thermoelectricity: science and engineering*. (Interscience Publishers: 1961).

17. Snyder, G. J. & Ursell, T. S. Thermoelectric Efficiency and Compatibility. *Phys. Rev. Lett.* **91**, 148301 (2003).

18. Gordon, J. M. & Huleihil, M. General performance characteristics of real heat engines. *Journal of Applied Physics* **72**, 829–837 (1992).

19. Fernandez-Pello, C. Micropower generation using combustion: Issues and approaches. *Proceedings of the Combustion Institute* **29**,

20. Vining, C. B. An inconvenient truth about thermoelectrics. *Nat Mater* **8**, 83–85 (2009).

21. Desai, A. V., Jhirad, D. & Munasinghe, M. *Nonconventional energy*. (New Age International: 1990).

22. Ginley, D. S. & Cahen, D. *Fundamentals of Materials for Energy and Environmental Sustainability*. (Cambridge University Press: 2011).

23. Goldsmid, H. J. & Douglas, R. W. The use of semiconductors in thermoelectric refrigeration. *British Journal of Applied Physics* **5**, 386–390 (1954).

24. Hébert, S. & Maignan, A. Thermoelectric Oxides. *Functional Oxides* 203–255 (2010).at <http://dx.doi.org/10.1002/9780470686072.ch4>

25. Snyder, G. J. & Toberer, E. S. Complex thermoelectric materials. *Nat Mater* **7**, 105–114 (2008).

26. Rowe, D. M. *CRC handbook of thermoelectrics*. (CRC Press: 1995).

27. Toberer, E. S., May, A. F. & Snyder, G. J. Zintl Chemistry for Designing High Efficiency Thermoelectric Materials. *Chemistry of Materials* **22**, 624–634 (2009).

28. Nolas, G. S., Poon, J. & Kanatzidis, M. Recent Developments in Bulk Thermoelectric Materials. *MRS Bulletin* **31**, 199–205 (2006).

29. Sales, B. C., Mandrus, D. & Williams, R. K. Filled Skutterudite Antimonides: A New Class of Thermoelectric Materials. *Science* **272**, 1325 –1328 (1996).

30. Feldman, J. L., Singh, D. J., Mazin, I. I., Mandrus, D. & Sales, B. C. Lattice dynamics and reduced thermal conductivity of filled skutterudites. *Phys. Rev. B* **61**, R9209–R9212 (2000).

31. Caillat, T., Fleurial, J.-P. & Borshchevsky, A. Preparation and thermoelectric properties of semiconducting Zn4Sb3. *Journal of Physics and Chemistry of Solids* **58**, 1119–1125 (1997).

32. Nolas, G. S., Slack, G. A., Morelli, D. T., Tritt, T. M. & Ehrlich, A. C. The effect of rare-earth filling on the lattice thermal conductivity of skutterudites. *Journal of Applied Physics* **79**, 4002–4008 (1996).

33. Callaway, J. & von Baeyer, H. Effect of Point Imperfections on Lattice Thermal Conductivity. *Physical Review* **120**, 1149–1154 (1960).

34. Abeles, B. Lattice Thermal Conductivity of Disordered Semiconductor Alloys at High Temperatures. *Phys. Rev.* **131**, 1906–1911 (1963).

35. Wood, C. Materials for thermoelectric energy conversion. *Reports on Progress in Physics* **51**, 459–539 (1988).

36. Qu, Z., Sparks, T. D., Pan, W. & Clarke, D. R. Thermal conductivity of the gadolinium calcium silicate apatites: Effect of different point defect types. *Acta Materialia* **59**, 3841–3850 (2011).

37. Klemens, P. G. & Gell, M. Thermal conductivity of thermal barrier coatings. *Materials Science and Engineering: A* **245**, 143–149 (1998).

38. Winter, M. R. & Clarke, D. R. Thermal conductivity of yttria-stabilized zirconia–hafnia solid solutions. *Acta Materialia* **54**, 5051–5059 (2006).

39. Shen, Y., Clarke, D. R. & Fuierer, P. A. Anisotropic thermal conductivity of the Aurivillus phase, bismuth titanate (Bi4Ti3O12): A natural nanostructured superlattice. *Applied Physics Letters* **93**, 102907 (2008).

40. Sparks, T. D., Fuierer, P. A. & Clarke, D. R. Anisotropic Thermal Diffusivity and Conductivity of La-Doped Strontium Niobate Sr2Nb2O7. *Journal of the American Ceramic Society* **93**, 1136–1141 (2010).

41. Koumoto, K., Terasaki, I. & Funahashi, R. Complex Oxide Materials for Potential Thermoelectric Applications. *MRS Bulletin* **31**, 206–210 (2006).

42. Terasaki, I., Sasago, Y. & Uchinokura, K. Large thermoelectric power in NaCo2O4 single crystals. *Phys. Rev. B* **56**, R12685–R12687 (1997).

43. Wan, C., Sparks, T. D., Wei, P. & Clarke, D. R. Thermal Conductivity of the Rare-Earth Strontium Aluminates. *Journal of the American Ceramic Society* **93**, 1457–1460 (2010).

44. Shin, W. & Murayama, N. Thermoelectric properties of (Bi,Pb)-Sr-Co-O oxide. *Journal of Materials Research* **15**, 382–386 (2000).

45. Gascoin, F., Ottensmann, S., Stark, D., Haïle, S. M. & Snyder, G. J. Zintl Phases as Thermoelectric Materials: Tuned Transport Properties of the Compounds CaxYb1–xZn2Sb2. *Advanced Functional Materials* **15**, 1860–1864 (2005).

46. Zhu, P. *et al.* Enhanced thermoelectric properties of PbTe alloyed with Sb2Te3. *Journal of Physics: Condensed Matter* **17**, 7319–7326 (2005).

47. Poudeu, P. F. P. *et al.* High Thermoelectric Figure of Merit and Nanostructuring in Bulk p-type Na1−xPbmSbyTem+2. *Angewandte Chemie* **118**, 3919–3923 (2006).

48. Poudeu, P. F. P. *et al.* Nanostructures versus Solid Solutions: Low Lattice Thermal Conductivity and Enhanced Thermoelectric Figure of Merit in Pb9.6Sb0.2Te10-xSex Bulk Materials. *Journal of the American Chemical Society* **128**, 14347–14355 (2006).

49. WRIGHT, D. A. Thermoelectric Properties of Bismuth Telluride and its Alloys. *Nature* **181**, 834 (1958).

50. Kusano, D. & Hori, Y. Thermoelectric properties of p-type (Bi2Te3)0.2(Sb2Te3)0.8 thermoelectric material doped with PbTe. *Nippon Kinzoku Gakkaishi* **66**, 1063–1065

51. Goldsmid, H. J. & Penn, A. W. Boundary scattering of phonons in solid solutions. *Physics Letters A* **27**, 523–524 (1968).

52. Kim, W. *et al.* Cross-plane lattice and electronic thermal conductivities of ErAs:InGaAs/InGaAlAs superlattices. *Applied Physics Letters* **88**, 242107–242107–3 (2006).

53. Hsu, K. F. *et al.* Cubic AgPbmSbTe2+m: Bulk Thermoelectric Materials with High Figure of Merit. *Science* **303**, 818 –821 (2004).

54. Caylor, J. C., Coonley, K., Stuart, J., Colpitts, T. & Venkatasubramanian, R. Enhanced thermoelectric performance in PbTe-based superlattice structures from reduction of lattice thermal conductivity. *Applied Physics Letters* **87**, 023105–023105–3 (2005).

55. Hochbaum, A. I. *et al.* Enhanced thermoelectric performance of rough silicon nanowires. *Nature* **451**, 163–167 (2008).

56. Beyer, H. *et al.* High thermoelectric figure of merit ZT in PbTe and Bi2Te3-based superlattices by a reduction of the thermal conductivity. *Physica E: Low-dimensional Systems and Nanostructures* **13**, 965–968 (2002).

57. Poudel, B. *et al.* High-Thermoelectric Performance of Nanostructured Bismuth Antimony Telluride Bulk Alloys. *Science* **320**, 634 –638 (2008).

58. Cahill, D. G., Watson, S. K. & Pohl, R. O. Lower limit to the thermal conductivity of disordered crystals. *Phys. Rev. B* **46**, 6131–6140 (1992).

59. Chen, N. *et al.* Macroscopic thermoelectric inhomogeneities in (AgSbTe2)x(PbTe)1-x. *Applied Physics Letters* **87**, 171903–171903–3 (2005).

60. Cook, B. A., Kramer, M. J., Wei, X., Harringa, J. L. & Levin, E. M. Nature of the cubic to rhombohedral structural transformation in (AgSbTe2)15(GeTe)85 thermoelectric material. *Journal of Applied Physics* **101**, 053715–053715–6 (2007).

61. Boukai, A. I. *et al.* Silicon nanowires as efficient thermoelectric materials. *Nature* **451**, 168–171 (2008).

62. Touzelbaev, M. N., Zhou, P., Venkatasubramanian, R. & Goodson, K. E. Thermal characterization of Bi2Te3/Sb2Te3 superlattices. *Journal of Applied Physics* **90**, 763–767 (2001).

63. Kim, W. *et al.* Thermal Conductivity Reduction and Thermoelectric Figure of Merit Increase by Embedding Nanoparticles in Crystalline Semiconductors. *Phys. Rev. Lett.* **96**, 045901 (2006).

64. Yao, T. Thermal properties of AlAs/GaAs superlattices. *Applied Physics Letters* **51**, 1798–1800 (1987).

65. Chiritescu, C. *et al.* Ultralow Thermal Conductivity in Disordered, Layered WSe2 Crystals. *Science* **315**, 351 –353 (2007).

66. Kim, H. J., Božin, E. S., Haile, S. M., Snyder, G. J. & Billinge, S. J. L. Nanoscale α-structural domains in the phonon-glass thermoelectric material β-Zn4Sb3. *Phys. Rev. B* **75**, 134103 (2007).

67. Winter, M. R. & Clarke, D. R. Oxide Materials with Low Thermal Conductivity. *Journal of the American Ceramic Society* **90**, 533–540 (2007).

68. Kanatzidis, M. G. Structural Evolution and Phase Homologies for ‘Design’ and Prediction of Solid-State Compounds. *Acc. Chem. Res.* **38**, 359–368 (2004).

69. Kauzlarich, S. M., Brown, S. R. & Snyder, G. J. Zintl phases for thermoelectric devices. *Dalton Trans.* 2099–2107 (2007).doi:10.1039/B702266B

70. Gordon B. Haxel, James B. Hedrick & Greta J. Orris Rare Earth Elements—Critical Resources for High Technology | USGS Fact Sheet 087-02. *U.S. Geological Survey Fact Sheet 087-02* at <http://pubs.usgs.gov/fs/2002/fs087-02/>

71. U.S. Department of Energy U.S. Department of Energy Critical Materials Strategy. (2010).

72. Michael George USGS Minerals Information: Selenium and Tellurium. *USGS 2010 Minerals Yearbook* (2010).at <http://minerals.usgs.gov/minerals/pubs/commodity/selenium/>

73. Mott, N. F. & Davis, E. A. *Electronic Processes in Non-Crystalline Materials*. (Oxford University Press, USA: 1979).

74. Mott, N. F. & Jones, H. *The Theory of the Properties of Metals and Alloys*. (Dover Publications: 1958).

75. Nolas, G. S., Sharp, J. & Goldsmid, J. *Thermoelectrics: Basic Principles and New Materials Developments*. (Springer: 2001).

76. Hicks, L. D. & Dresselhaus, M. S. Effect of quantum-well structures on the thermoelectric figure of merit. *Phys. Rev. B* **47**, 12727–12731 (1993).

77. Hicks, L. D., Harman, T. C., Sun, X. & Dresselhaus, M. S. Experimental study of the effect of quantum-well structures on the thermoelectric figure of merit. *Phys. Rev. B* **53**, R10493–R10496 (1996).

78. Venkatasubramanian, R., Siivola, E., Colpitts, T. & O’Quinn, B. Thin-film thermoelectric devices with high room-temperature figures of merit. *Nature* **413**, 597–602 (2001).

79. Zide, J. M. O. *et al.* Demonstration of electron filtering to increase the Seebeck coefficient in In0.53Ga0.47As/In0.53Ga0.28Al0.19As superlattices. *Phys. Rev. B* **74**, 205335 (2006).

80. Dresselhaus, M. S. *et al.* New Directions for Low-Dimensional Thermoelectric Materials. *Advanced Materials* **19**, 1043–1053 (2007).

81. DiSalvo, F. J. Thermoelectric Cooling and Power Generation. *Science* **285**, 703 –706 (1999).

82. Ohta, H., Seo, W. & Koumoto, K. Thermoelectric Properties of Homologous Compounds in the ZnO–In2O3 System. *Journal of the American Ceramic Society* **79**, 2193–2196 (1996).

83. Tsubota, T., Ohtaki, M., Eguchi, K. & Arai, H. Thermoelectric properties of Al-doped ZnO as a promising oxide material for high-temperature thermoelectric conversion. *Journal of Materials Chemistry* **7**, 85–90 (1997).

84. Cai, K. F., Müller, E., Drašar, C. & Mrotzek, A. Preparation and thermoelectric properties of Al-doped ZnO ceramics. *Materials Science and Engineering: B* **104**, 45–48 (2003).

85. Bhosle, V., Tiwari, A. & Narayan, J. Metallic conductivity and metal-semiconductor transition in Ga-doped ZnO. *Applied Physics Letters* **88**, 032106 (2006).

86. Singh, S. *et al.* Structure, microstructure and physical properties of ZnO based materials in various forms: bulk, thin film and nano. *Journal of Physics D: Applied Physics* **40**, 6312–6327 (2007).

87. Guilmeau, E., Maignan, A. & Martin, C. Thermoelectric Oxides: Effect of Doping in Delafossites and Zinc Oxide. *Journal of Electronic Materials* **38**, 1104–1108 (2009).

88. Jood, P. *et al.* Al-Doped Zinc Oxide Nanocomposites with Enhanced Thermoelectric Properties. *Nano Letters* **11**, 4337–4342 (2011).

89. Maignan, A., Martin, C., Damay, F., Raveau, B. & Hejtmanek, J. Transition from a paramagnetic metallic to a cluster glass metallic state in electron-doped perovskite manganites. *Phys. Rev. B* **58**, 2758–2763 (1998).

90. Hejtmánek, J. *et al.* Interplay between transport, magnetic, and ordering phenomena in Sm1-xCaxMnO3. *Phys. Rev. B* **60**, 14057–14065 (1999).

91. Raveau, B., Zhao, Y. M., Martin, C., Hervieu, M. & Maignan, A. Mn-Site Doped CaMnO3: Creation of the CMR Effect. *Journal of Solid State Chemistry* **149**, 203–207 (2000).

92. Matsubara, I. *et al.* Fabrication of an all-oxide thermoelectric power generator. *Applied Physics Letters* **78**, 3627 (2001).

93. Maignan, A. *et al.* Structural–magnetic phase diagram of Mo-substituted CaMnO3: consequences for thermoelectric power properties. *J. Mater. Chem.* **12**, 1806–1811 (2002).

94. Flahaut, D., Funahashi, R., Lee, K., Ohta, H. & Koumoto, K. Effect of the Yb substitutions on the thermoelectric properties of CaMnO3. *25th International Conference on Thermoelectrics, 2006. ICT '06* 103–106 (2006).doi:10.1109/ICT.2006.331291

95. Bocher, L. *et al.* CaMn1−x NbxO3 (x ≤ 0.08) Perovskite-Type Phases As Promising New High-Temperature n-Type Thermoelectric Materials. *Inorgnic Chemistry* **47**, 8077–8085 (2008).

96. Wang, Y. *et al.* High Temperature Thermoelectric Response of Electron-Doped CaMnO3. *Chemistry of Materials* **21**, 4653–4660 (2009).

97. Park, J. W., Kwak, D. H., Yoon, S. H. & Choi, S. C. Thermoelectric properties of Bi, Nb co-substituted CaMnO3 at high temperature. *Journal of Alloys and Compounds* **487**, 550–555 (2009).

98. Populoh, S., Trottmann, M., Aguire, M. H. & Weidenkaff, A. Nanostructured Nb-Substituted CaMnO3 N-Type Thermoelectric Material Prepared in a Continuous Process by Ultrasonic Spray Combustion. *Journal of Materials Research* **26**, 1947–1952 (2011).

99. Okuda, T., Nakanishi, K., Miyasaka, S. & Tokura, Y. Large thermoelectric response of metallic perovskites: Sr1-xLaxTiO3 (0<~x<~0.1). *Phys. Rev. B* **63**, 113104 (2001).

100. Muta, H., Kurosaki, K. & Yamanaka, S. Thermoelectric properties of rare earth doped SrTiO3. *Journal of Alloys and Compounds* **350**, 292–295 (2003).

101. Ohta, S. *et al.* Large thermoelectric performance of heavily Nb-doped SrTiO3 epitaxial film at high temperature. *Applied Physics Letters* **87**, 092108 (2005).

102. Ohta, S., Nomura, T., Ohta, H. & Koumoto, K. High-temperature carrier transport and thermoelectric properties of heavily La- or Nb-doped SrTiO3 single crystals. *Journal of Applied Physics* **97**, 034106–034106–4 (2005).

103. Ohta, H. *et al.* Giant thermoelectric Seebeck coefficient of a two-dimensional electron gas in SrTiO3. *Nat Mater* **6**, 129–134 (2007).

104. Edwards, P. P., Porch, A., Jones, M. O., Morgan, D. V. & Perks, R. M. Basic materials physics of transparent conducting oxides. *Dalton Transactions* 2995 (2004).doi:10.1039/b408864f

105. Bizo, L., Choisnet, J., Retoux, R. & Raveau, B. The great potential of coupled substitutions in In2O3 for the generation of bixbyite-type transparent conducting oxides, In2−2xMxSnxO3. *Solid State Communications* **136**, 163–168 (2005).

106. Bérardan, D., Guilmeau, E., Maignan, A. & Raveau, B. In2O3:Ge, a promising n-type thermoelectric oxide composite. *Solid State Communications* **146**, 97–101 (2008).

107. Berardan, D., Guilmeau, E., Maignan, A. & Raveau, B. Enhancement of the thermoelectric performances of In2O3 by the coupled substitution of M2+/Sn4+ for In3+. *Journal of Applied Physics* **104**, 064918–064918–5 (2008).

108. Guilmeau, E. *et al.* Tuning the transport and thermoelectric properties of In2O3 bulk ceramics through doping at In-site. *Journal of Applied Physics* **106**, 053715–053715–7 (2009).

109. Sakai, A., Kanno, T., Takahashi, K., Yamada, Y. & Adachi, H. Large anisotropic thermoelectricity in perovskite related layered structure: SrnNbnO3n+2 (n=4,5). *Journal of Applied Physics* **108**, 103706–103706–5 (2010).

110. Fujita, K., Mochida, T. & Nakamura, K. High-Temperature Thermoelectric Properties of NaxCoO2-δ Single Crystals. *Jpn. J. Appl. Phys.* **40**, 4644–4647 (2001).

111. Koshibae, W., Tsutsui, K. & Maekawa, S. Thermopower in cobalt oxides. *Phys. Rev. B* **62**, 6869–6872 (2000).

112. Koshibae, W. & Maekawa, S. Effects of Spin and Orbital Degeneracy on the Thermopower of Strongly Correlated Systems. *Phys. Rev. Lett.* **87**, 236603 (2001).

113. Maekawa, S. *et al. Physics of Transition Metal Oxides (Springer Series in Solid-State Sciences)*. (Springer: 2004).

114. Koshibae, W. & Maekawa, S. Thermoelectric Effect in Transition Metal Oxides. *Properties and Applications of Thermoelectric Materials* 69–79 (2009).at <http://www.springerlink.com/content/vw75871456731022/>

115. Tajima, S., Tani, T., Isobe, S. & Koumoto, K. Thermoelectric properties of highly textured NaCo2O4 ceramics processed by the reactive templated grain growth (RTGG) method. *Materials Science and Engineering: B* **86**, 20–25 (2001).

116. Pelloquin, D. *et al.* New Misfit Cobaltites [Pb0.7A0.4Sr1.9O3][CoO2]1.8 (A = Hg, Co) with Large Thermopower. *Chemistry of Materials* **14**, 3100–3105 (2002).

117. I., T. Transport properties and electronic states of the thermoelectric oxide NaCo2O4. *Physica B: Condensed Matter* **328**, 63–67 (2003).

118. Park, K. & Jang, K. U. Improvement in high-temperature thermoelectric properties of NaCo2O4 through partial substitution of Ni for Co. *Materials Letters* **60**, 1106–1110 (2006).

119. Park, K., Jang, K. U., Kwon, H.-C., Kim, J.-G. & Cho, W.-S. Influence of partial substitution of Cu for Co on the thermoelectric properties of NaCo2O4. *Journal of Alloys and Compounds* **419**, 213–219 (2006).

120. Dutta, B. *et al.* Thermoelectric Properties of NaCo2–x Fe x O y. *Journal of Electronic Materials* **36**, 746–752 (2007).

121. Miyazaki *et al.* Low-temperature thermoelectric properties of the composite crystal [Ca2CoO3.34]0.614[CoO2]. *Japanese Journal Of Applied Physics Part 2 Letters* **39**, L531–3 (2000).

122. Funahashi, R. & Matsubara, I. Thermoelectric properties of Pb- and Ca-doped (Bi2Sr2O4)CoO2 whiskers. *Applied Physics Letters* **79**, 362 (2001).

123. Hervieu, M. *et al.* Metallicity and thermopower of the misfit cobaltite [Bi2Ba1.8Co0.2O4]RS[CoO2]2. *Phys. Rev. B* **67**, 045112 (2003).

124. Shikano, M. & Funahashi, R. Electrical and thermal properties of single-crystalline (Ca2CoO3)0.7CoO2 with a Ca3Co4O9 structure. *Applied Physics Letters* **82**, 1851–1853 (2003).

125. Masuda, Y. *et al.* Thermoelectric performance of Bi- and Na-substituted Ca3Co4O9 improved through ceramic texturing. *Journal of Materials Chemistry* **13**, 1094–1099 (2003).

126. Maignan, A. *et al.* Magnetoresistance and magnetothermopower properties of Bi/Ca/Co/O and Bi(Pb)/Ca/Co/O misfit layer cobaltites. *Journal of Physics: Condensed Matter* **15**, 2711–2723 (2003).

127. Wang, D., Chen, L., Yao, Q. & Li, J. High-temperature thermoelectric properties of Ca3Co4O9+δ with Eu substitution. *Solid State Communications* **129**, 615–618 (2004).

128. Limelette, P. *et al.* Strongly correlated properties of the thermoelectric cobalt oxide Ca3Co4O9. *Phys. Rev. B* **71**, 233108 (2005).

129. Prevel, M. *et al.* Textured Ca3Co4O9 thermoelectric oxides by thermoforging process. *Journal of Applied Physics* **98**, 093706–093706–4 (2005).

130. Sugiura, K. *et al.* High electrical conductivity of layered cobalt oxide Ca3Co4O9 epitaxial films grown by topotactic ion-exchange method. *Applied Physics Letters* **89**, 032111–032111–3 (2006).

131. Maignan, A., Flahaut, D. & Hébert, S. Sign change of the thermoelectric power in LaCoO3. *The European Physical Journal B* **39**, 145–148 (2004).

132. Pelloquin, D., Hébert, S., Maignan, A. & Raveau, B. Partial substitution of rhodium for cobalt in the misfit [Pb0.7Co0.4Sr1.9O3]RS[CoO2]1.8 oxide. *Journal of Solid State Chemistry* **178**, 769–775 (2005).

133. Kobayashi, W., Hébert, S., Pelloquin, D., Pérez, O. & Maignan, A. Enhanced thermoelectric properties in a layered rhodium oxide with a trigonal symmetry. *Phys. Rev. B* **76**, 245102 (2007).

134. Marsh, D. B. & Parris, P. E. Theory of the Seebeck coefficient in LaCrO3 and related perovskite systems. *Phys. Rev. B* **54**, 7720–7728 (1996).

135. Pal, S., Hébert, S., Yaicle, C., Martin, C. & Maignan, A. Transport and magnetic properties of Pr1-xCaxCrO3 (x = 0.0–0.5): effect of t2g orbital degeneracy on the thermoelectric power. *The European Physical Journal B* **53**, 5–9 (2006).

136. Kobayashi, W. *et al.* Universal charge transport of the Mn oxides in the high temperature limit. *Journal of Applied Physics* **95**, 6825–6827 (2004).

137. Sparks, T. D., Gurlo, A. & Clarke, D. R. Enhanced n-type thermopower in distortion-free LiMn2O4. *Journal of Materials Chemistry* **22**, 4631–4636 (2012).

138. Sparks, T. D., Gurlo, A. & Clarke, D. R. Revisiting thermopower measurement of cation distribution in spinels: a Co3O4 case study. *in preparation*

139. Williams, G. V. M., Hemery, E. K. & McCann, D. Magnetic and transport properties of SrFeOx. *Physical Review B - Condensed Matter and Materials Physics* **79**, (2009).

140. Taskin, A. A., Lavrov, A. N. & Ando, Y. Origin of the large thermoelectric power in oxygen-variable RBaCo2O5+x (R=Gd,Nd). *Phys. Rev. B* **73**, 121101 (2006).

141. Jansen, M. & Hoppe, R. Notiz zur Kenntnis der Oxocobaltate des Natriums. *Zeitschrift für anorganische und allgemeine Chemie* **408**, 104–106 (1974).

142. Tanaka, T., Nakamura, S. & Iida, S. Observation of Distinct Metallic Conductivity in NaCo2O4. *Japanese Journal of Applied Physics* **33**, L581–L582 (1994).

143. Ray, R., Ghoshray, A., Ghoshray, K. & Nakamura, S. 59Co NMR studies of metallic NaCo2O4. *Phys. Rev. B* **59**, 9454–9461 (1999).

144. Maignan, A., Caignaert, V., Raveau, B., Khomskii, D. & Sawatzky, G. Thermoelectric Power of HoBaCo2O5.5: Possible Evidence of the Spin Blockade in Cobaltites. *Phys. Rev. Lett.* **93**, 026401 (2004).

145. Hébert, S. *et al.* Thermoelectric properties of perovskites: Sign change of the Seebeck coefficient and high temperature properties. *Progress in Solid State Chemistry* **35**, 457–467 (2007).

146. Mitra, S. *Fundamentals Of Optical, Spectroscopic And X-Ray Mineralogy*. (New Age International: 1996).

147. Burns, R. G. *Mineralogical Applications of Crystal Field Theory*. (Cambridge University Press: 1993).

148. Shannon, R. D. Revised effective ionic radii and systematic studies of interatomic distances in halides and chalcogenides. *Acta Crystallographica Section A* **32**, 751–767 (1976).

149. Shannon, R. D. & Prewitt, C. T. Effective ionic radii in oxides and fluorides. *Acta Crystallographica Section B Structural Crystallography and Crystal Chemistry* **25**, 925–946 (1969).

150. Shannon, R. D. & Prewitt, C. T. Revised values of effective ionic radii. *Acta Crystallographica Section B Structural Crystallography and Crystal Chemistry* **26**, 1046–1048 (1970).

151. Shannon, R. D. & Prewitt, C. T. Effective ionic radii and crystal chemistry. *Journal of Inorganic and Nuclear Chemistry* **32**, 1427–1441 (1970).

152. Whittaker, E. J. W. & Muntus, R. Ionic radii for use in geochemistry. *Geochimica et Cosmochimica Acta* **34**, 945–956 (1970).

153. Porter, D. A. & Easterling, K. E. *Phase Transformations in Metals and Alloys, Third Edition*. (CRC Press: 1992).

154. Früh, A. File:Pourbaix Diagram of Iron.svg - Wikimedia Commons. (2006).at <http://commons.wikimedia.org/wiki/File:Pourbaix_Diagram_of_Iron.svg>

155. Rayner-Canham, G. & Overton, T. *Descriptive inorganic chemistry*. (Macmillan: 2003).

156. Mccafferty, E. *Introduction to Corrosion Science*. (Springer: 2010).

157. Munir, Z. A., Anselmi-Tamburini, U. & Ohyanagi, M. The effect of electric field and pressure on the synthesis and consolidation of materials: A review of the spark plasma sintering method. *Journal of Materials Science* **41**, 763–777 (2006).

158. Hungría, T., Galy, J. & Castro, A. Spark Plasma Sintering as a Useful Technique to the Nanostructuration of Piezo-Ferroelectric Materials. *Advanced Engineering Materials* **11**, 615–631 (2009).

159. Tiwari, Basu, B. & Biswas, K. Simulation of thermal and electric field evolution during spark plasma sintering. *Ceramics International* **35**, 699–708 (2009).

160. Brandon, D. & Kaplan, W. D. *Microstructural Characterization of Materials*. (Wiley: 2008).

161. Azaroff, L. V. *X-ray Diffraction*. (McGraw-Hill Inc.,US: 1974).

162. Dinnebier, R. E. *Powder diffraction: theory and practice*. (Royal Society of Chemistry: 2008).

163. Warren, B. E. *X-ray diffraction*. (Courier Dover Publications: 1990).

164. File:Bragg diffraction 2.svg - Wikimedia Commons. at <http://commons.wikimedia.org/wiki/File:Bragg_diffraction_2.svg>

165. Cromer, D. & von Dreele, B. FPRIME. at <http://www.ccp14.ac.uk/ccp/web-mirrors/farrugia/~louis/software/wingx/hlp/mod107.htm>

166. EPSIM 3D/JF Santarelli, Synchrotron Soleil File:Schéma de principe du synchrotron.jpg - Wikimedia Commons. at <http://commons.wikimedia.org/wiki/File:Sch%C3%A9ma_de_principe_du_synchrotron.jpg>

167. Shull, C. G. Early development of neutron scattering. *Rev. Mod. Phys.* **67**, 753–757 (1995).

168. Rietveld, H. M. A profile refinement method for nuclear and magnetic structures. *Journal of Applied Crystallography* **2**, 65–71 (1969).

169. Larson, A. C. & von, R. B. General Structure Analysis System. (1987).

170. Toby, B. H. EXPGUI, a graphical user interface for GSAS. *Journal of Applied Crystallography* **34**, 210–213 (2001).

171. Rodriguez-Carvajal, J. FULLPROF: A Program for Rietveld Refinement and Pattern Matching Analysis. *Abstracts of the Satellite Meeting on Powder Diffraction of the XV Congress of the IUCr, p. 127, Toulouse, France* (1990).

172. Bogue, R. H. Calculation of the Compounds in Portland Cement. *Ind. Eng. Chem. Anal. Ed.* **1**, 192–197 (1929).

173. Hubbard, C. R., Evans, E. H. & Smith, D. K. The reference intensity ratio,I/Ic, for computer simulated powder patterns. *Journal of Applied Crystallography* **9**, 169–174 (1976).

174. Hill, R. J. Expanded Use of the Rietveld Method In Studies of Phase Abundance in Multiphase Mixtures. *Powder Diffraction Journal* **6**, 74–77 (1991).

175. J. A. Kaduk, 'X-Ray Diffraction in the Petroleum and Petrochemical Industry'. *Industrial Applications of X-Ray Diffraction* 207–256 (1999).

176. Skoog, D. A., Holler, F. J. & Crouch, S. R. *Principles of instrumental analysis*. (Thomson Brooks/Cole: 2007).

177. Nakamoto, K. *Infrared and Raman Spectra of Inorganic and Coordination Compounds: Theory and applications in inorganic chemistry*. (John Wiley: 1997).

178. Nakamoto, K. *Infrared and Raman Spectra of Inorganic and Coordination Compounds: Applications in coordination, organometallic, and bioinorganic chemistry*. (John Wiley & Sons: 2009).

179. Slashme File:Ramanscattering.svg - Wikimedia Commons. (2007).at <http://commons.wikimedia.org/wiki/File:Ramanscattering.svg>

180. Downs, R. T. The RRUFF Project: an integrated study of the chemistry, crystallography, Raman and infrared specroscopy of minerals. *Program and Abstracts of the 19th General Meeting of the International Mineralogical Association in Kobe, Japan, O03-13* (2006).

181. ASTM Standard E1225 - 09, 'Standard Test Method for Thermal Conductivity of Solids by Means of the Guarded Comparative Longitudinal Heat Flow Technique' ASTM International, West Conshohocken, PA, 2009. at <DOI: 10.1520/E1225-09>

182. ASTM Standard C177 - 10, 'Standard Test Method for Steady State Heat Flux Measurements and Thermal Transmission Properties by Means of the Guarded Hot Plate Apparatus' ASTM International, West Conshohocken, PA, 2010. at <DOI: 10.1520/C0177-10>

183. ASTM Standard C1113 / C1113M - 09, 'Standard Test Method for Thermal Conductivity of Refractories by Hot Wire (Platinum Resistance Thermometer Technique)' ASTM International, West Conshohocken, PA, 2009. at <DOI: 10.1520/C1113_C1113M-09>

184. ASTM Standard D5930 - 09, 'Standard Test Method for Thermal Conductivity of Plastics by Means of a Transient Line Source Technique' ASTM International, West Conshohocken, PA, 2009. at <DOI: 10.1520/D5930-09>

185. Barin, I. *Thermochemical data of pure substances*. (VCH: Weinheim, Federal Republic of Germany; New York, 1993).

186. Powell, R. W., Tye, R. P., Metcalf, S. C. & Gratch, S. *Advances in Thermophysical Properties at Extreme Temperatures and Pressures*. (The American Society of Mechanical Engineers: New York, 1965).

187. Thambynayagam, R. K. M. *The Diffusion Handbook: Applied Solutions for Engineers*. (McGraw-Hill Professional: 2011).

188. Clark III, L. M. & Taylor, R. E. Radiation loss in the flash method for thermal diffusivity. *Journal of Applied Physics* **46**, 714–719 (1975).

189. Cape, J. A. & Lehman, G. W. Temperature and Finite Pulse-Time Effects in the Flash Method for Measuring Thermal Diffusivity. *Journal of Applied Physics* **34**, 1909–1913 (1963).

190. Maxwell, J. C. *A Treatise on Electricity and Magnetism (Cambridge Library Collection - Physical Sciences)*. (Cambridge University Press: 2010).

191. Johnsson, M. & Lemmens, P. Crystallography and Chemistry of Perovskites. doi:10.1002/9780470022184.hmm411

192. West, A. R. *Basic Solid State Chemistry*. (Wiley: 1999).

193. Gorshkov, V. S., Savel'ev, V. G. & Vedorov, N. F. *Physical Chemistry of Silicates and Other Refractory Compounds*. (Vysshaya Shkola: Moscow, 1988).

194. Massarotti, V. *et al.* Electric and Magnetic Properties of LiMn2O4- and Li2MnO3-Type Oxides. *Journal of Solid State Chemistry* **131**, 94–100 (1997).

195. Yamada, A. & Tanaka, M. Jahn-Teller structural phase transition around 280K in LiMn2O4. *Materials Research Bulletin* **30**, 715–721 (1995).

196. Bosi, F., Hålenius, U., Andreozzi, G. B., Skogby, H. & Lucchesi, S. Structural refinement and crystal chemistry of Mn-doped spinel: A case for tetrahedrally coordinated Mn3+ in an oxygen-based structure. *American Mineralogist* **92**, 27 –33 (2007).

197. Paulsen, J. M. & Dahn, J. R. Phase Diagram of Li−Mn−O Spinel in Air. *Chem. Mater.* **11**, 3065–3079 (1999).

198. Sickafus, K. E., Wills, J. M. & Grimes, N. W. Structure of Spinel. *Journal of the American Ceramic Society* **82**, 3279–3292 (1999).

199. Thackeray, M. M., Mansuetto, M. F., Dees, D. W. & Vissers, D. R. The thermal stability of lithium-manganese-oxide spinel phases. *Materials Research Bulletin* **31**, 133–140 (1996).

200. Mott, N. F. *Metal-Insulator Transitions*. (Taylor & Francis: London, 1990).

201. Atanasov, M., Barras, J.-L., Benco, L. & Daul, C. Electronic Structure, Chemical Bonding, and Vibronic Coupling in MnIV/MnIII Mixed Valent LixMn2O4 Spinels and Their Effect on the Dynamics of Intercalated Li: A Cluster Study Using DFT. *J. Am. Chem. Soc.* **122**, 4718–4728 (2000).

202. Julien, C. M. & Massot, M. Lattice vibrations of materials for lithium rechargeable batteries III. Lithium manganese oxides. *Materials Science and Engineering: B* **100**, 69–78 (2003).

203. Dorris, S. E. & Mason, T. O. Electrical Properties and Cation Valencies in Mn3O4. *Journal of the American Ceramic Society* **71**, 379–385 (1988).

204. Metselaar, R., Van Tol, R. E. J. & Piercy, P. The electrical conductivity and thermoelectric power of Mn3O4 at high temperatures. *Journal of Solid State Chemistry* **38**, 335–341 (1981).

205. Chen, M., Hallstedt, B. & Gauckler, L. J. Thermodynamic assessment of the Co-O system. *Journal of Phase Equilibria* **24**, 212–227 (2003).

206. Wu, C. C. & Mason, T. O. Thermopower Measurement of Cation Distribution in Magnetite. *Journal of the American Ceramic Society* **64**, 520–522 (1981).

207. Gleitzer, C., Nowotny, J. & Rekas, M. Surface and bulk electrical properties of the hematite phase Fe2O3. *Applied Physics A Solids and Surfaces* **53**, 310–316 (1991).

208. John B, G. Seebeck coefficients in vanadium spinels. *Materials Research Bulletin* **5**, 621–629 (1970).

209. Tuller, H. L. & Nowick, A. S. Small polaron electron transport in reduced CeO2 single crystals. *Journal of Physics and Chemistry of Solids* **38**, 859–867 (1977).

210. Yoo, H. & Tuller, H. L. Analytic calculation of cation distributions in ferrite spinel Mn1−γFe2 + γO4. *Journal of Physics and Chemistry of Solids* **49**, 761–766 (1988).

211. Mocala, Navrotsky, A. & Sherman, D. M. High-temperature heat capacity of Co3O4 spinel: thermally induced spin unpairing transition. *Physics and Chemistry of Minerals* **19**, 89–95 (1992).

212. Kale, G. M., Pandit, S. S. & Jacob, K. T. Thermodynamics of Cobalt (II, III) Oxide (Co3O4): Evidence of Phase Transition. *Transactions of the Japan Institute of Metals* **29**, 125–132 (1988).

213. Jung, I.-H., Decterov, S. A., Pelton, A. D., Kim, H.-M. & Kang, Y.-B. Thermodynamic evaluation and modeling of the Fe–Co–O system. *Acta Materialia* **52**, 507–519 (2004).

214. Navrotsky, A., Ma, C., Lilova, K. & Birkner, N. Nanophase Transition Metal Oxides Show Large Thermodynamically Driven Shifts in Oxidation-Reduction Equilibria. *Science* **330**, 199 –201 (2010).

215. Bahlawane, N., Tchoua Ngamou, P. H., Vannier, V. & Kottke, T. Tailoring the properties and the reactivity of the spinel cobalt oxide. *Physical Chemistry of Chemical Physics* **11**, 9224–9232 (2009).

216. Liu, X. & Prewitt, C. High-temperature X-ray diffraction study of Co3O4: Transition from normal to disordered spinel. *Physics and Chemistry of Minerals* **17**, (1990).

217. Hadjiev, V. G., Iliev, M. N. & Vergilov, I. V. The Raman spectra of Co3O4. *Journal of Physics C: Solid State Physics* **21**, L199–L201 (1988).

218. de Faria, D. L. A., Venâncio Silva, S. & de Oliveira, M. T. Raman microspectroscopy of some iron oxides and oxyhydroxides. *Journal of Raman Spectroscopy* **28**, 873–878 (1997).

219. Gallant, D., Pézolet, M. & Simard, S. Optical and Physical Properties of Cobalt Oxide Films Electrogenerated in Bicarbonate Aqueous Media. *J. Phys. Chem. B* **110**, 6871–6880 (2006).

220. Melendres, C. A. & Xu, S. In Situ Laser Raman Spectroscopic Study of Anodic Corrosion Films on Nickel and Cobalt. *J. Electrochem. Soc.* **131**, 2239–2243 (1984).

221. Ngamou, P. H. T. & Bahlawane, N. Influence of the Arrangement of the Octahedrally Coordinated Trivalent Cobalt Cations on the Electrical Charge Transport and Surface Reactivity. *Chem. Mater.* **22**, 4158–4165 (2010).

222. Koumoto, K. & Yanagida, H. Electrical Conduction in Pure and Li-Substituted Co3O4. *Journal of the American Ceramic Society* **64**, C-156–C-157 (1981).

223. Roth, W. L. The magnetic structure of Co3O4. *Journal of Physics and Chemistry of Solids* **25**, 1–10 (1964).

224. Cossee, P. Magnetic properties of cobalt in oxide lattices. *Journal of Inorganic and Nuclear Chemistry* **8**, 483 (1958).

225. Lenglet, M. & Jørgensen, C. K. Reinvestigation of the optical properties of Co3O4. *Chemical Physics Letters* **229**, 616–620 (1994).

226. Dieckmann, R., Witt, C. A. & Mason, T. O. Defects and Cation Diffusion in Magnetite (V): Electrical Conduction, Cation Distribution and Point Defects in Fe3-δO4. *Berichte der Bunsengesellschaft für physikalische Chemie* **87**, 495–503 (1983).

227. Kündig, W. & Steven Hargrove, R. Electron hopping in magnetite. *Solid State Communications* **7**, 223–227 (1969).

228. Touzelin, B. High temperature X-ray diffraction in a controlled atmosphere of cobalt and nickel oxides. *Revue Internationale des Hautes Temperatures et des Refractaires* **15**, 33–41 (1978).

218. O'Neill, H. S. C. Thermodynamics of Co3O4: a possible electron spin unpairing transition in Co3+. *Physics and Chemistry of Minerals* **12**, 149–154 (1985).

219. Brabers, V. A. M. & Broemme, A. D. D. Low-spin-high-spin transition in the Co3O4 spinel. *Journal of Magnetism and Magnetic Materials* **104**, 405–406 (1992).